PROPERTIES OF REINFORCED CARBON NANOTUBE AND LASER-CRYSTALLIZED SILICON FILMS

A Dissertation
Submitted to the Graduate Faculty
of the
North Dakota State University
of Agriculture and Applied Science

By

Matthew Roy Semler

In Partial Fulfillment of the Requirements
for the Degree of
DOCTOR OF PHILOSOPHY

Major Department:
Physics

April 2016

Fargo, North Dakota

North Dakota State University
Graduate School

Title

Properties of Reinforced Carbon Nanotube and Laser-Crystallized Silicon Films

By

Matthew Roy Semler

The Supervisory Committee certifies that this ***disquisition*** complies with North Dakota State University's regulations and meets the accepted standards for the degree of

DOCTOR OF PHILOSOPHY

SUPERVISORY COMMITTEE:

Erik K. Hobbie
Chair

Orven Swenson

Andrew Croll

Long Jiang

Approved:

4/11/16 — Date

Sylvio May — Department Chair

ABSTRACT

Flexible electronics are anticipated to be one of the next technological advancements of electronic devices. The enhanced durability, light-weight nature, and conformity of flexible electronics are desired properties in a variety of fields and are anticipated to reduce production costs. Two promising materials for use in flexible electronics are carbon nanotube (CNT) films and laser-crystallized thin silicon films.

CNTs are in their infancy in respect to their presence in electronic devices; however their superb mechanical and electronic properties make them ideal candidates for flexible electronics. Thin silicon films are a natural transition from bulk silicon as bulk silicon has been the preferred material in electronics since the dawn of the transistor. Thin-film silicon retains the well-studied electronic properties of bulk silicon; however, it becomes flexible as it is thinned.

Obstacles to the application of both these materials in flexible electronics nonetheless exist. Compressed CNT films undergo strain softening – a mechanism in which the CNT film restructures itself in response to an applied strain, which reduces the Young's modulus and electronic conductivity. In this dissertation, thin CNT films are capped with a thin polymer layer, with the aim to mitigate strain softening through excluded volume interactions in a bilayer format that serves as a paradigm for more sophisticated device relevant settings. More specifically, metallic and semiconducting CNT films of different thicknesses are capped with a polystyrene film of comparable thickness, and the mechanical and electronic strain response of the capped CNT film is examined and discussed.

Ultrathin silicon films cannot be grown as monocrystalline silicon, so amorphous silicon films must be deposited and crystallized. Laser crystallization is an alternative to oven annealing and has a faster throughput. In this dissertation, amorphous silicon films of various thicknesses

were deposited on several substrates *via* plasma enhanced chemical vapor deposition. The films were crystallized with a pulsed Nd:YVO_4 laser operating at the third harmonic of 355 nm, and the structural and electronic properties were characterized to determine the effects of film thickness and substrate composition.

ACKNOWLEDGEMENTS

I'd like to start by thanking Erik Hobbie, my advisor, for all of the guidance, motivation, and the opportunity to do the research. Erik, you kept me going when my research seemed to be stuck and often provided the insight to keep it moving forward. Your enthusiasm, reassurance, and support have helped me through the last five years, and I wouldn't be where I am without you. Thank you for everything.

I'd like to thank Orv Swenson for getting me started in research and laying the foundation for my knowledge of optics and lasers. Orv, you gave me to the opportunity to gain three years of invaluable research experience at CNSE during my undergraduate career, which has had echoes throughout my graduate career. As my undergraduate research supervisor, optics professor, and graduate committee member, you taught me the basic laser and optics foundation needed for what I've learned over the past few years. Thanks for all the guidance, Orv.

I'd like to thank everyone in the lab, presently and formerly, who has helped me over the past five years. I'd like to acknowledge Joe Miller, Bekele Gurmesa, John Harris, Damith Rozairo, Sam Brown, Ahmed Elbaradei, Tim Twohig, and the newer members, Mariia Goriacheva, Eid Almutairi, and Abu Niamul. Thank you all for everything. All of the game nights, the racquetball, volleyball and basketball, and intraday discussions kept me sane over the past five years. Joe, you served as a great model to emulate with your excellent work ethic and your positive energy. John thanks for getting me started and providing all the nanotube insight and for the initial time-consuming AFM measurements that you took for me. Damith and Sam, you both have been invaluable, for the research ideas, for letting me bounce ideas off you, and for the intense racquetball matches. Again, thank you all.

I’d also like to thank Justin Hoey and Guru Srinivasan, for all the guidance and assistance with everything related to laser-crystallization, Kevin Mattson, Eric Jarabek, and Greg Strommen for equipment training and cleanroom activities, and Scott Payne for the acquisition of TEM and SEM images.

And finally, I’d like to thank my family and friends for the support over the years.

DEDICATION

To my high school Physics and Chemistry teachers, who inspired me to undertake this journey:

Ron Koester and John Raddick

TABLE OF CONTENTS

ABSTRACT iii

ACKNOWLEDGEMENTS v

DEDICATION vii

LIST OF TABLES xi

LIST OF FIGURES xii

LIST OF APPENDIX TABLES xvi

LIST OF APPENDIX FIGURES xvii

1. INTRODUCTION: FLEXIBLE ELECTRONICS 1

1.1. Carbon Nanotube and Laser-Crystallized Silicon Films 2

1.2. Flexible Electronic Devices 3

1.2.1. Solar Cells 4

1.2.2. Thin Film Transistors 5

1.2.3. Transparent Conductive Films 6

1.3. Objectives and Approach 6

2. EXPERIMENTAL METHODS 7

2.1. Sample Preparation 7

2.1.1. CNT Composite Synthesis 7

2.1.2. Laser-Crystallized Silicon Films 10

2.2. Sample Characterization 13

2.2.1. Optical Microscopy 14

2.2.2. Atomic Force Microscopy 14

2.2.3. Scanning Electron Microscopy 15

2.2.4. X-Ray Diffraction XRD 15

2.2.5. Raman Spectroscopy 16

2.2.6. UV-vis-IR Spectroscopy 17

2.2.7. Ellipsometry 17

2.2.8. Resistivity Characterization........ 18

2.2.9. Tensile Pull Tester........ 19

2.2.10. Strain-induced Elastic Buckling Instability for Mechanical Measurements 20

3. PHYSICS OF CARBON NANOTUBES 22

3.1. Individual Carbon Nanotubes........ 22

3.2. CNT Film Properties 27

4. WRINKLING AND FOLDING OF NANOTUBE-POLYMER BILAYERS 33

4.1. Mechanical Strain-Response 33

4.2. Electronic Strain-Response 38

4.3. Conclusion........ 40

6. PHYSICS OF LASER-CRYSTALLIZATION OF SILICON 41

6.1. Heat Transfer and Phase Change 41

6.2. Crystallization Parameters and Film Properties 46

6.2.1. Crystallization Fluence 46

6.2.2. Crystallization Techniques and Beam Profiles........ 47

6.2.3. Type of Laser and Wavelength........ 49

6.2.4. Crystallization Environment and Sample Preparation 50

7. PROPERTIES OF 355 NM LASER-CRYSTALLIZED SILICON 52

7.1. Morphology Dependence on Film Thickness 52

7.2. Morphology Dependence on Substrate Composition........ 61

7.3. Conclusion........ 71

8. OUTLOOK 73

8.1. Reinforced Carbon Nanotube Films........ 73

8.2. Laser-Crystallization of Silicon 74

REFERENCES 76

APPENDIX A. BEAM SIZE MEASUREMENTS 84

APPENDIX B. LASER-CRYSTALLIZATION SIMULATION DERIVATION AND VERIFICATION........ 85

B.1. Discretization of the Heat Equation........ 85

B.2. Code Verification 88

B.3. Thermal Properties of Materials 92

APPENDIX C. LASER-CRYSTALLIZATION CODE 95

LIST OF TABLES

Table Page

1. Mechanical properties of CNTs, copper, and polystyrene. 24

2. Lasers commonly used for the laser-crystallization of silicon films. 42

LIST OF FIGURES

Figure Page

1. Schematic of a solar cell. The n-type material is either n-doped CNTs or n-type laser crystallized silicon. Laser-crystallized silicon solar cells are typically completely polycrystalline silicon, whereas CNT devices have thus far been designed on monocrystalline silicon wafers. 5

2. Schematic of a field effect transistor. When a potential is applied to the gate electrode, current flows from the source to the drain. 5

3. CNT solutions and films. a) The parent solution (black), metallic type-sorted (blue), and semiconducting type-sorted (brown) solutions are shown. b) Metallic (blue) and semiconducting (brown) films filtered on cellulose-based filter paper are shown.[28] 8

4. Strain stage and schematic of bilayer sample. a) PDMS mounted on a strain stage. b) Schematic of bilayer sample shows the three regions of interest – the CNT, PS, and bilayer film. 9

5. Schematic of laser-crystallization setup........ 13

6. AFM thickness measurement of a CNT film. a) The 3D profile of the edge of a CNT film on quartz. b) The height profile along the line marked in a)........ 15

7. Energy diagram of Stokes (left) and anti-Stokes (right) scattering used by Raman spectroscopy........ 16

8. Electrode pattern on a SWCNT film........ 19

9. Chirality map of SWCNTs. The blue dots represent metallic SWCNTs and the green, semiconducting SWCNTs........ 23

10. Raman spectra of a metallic SWCNT film. The inset shows the RBM with finer resolution. The RBM is a convolution of at least two peaks, which means the metallic SWCNT film contains with a variety chiralities........ 25

11. TEM, SEM, and SALS plot of SWCNT films. The film structure is shown in the a) TEM and b) SEM images of a film. Scale bars are 200 nm for the TEM image and 250 nm for the SEM image. SALS of a metallic and semiconducting SWCNT films both have exponents of 1.72, suggesting they have the same structure.[5] 28

12. SWCNT and a PS films under 5 % compressive strain on PDMS. a) A reflection micrograph shows the wrinkle pattern of the 30 nm SWCNT film. The scale bar represents 10 μm. b) Profiles of metallic (blue) and semiconducting (brown) films obtained from the intensity of the reflection micrograph. c) A reflection micrograph of a PS film compressed at 5 % strain shows the creases with the more subtle wrinkles between them. 30

13. Reduced Young's modulus of metallic and semiconducting SWCNT films.[4] 30

14. a) Sheet conductivity shows the longer semiconducting SWCNTs (green) have a lower connectivity percolation threshold than metallic CNTs (blue). b) The semiconducting SWCNTs have a narrower diameter resulting in a film with a lower rigidity percolation threshold due to the ability of the SWCNTs to form denser films, as shown in c). 31

15. Length and diameter distributions of metallic (blue) and semiconducting (yellow) SWCNTs. The metallic SWCNTs are shorter and have a larger diameter. 32

16. The strain response of the sheet resistance for semiconducting compared to metallic SWCNTs. Although the metallic SWCNTs appear to be much more resilient than the semiconducting SWCNTs, much of the difference in this figure is attributable to residual excess surfcactant.[28] 32

17. A schematic denoting the effect the polymer filler has on a compressed SWCNT film. 33

18. Reflection optical micrographs of compressed films.[70] (a) A 125 μm thick PS film on PDMS at 2.5 % strain (width = 110 μm). (b) A 35 nm thick metallic SWCNT film at 10 % strain (width = 25 μm). (c) A 32 nm thick semiconducting SWCNT film covered with a 125 nm thick PS film at 10 % strain. The dashed line indicates the interface of the capped SWCNT film and the pure PS film (width = 90 μm). (d) A 50 nm PS film (top) and a capped SWCNT film (bottom, $h_{PS} = 33$ nm, $h_{PS} =$ 16 nm) at 5 % strain. The two images show a comparison of wavelengths (the scale bars represent twice the fundamental wavelength) of the composite and a PS film of comparable thickness. 34

19. TEM cross-sectional images of the SWCNT-PS interface.[71] The bottom image shows the SWCNTs being removed with the PS as it is peeled off the 60 nm metallic SWCNT film. 35

20. (a) Metallic and (b) semiconducting SWCNT film moduli vs. strain with fits using Equation 6.1. Open markers represent uncapped SWCNT data and solid markers represent capped SWCNT data. The lower legend thicknesses are the SWCNT film thicknesses, and the upper legend is for the PS film thicknesses.[71] 36

21. Zero-strain modulus of (a) metallic and (b) semiconducting SWCNT films. The light data represent the uncapped films and the dark data represent the capped data.[71] 37

22. Yield strain of (a) metallic and (b) semiconducting SWCNT films. The data was extracted from the fits in Figure 20 and plotted against thickness. The dark lines represent the capped data and the light represent the uncapped data.[71] 38

23. Normalized sheet resistance for compression/stretching of uncapped and capped films.[71] (a) and (b) are 20 nm and 40 nm thick metallic films, and (d) and (e) are 20 nm and 65 nm thick semiconducting films. The unstrained sheet resistance after each cyclical compression and extension was plotted as a function of the cycle number for the (c) metallic films, and (f) the semiconducting films. The improved stability of the strain response, in comparison to that depicted in Figure 16, can be attributed to cleaner SWCNT films with less residual surfactant. 39

24. The measured absorption coefficient of amorphous silicon increases dramatically for wavelengths shorter than 600 nm. 41

25. Optical micrographs of various intrinsic film thicknesses laser-crystallized with different fluences.[107] The scale bar is 5 μm. 53

26. High-resolution SEM images of laser-crystallized doped (n-type) films.[107] Film thicknesses are 41 nm (top) and 125 nm (bottom), and the samples were crystallized with fluences of 38, 44, and 55 mJ/cm^2 (left to right). The scale bar is 2 μm, and the rectangular insets are 1.6 μm wide. 54

27. (a) Raman spectra of 121nm thick laser-crystallized intrinsic silicon films. The FWHM (b) and Raman shift (c) of the crystalline TO peak for several film thicknesses crystallized at varied laser pulse energies as indicated in the legend.[107] 55

28. (a) XRD spectra of 121 nm thick intrinsic Si films in descending order of laser fluence; 26.6, 18.4, and 10.1 mJ/cm^2. The bottom reference spectrum is for a-Si. (b) The FWHM of the (111) peak for a 121 nm thick silicon film vs. laser fluence. (c) Mean crystallite diameter as a function of laser fluence.[107] 56

29. (a) Resistivity of the phosphorous-doped, laser-crystallized films. (b) Average visible transmittance and reflectance of 121 nm thick intrinsic, laser-processed films. (c) Tauc plot for the 121 nm thick intrinsic film at low laser fluence, where the inset shows the optical band gap determined from such plots along with the accepted value (dashed line) for a-Si (1.7 eV).[107,111,112] 58

30. Phase diagrams for (a) the film morphology and (b) the Raman shift of the intrinsic laser processed films.[107] 59

31. (a) Dimensionless scaling plot of the data in Figure 29. (b) Thickness dependence of the scaling parameter for the resistivity with a linear fit (upper, expressed as conductivity), which mirrors the change in Raman shift associated with the loss of crystallinity at fixed fluence (lower). (c) Thickness dependence of the critical fluence where the resistivity diverges, which mirrors the onset of agglomeration in the phase diagram in Figure 30(a).[114] 60

32. i-Si (top) and n-Si (bottom) films crystallized at 55 mJ/cm^2 on (left to right) quartz, BAS, YSZ, and c-Si substrates. The scale bar in the lower right image is 5 μm.[114] 62

33. (a) The percentage of substrate covered by the film as a function of laser fluence. (b) Transmission images of i-Si on quartz, BAS, and YSZ (top to bottom) at 21 (left) and 27 mJ/cm^2 (right). White regions are areas of exposed substrate, and the dark circles are pillars that absorb more of the light. The scale bar in the lower right image is 5 µm.[114] 63

34. SEM images of n-Si films crystallized at a laser fluence of 55 mJ/cm^2 on quartz, BAS, YSZ, and c-Si substartes (left to right), as viewed normal (top) and tilted at 45° (bottom) to the sample. The scale bar and insets are 1.5 µm wide.[114] 64

35. Normalized probability distributions of width (top), length (middle), and angle (bottom) for a-Si films crystallized at a laser fluence of 55 mJ/cm^2.[114] 64

36. Feature height (left) and spatial density of features (right) plotted versus laser fluence for the n-Si and i-Si films on each of the four substrates.[114] 65

37. Raman spectra for i-Si (*solid*) and n-Si (*dashed*) crystallized on quartz with four different fluences. The amorphous contribution is evident at 15 mJ/cm^2, whereas the Fano effect is evident at 55 mJ/cm^2.[114] 66

38. a) The Raman shift, b) FWHM, c) crystallinity and q-parameter (inset) for n-Si films plotted as a function of laser fluence. Open symbols with dashed lines denote n-Si and solid symbols with solid lines denote i-Si. Green denotes YSZ, red denotes quartz, and blue denotes BAS.[114] 67

39. Resistivity (left) and crystallite diameter (right) of the i-Si and n-Si films plotted against laser fluence for the four different substrates.[114] 68

40. Left - simulated crystallinity (solid squares) and experimental crystallinity from Raman (open squares) versus laser fluence. Right - simulated surface melt duration versus laser fluence.[114] 69

LIST OF APPENDIX TABLES

Table Page

B1. Simulation parameters used to verify heat equation. 89

B2. Simulation parameters used to verify laser-heating source term. 90

B3. Simulation parameters used to verify phase transition mechanism. 92

B4. Fits of thermal conductivities used during silicon crystallization simulations. 93

B5. Fits of heat capacities used during silicon crystallization simulations................................ 93

B6. Material properties used for silicon crystallization simulation. 94

B7. Laser parameters used for silicon crystallization simulation. 94

LIST OF APPENDIX FIGURES

Figure Page

A1. Gaussian fits to the major (left) and minor (right) axes. 84

B1. Temperature profiles of a wire with the ends fixed at 300 and 2000 K. The thick dark lines are the data collected from the simulation and the pastel lines are the theoretical values calculated from Equation B9. 89

B2. Plots of the source term as a function of (a) depth, and (b, c) time. 91

B3. Temperature of a wire uniformly heated past the melting temperature. 92

1. INTRODUCTION: FLEXIBLE ELECTRONICS

Flexible electronics are anticipated to open up new possibilities for electronic devices, including biomedical, commercial, consumer, and military applications.[1] The advantages of flexible electronics exist in the lightweight, bendable, and durable nature of the devices, and the anticipated reduced production costs. Applications that are generating a great deal of interest are in flexible sensors, displays, and photovoltaics, among others.[1]

In the biomedical field, flexible sensors could drastically improve patient care and standard of living.[2] Vitals could be monitored constantly with more comfort for the patient by the incorporation of sensors into clothing or bandages, and the conformal nature of flexible electronics would ensure comfortable, reliable connectivity with the patient. It may even be possible to produce biocompatible bandages that sense the presence of infection and release antibiotics.

The addition of electronics to packaging materials is anticipated to improve productivity and ensure food quality. Radio frequency identification is a common technology used to track crates at warehouses, and by placing RFID directly into individual packaging, stores could determine if shelves need to be stocked, if items are located in the proper place, or as an anti-counterfeit measure.[1,3] Sensors in packaging could also ensure quality of the item, such as the freshness of food products.[3]

Many consumer and military applications overlap, including wearable electronics and sensors, flexible displays and other ruggedized electronic devices. Like the biomedical applications, wearable sensors can be used to measure soldier or civilian biometrics, such as heart rate and temperature. The sensors could also be used to determine environmental states as well, such as the presence of biological weapons in warzones.[1]

Flexible displays have been an area of interest for some time. The resilience of displays will enhance the durability of goods - brittle smart phone screens are prone to cracking when dropped, whereas flexible displays would be capable of withstanding the sudden stress. Cost reductions are anticipated to arise from a reduced amount of material needed to construct the devices, as well as cheaper manufacturing processes, such as roll-to-roll and liquid-based processing.

1.1. Carbon Nanotube and Laser-Crystallized Silicon Films

Carbon nanotubes (CNTs) and thin silicon films are two promising materials for use in flexible electronics. CNTs are incredibly strong nanostructures with high aspect ratios. They are carbon-based, tubular structures that are roughly a nanometer in diameter and as long as a centimeter. The structure of CNTs is the source of their strength. The carbon-carbon bonds are among the strongest in nature, and the tube-like structure builds on this strength, requiring several bonds to break before the CNT is severed. The quantum nature of CNTs gives rise to their conductive properties, rivaling that of copper, while having a density comparable to that of plastics. The mechanical and electronic properties of CNTs make them ideal candidates for flexible electronics.

Interfacial interactions between CNTs are weaker than the carbon bond strength, resulting in a film weaker than the individual components. CNT films, however, are still quite strong, with a Young's modulus on the order of gigapascals.[4] When CNT films are compressed, they undergo a phenomenon called strain softening,[5] which results in a bundling and realignment of CNTs in the direction perpendicular to the applied strain. Strain softening reduces the strength of the CNT film, a detriment to its candidacy as a material used in flexible electronics. By capping the CNT

film with a polymer film, the mechanical properties could be enhanced, as discussed in a later chapter.

The replacement of bulk silicon with thin silicon films is a natural transition from traditional electronics to flexible electronics due to the ubiquity of bulk silicon in electronics. Rigid materials, including silicon, exhibit a degree flexibility when thinned,[6] however, mechanical thinning of silicon is limited to a thickness on the order of tens of microns[7] and typically introduces cracks and dislocations in the crystal. To create silicon films at the nanoscopic scale with greater flexibility, amorphous silicon can be deposited *via* chemical vapor deposition, or other means,[8] and crystallized.

Laser crystallization is a popular technique that employs a pulsed or continuous-wave laser to melt a region of silicon. Laser crystallization is a relatively mature technology dating back to the 1970's.[9] When the molten silicon cools, it freezes as crystalline silicon. The processing speed of laser-crystallization far exceeds that of oven annealing, and the short pulse duration and high absorption of the silicon results in localized heating of the silicon film,[10] making materials with low melting temperatures, such as plastics, viable substrates.[11] In this dissertation amorphous silicon films are deposited *via* plasma enhanced chemical vapor deposition and crystallized with a $Nd:YVO_4$ pulsed laser operating at the third harmonic wavelength of 355 nm. The effects of the film thickness and the substrate composition on the morphology were characterized and are presented in a later chapter.

1.2. Flexible Electronic Devices

CNTs and laser-crystallized silicon have several applications in flexible electronics. The architecture and physics of solar cells and thin film transistors are described in this section, as well as the potential application of CNTs films as transparent conductive films.

1.2.1. Solar Cells

Solar cells are diodes that employ the photoelectric effect to produce electricity. The basic structure of a solar cell consists of two doped, one n-type and the other p-type, semiconductors that are in contact with one another. Semiconductors doped with Group 5 elements result in an n-type semiconductor with an excess of electrons, whereas doping with Group 3 elements result in p-type semiconductors, which have a shortage of electrons (or an excess of holes) in the valence shell. When the semi-conductors are in contact, the electrons in the n-type semiconductor diffuse into the p-type semiconductor to fill the holes. The n- and p-type regions are now positively and negatively charged, forming an electric field and preventing further diffusion of the carriers. The region occupied by the electric field is called the depletion zone. When a photon with energy greater than the band gap of the absorbing layer is absorbed, it can create an electron-hole pair. If the electron-hole pair interacts with the electric field in the depletion zone before annihilating, they can create a potential difference.

Both CNT films[12-15] and laser-crystallized silicon[16-18] have been used in solar cells. Schematics of typical device architectures are shown in Figure 1. CNT solar cells have been capable of achieving an efficiency of 15 %, although the physics of the devices is not fully agreed upon.[15] Laser-crystallized silicon films have had lower efficiencies, near 10 %. The two values should not be compared directly as the CNT solar cells were designed on monocrystalline n-type wafer silicon, whereas the laser-crystallized devices were composed completely of laser-crystallized silicon.

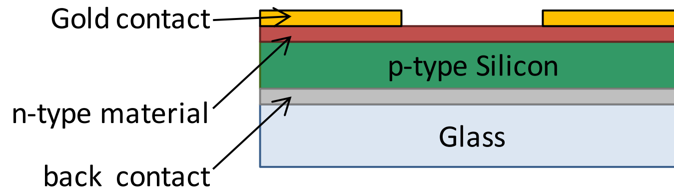

Figure 1. Schematic of a solar cell. The n-type material is either n-doped CNTs or n-type laser crystallized silicon. Laser-crystallized silicon solar cells are typically completely polycrystalline silicon, whereas CNT devices have thus far been designed on monocrystalline silicon wafers.

1.2.2. Thin Film Transistors

Transistors are semiconducting devices that act as amplifiers or switches. The structure of a field effect transistor (FET), shown in Figure 2, is composed of two n-type semiconductors separated by a p-type semiconductor, which forms two different depletion zones. Two pairs of electrodes are deposited on the FET - a source and drain pair are deposited on the n-type semiconductor, and a pair of electrodes is deposited on the bottom (the body) of the FET and on top of an oxide layer on the top of the FET (the gate). When a potential is applied to the gate, the depletion zones are flooded with electrons, allowing current to flow from the source to the drain.

The electron field effect mobility is a common property used to characterize transistors. High electron mobilities result in transistors with quicker response and higher operational frequency. Standard silicon transistors typically have field effect mobilities near 1000 $cm^2 V^{-1} s^{-1}$. CNT and laser crystallized silicon thin film transistors have mobilities much lower than the crystalline silicon standard, and are near 150 and 410 $cm^2 V^{-1} s^{-1}$, respectively.[19,20]

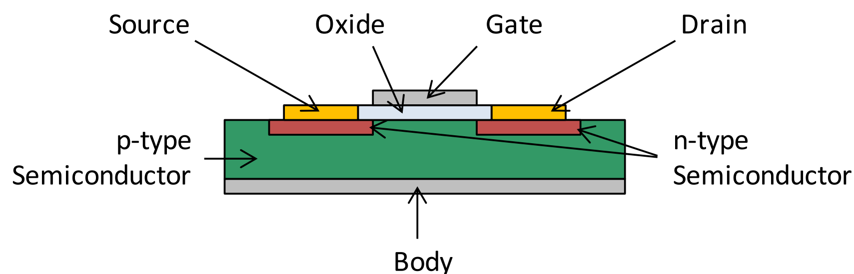

Figure 2. Schematic of a field effect transistor. When a potential is applied to the gate electrode, current flows from the source to the drain.

1.2.3. Transparent Conductive Films

Indium tin oxide (ITO) is the most common transparent conductive material and is used in LEDs, solar cells, and displays, such as cell phones. The excellent optical and electronic properties of ITO make it an ideal transparent conductor, and the deposition is a well-established and controllable process. However, ITO is a brittle ceramic material not suitable for flexible electronics. The conductive nature of CNT films, and the semi-transparency of the films at visible and IR wavelengths, make it a potential suitable replacement.[21-23] Doping CNT films can significantly enhance the conductivity of the films, while retaining their optically transmissive properties.[24]

1.3. Objectives and Approach

This dissertation focuses on the properties of CNTs and laser-crystallized silicon, two promising materials for flexible electronics. In Chapter 2, the techniques used to prepare, treat, and characterize the samples will be covered. Chapter 3 gives a detailed background on the properties of individual CNTs and CNT films. In an attempt to mitigate the strain softening of CNT films, they are capped with a polymer layer. The properties of the capped films are discussed in Chapter 4. Chapter 5 gives a background on the laser-crystallization of silicon, starting with the theory and followed by the experimental observations. Chapter 6 covers the dependence of the morphology on film thickness and the substrate composition of silicon films crystallized with a 355 nm laser. Finally, Chapter 7 provides a brief summary and the outlook for the two materials.

2. EXPERIMENTAL METHODS

In this chapter, the equipment and techniques used to create samples and characterize them will be discussed. An emphasis will be placed on the procedures used to produce and treat samples.

2.1. Sample Preparation

2.1.1. CNT Composite Synthesis

Thermoplastic or thermosetting polymer is typically the primary component of polymer-CNT composites, however, the research presented in this dissertation reverses this notion and uses a CNT film as the base material and polymer as the filler material. The composite is constructed by annealing a thin polystyrene film above its glass transition temperature on a CNT membrane under vacuum. Under these conditions, the polystyrene infiltrates the semi-porous CNT membrane, creating the composite bilayer film. The bilayer architecture here is critical because it preserves the distinct "heterojunction geometry" that underlies all of the applications our group is focused on.

Electronic type-sorted aqueous solutions of single-wall carbon nanotubes (SWCNTs) were obtained from NIST.[25,26] SWCNTs purified from the soot produced by the laser ablation method were dispersed in water using surfactants, and this solution then underwent electronic-type separation. The purification and separation process is described as follows: SWCNT powder (NASA-JSC laser ablation batch 338), loaded at (1.0 ± 0.1) mg/mL, was tip-sonicated in an aqueous solution of surfactant (2 % wt. sodium deoxycholate, DOC) for one hour in 32 mL batches in ice water at 30 W of power. Each solution was centrifuged for 2 hours at 1885 rad/s in a Beckman-Coulter JA-20 rotor and the supernatant was collected. The films were sorted by electronic type as described by Arnold *et al.*[27] Prior to type-separation, water was added to the

SWCNT solution. Type-separation was done in a Beckman-Coulter VIT 65.2 vertical rotor for 1 hour at 6800 rad/s at 20 °C with the following layers: 1 mL of 18 % mass per volume oidixanol and 1 % DOC; 3 mL of 9 % mass per volume iodixanol and 1 % DOC; 0.9 mL of 2 % DOC/SWCNTs. A middle band containing the water-filled SWCNTs was collected from multiple runs and concentrated using forced filtration to produce the parent, mixed-type solution used for type sorting as described by Harris *et al*.[28]

The parent solution was type-sorted as follows. The solution layers used for type separation were: 1 mL of 40 % mass per volume iodixanol, 0.75 % sodium (dodecylsulfate) (SDS), and 0.75 % sodium cholate (NaChol); 2 mL of purified CNTs in 32 % iodixanol, 1.125 % SDS, and 0.5 % DOC; 20 mL of 30 % mass per volume iodixanol, 1.125 % SDS, and 1.125 % NaChol. The solution was allowed to equilibrate for four days and then centrifuged using a Beckman-Coulter SW-32 rotor for 19.25 hours with a spin speed of 3350 rad/s at 20 °C. The type sorted solutions were extracted and dialyzed through forced filtration against a 30 kD membrane to exchange the SWCNTs into 1 % DOC, increasing the concentration.

The solutions were diluted in de-ionized (DI) water to make a 150 mL solution and were pulled through porous cellulose-ester filter paper using a vacuum filtration system. A 10 % ethanol in water mixture was repeatedly pulled through the SWCNTs to remove the surfactant. Metallic and semiconducting films on the filter paper are shown in Figure 3.

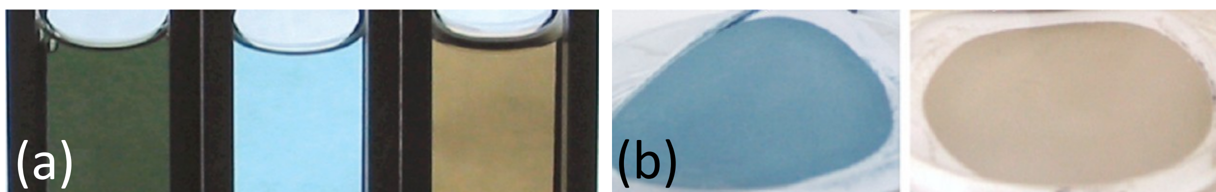

Figure 3. CNT solutions and films. a) The parent solution (black), metallic type-sorted (blue), and semiconducting type-sorted (brown) solutions are shown. b) Metallic (blue) and semiconducting (brown) films filtered on cellulose-based filter paper are shown.[28]

Polydimethyl siloxane (PDMS, Sylgard 184, Sigma-Aldrich) substrates were used for strain experiments and were prepared by mixing a 10:1 ratio of PDMS monomer to cross-linker. The volume was chosen such that the substrates had a final thickness of 2 mm. The mixture was poured and spread onto a 10 cm x 20 cm glass plate. The PDMS was degassed under 85 kPa vacuum for one hour, then heated to 90 °C under a vacuum pressure of 50 kPa for 2 hours. The samples were removed from the oven and cut into 1" x 3" slabs.

For initial experiments, a 15 % pre-strain was applied to a PDMS substrate using a strain stage (Figure 4). PDMS was clamped to the carriage, which was then mounted to a linear stage. The linear stage translated one of the PDMS clamps while the other remained stationary. A small area, approximately 4 mm x 4 mm, of a CNT film was deposited on the PDMS substrates by placing the CNTs on the substrate with the filter paper exposed. The CNTs were repeatedly covered and rinsed in acetone for two hours to dissolve the filter paper, followed by repeated rinsing for two hours with ethanol to remove residual surfactant. The sample was placed in the vacuum at 85 kPa to remove any residual volatiles.

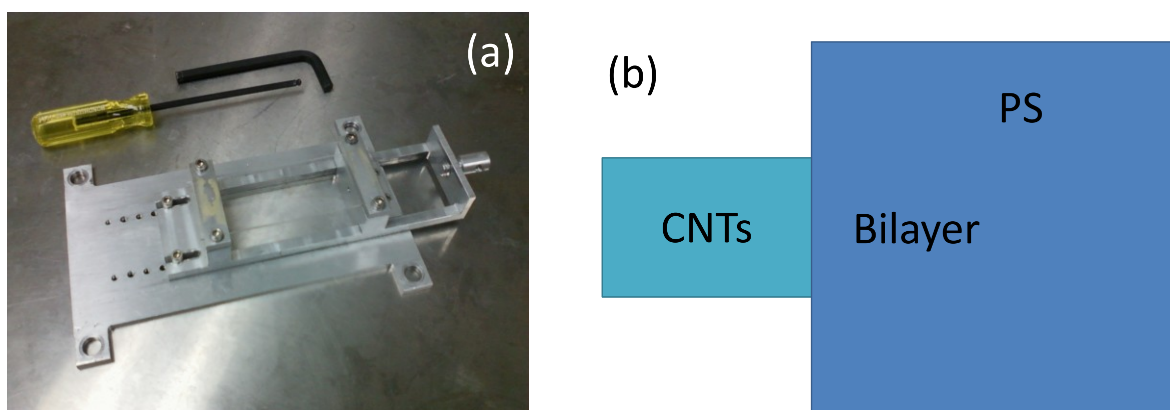

Figure 4. Strain stage and schematic of bilayer sample. a) PDMS mounted on a strain stage. b) Schematic of bilayer sample shows the three regions of interest – the CNT, PS, and bilayer film.

Polystyrene (PS, M_w=192 kg/mol, Sigma-Aldrich) films were spin-cast using a 0.72 % wt. PS in toluene solution at 2000 rpm on a cleaved mica substrate. The film was cut into areas

of 5 x 5 mm^2 and floated on DI water. The PS films were placed on the CNTs such that the CNT film was partially covered, as shown in Figure 4b. The strain stage was put in the vacuum oven, and the capped CNT film was annealed at 115 °C, above the glass transition temperature of PS, under 50 kPa vacuum pressure for 30 minutes. The pre-strain was released in steps and microscope images were taken at applied uniaxial strains of 2.5, 5.0, 7.5 and 10.0 %.

To apply isotropic strains below 2 % a different technique was used in which the thermal expansion of the PDMS substrate was exploited. Low-strain samples were prepared in the same manner as described above, except no pre-strain was applied to the PDMS. After the sample was removed from the oven, it was immediately placed on a hot stage and heated to 115 °C for one hour to ensure the PDMS had fully expanded. The sample was allowed to cool under a microscope and images were taken every minute until the sample had cooled to room temperature.

2.1.2. Laser-Crystallized Silicon Films

Plasma enhanced chemical vapor deposition (PECVD) is a common technique used to deposit amorphous silicon directly on a substrate, however, the properties of crystalline silicon are preferential to amorphous silicon, and so amorphous silicon films are typically crystallized *via* a number of techniques, including laser-crystallization. In this section, the deposition and laser-crystallization methods used to create crystalline films are described.

2.1.2.1. Amorphous Silicon Deposition

Chemical vapor deposition (CVD) is a common technique used to deposit solid films on different substrates. Several different materials can be deposited, including metals, oxides, silicon compounds, etc. Films are deposited by exposing the substrate to a flow of energetically unstable gas that decomposes onto the substrate, forming a solid film. Basic CVD relies on a

heated substrate (typically 600 °C to 800 °C) to decompose the gas, whereas plasma-enhanced chemical vapor deposition (PECVD) radicalizes the gas by converting it to a plasma before exposing it to the substrate, allowing the substrate to be heated to lower temperatures (typically 250 to 350 °C). Several deposition parameters affect the film properties, including pressure and temperature. For a-Si, disilane gas is typically used, which results in a thin film with a hydrogen content of roughly 10%. Temperature primarily determines the deposition rate of the film, whereas the pressure largely affects the hydrogen content.[29]

Laser-crystallization samples were prepared by depositing a-Si *via* PECVD on quartz, boroalumino-silicate (BAS), yttria-stabilized zirconia (YSZ), and crystalline silicon (c-Si). Quartz was chosen based on previous research, whereas the remaining samples were chosen due to availability. The substrates were prepared with an RCA clean (Standard Clean 1 and Standard Clean 2: $H_2SO_4 + H_2O_2$, buffered HF, $HCl + H_2O_2$). A diffusion layer consisting of a 250 nm thick layer of SiO_2 was grown on the quartz substrate *via* PECVD, using an Oxford PlasmaLab 100, immediately after the RCA cleaning process. Intrinsic (i-Si) and degenerately doped n-type (n-Si) a-Si films were then deposited using PECVD. The films were grown using a mixture of 5 % disilane (Si_2H_6) gas in helium and hydrogen at flow rates of 30 sccm and 5 sccm, respectively. Doped samples were grown using 5 % Si_2H_6 in helium at a flow rate of 25 sccm with 5 sccm hydrogen, 25 sccm argon, and 1 sccm PH_3. Both types of films were grown at a chamber pressure and temperature of 1000 mTorr and 300° C, respectively.

2.1.2.2. Laser Crystallization Setup and Process

A pulsed neodymium-doped yttrium othrovanadate laser ($Nd:YVO_4$, Spectra-Physics HIPPO) operating at the tripled-frequency wavelength of 355 nm was used to crystallize the a-Si films under ambient conditions. The laser power was attenuated with a motorized, rotating half-

waveplate and a dichroic polarizer, which reflects S-polarized light. The S-polarized light was reflected to a power-meter. The transmitted beam diameter was increased from 3 mm to 8 mm using a beam expander. A pair of cylindrical positive and negative lenses (± 100 mm focal length), spaced 2.0 cm apart transformed the circular beam into an elliptical beam with a high aspect ratio.[30] The Gaussian beam was translated along the sample using a HurryScan 12 scanhead. An Aerotech XYZ stage system was used for long-range travel of the sample and focusing of the beam on the substrate. A schematic can be seen in Figure 5. Using an Ophir Optronics BeamGage beam profiler, the major and minor axes of the beam were measured several times at different places on the sensor, as described in Appendix A. The profiler had a resolution of 4.4 μm per pixel. Two Gaussian curves were fitted to the profiler data along the major and minor axes of the beam for each profile. The average beam length and width were 1526 μm and 11 μm, respectively, at $1/e^2$ intensity. The area of the beam was then calculated to be 5.27E-4 cm^2. Prior to experiments, the power was measured with a removable power-meter below the scanner. The sample was illuminated with red light emanating from a ring light mounted below the scanner. A CCD camera attached to the scanner was used view the sample for accurate positioning of the beam prior to the crystallization process.

The a-Si films were crystallized based on the sequential lateral solidification technique, which has been shown to produce long crystals.[31] The beam was scanned in the direction of the minor axis to the edge of the sample, at which point the laser was turned off and the beam began a new scan translated 50 μm along the major axis from the original location. The process was then repeated until the sample was fully scanned. The 50 μm beam offset between consecutive scans was determined in preliminary experiments through use of Raman spectroscopy.

The laser translation velocity was 25 mm/s with a repetition rate of 50 kHz, which corresponds to a distance of 0.5 μm between pulses.[32] As mentioned earlier, a-Si films deposited *via* PECVD contain large amounts of hydrogen. If the sample is heated rapidly, the hydrogen is explosively released, which destroys the film. Laser crystallization processes that incorporate uniform beam intensity require the hydrogen in the film to be removed prior to the crystallization process. This is often done by heating the sample, or by scanning the sample at a low fluence.[33] Since a Gaussian beam was employed to crystallize the samples, it was unnecessary to reduce the hydrogen content in the films because the lower intensity regions of the beam cause hydrogen to diffuse without ablating the film.

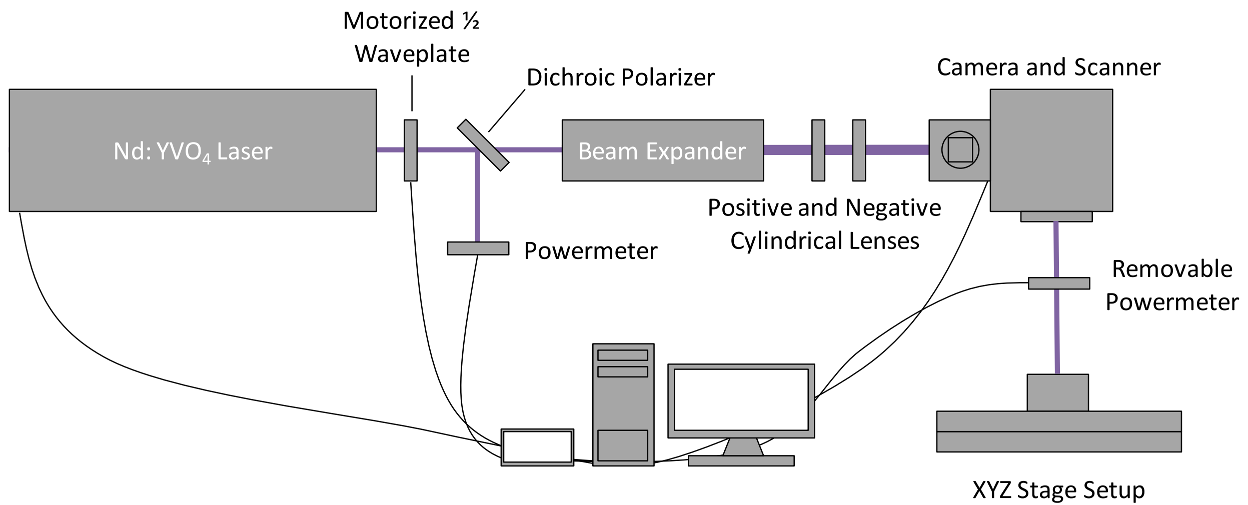

Figure 5. Schematic of laser-crystallization setup.

2.2. Sample Characterization

Many characterization techniques were applied to determine the mechanical, structural, electronic, and optical properties of each sample. An overview of how each technique was applied will be discussed in the following subsections.

2.2.1. Optical Microscopy

To characterize the wrinkling wavelength of the compressed SWCNT-PS bilayer, reflection optical micrographs were taken using an Olympus BX51 microscope with a 50x objective in bright field mode at the different compressive strains. The same microscope was used to obtain transmission images of laser-crystallized silicon films using the 50x objective to determine film agglomeration during the crystallization process. An Olympus BX60MF5 microscope with a 100x objective was used to obtain reflection micrographs of the laser-crystallized silicon films to observe the morphology of the film.

2.2.2. Atomic Force Microscopy

Atomic force microscopy (AFM) was used to obtain the thickness of SWCNT/PS films and the morphology of laser-crystallized silicon films. A Veeco DI-3100 atomic force microscope was operated in tapping mode. An NT-MDT FMG01 probe with a tip radius of 10 nm was used to obtain profiles. To characterize film thickness, three different step heights were measured at different spots on the film, and for each region, eight profiles were tilt corrected and the average step height was calculated. A profile of a CNT film is shown in Figure 6. Film thicknesses of the CNT film and the PS film were measured directly, and the step height of the PS onto the bilayer was measured to calculate the total thickness of the composite, which is the sum of the PS thickness and the step height of the polymer onto the bilayer. By using this method to measure the bilayer total thickness, we take into account the thickness lost due to the PS seeping into the CNT network.

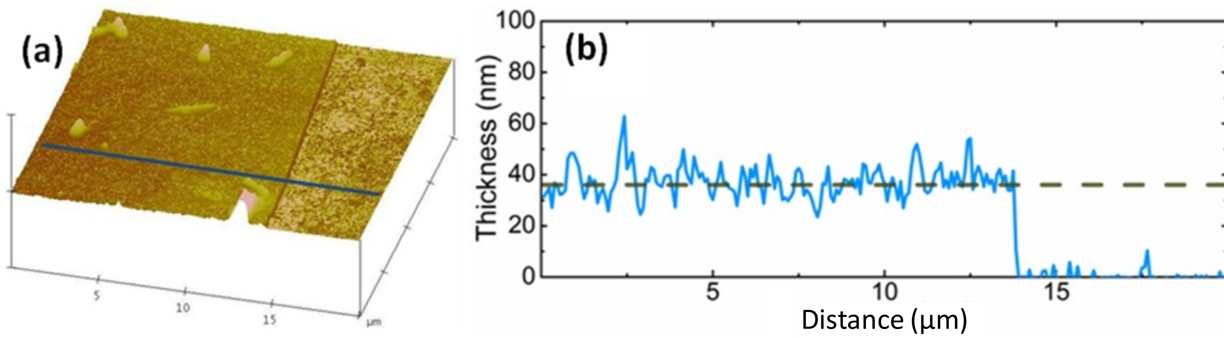

Figure 6. AFM thickness measurement of a CNT film. a) The 3D profile of the edge of a CNT film on quartz. b) The height profile along the line marked in a).

Morphology of laser-crystallized silicon films was analyzed using Gwyddion, an open-source software. The data was leveled by mean plane subtraction and the minimum value was set to zero. The watershed algorithm employed by the software was used to determine peak locations and their corresponding heights.

2.2.3. Scanning Electron Microscopy

Scanning electron microscope (SEM) images were taken of laser-crystallized silicon films to obtain greater detail of the morphology. A JEOL JSM-7600F high-resolution SEM was operated at 2.0 keV to image the samples. To reduce charging, samples were coated with carbon in a Ted Pella Cressington 208C high-vacuum carbon evaporative coater.

2.2.4. X-Ray Diffraction

X-Ray diffraction (XRD) was employed to determine the mean crystallite size of the laser-crystallized silicon films. Since the diffraction spectra of thin films were being acquired, grazing incidence XRD was employed, using a Bruker D8 Discoverer with a GADDS multipurpose X-ray diffractometer at an incident angle of 1° with an instrumental broadening of 0.107°. The background was subtracted from the spectra and a Gaussian curve was fit to the most intense peak, the $\langle 111 \rangle$ peak at $2\theta = 28.4^{\circ}$.

2.2.5. Raman Spectroscopy

Raman spectroscopy was used to characterize the laser-crystallized silicon films. Raman spectroscopy is a versatile measurement technique that gives information on the vibrational modes of materials. A laser excites the atoms of a material to a virtual state, from which they instantly return to a vibrational state, releasing a scattered photon. The scattered photon may be released *via* Stokes scattering, in which it has less energy than the initial photon, or *via* anti-Stokes scattering, resulting in a scattered photon with more energy. The difference in energy of the incoming and the emitted photon give rise to the Raman shift (ω), given by:

$$\omega = \frac{1}{\lambda_o} - \frac{1}{\lambda_1} \tag{2.1}$$

where λ_o and λ_1 are the wavelength of the incoming and scattered phontons. Different solids have different phonon modes, which appear as different Raman shifts, making identification of the material possible. Here, this is exploited to determine the crystallinity of laser-crystallized samples.

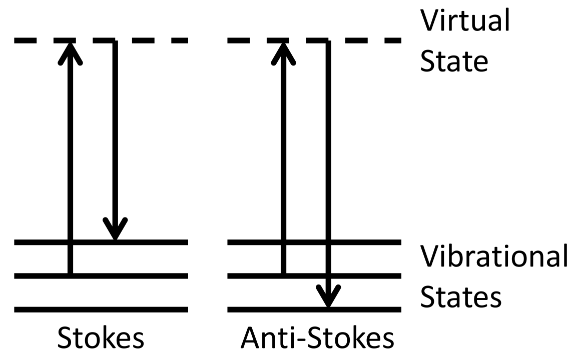

Figure 7. Energy diagram of Stokes (left) and anti-Stokes (right) scattering used by Raman spectroscopy.

Raman spectra were collected with a Horiba Jobin-Yvon Aramis confocal Raman imaging system. A 532 nm CW laser passed through a 10x objective to create a 20 μm diameter beam on the sample. The scattered light was collected with an InGaAs detector. A 600 lines/mm

grating was used with a slit and hole of 150 and 600 μm, respectively. With these parameters, the spectral resolution was 1.5 cm^{-1}.

Because a-Si absorbs at 532 nm, high powers had the potential to crystallize the film. To obtain accurate spectra with the largest intensity possible, spectra of a-Si were taken with the highest neutral density filter available, followed by the next highest, and so on until a crystalline peak was observed. The lowest neutral density filter that produced a spectrum without the crystalline peak present was used.

2.2.6. UV-vis-IR Spectroscopy

Transmittance and reflectance measurements of laser-crystallized silicon films were obtained to characterize their optical properties. A Varian Cary 5000 spectrometer was used to obtain the transmittance and reflectance spectra of laser-crystallized films from 250 to 2500 nm. The absorption coefficient was calculated from the spectra using the Beer-Lambert relationship:

$$\alpha = -\frac{1}{x}\ln(T^*), \tag{2.2}$$

where x is the thickness and T^* is the internal transmittance spectra of the sample. The internal transmittance was determined from the transmittance (T) and reflectance (R) spectra using the relation:

$$T^* = \frac{T}{1-R}. \tag{2.3}$$

The internal transmittance was adjusted such that the spectrum is non-negative and does not exceed unity.

2.2.7. Ellipsometry

Ellipsometry was used to determine the thickness of the deposited amorphous silicon films. Ellipsometry measures the change in reflected polarization of several wavelengths of light

after it interacts with a film and is primarily used to determine the complex refractive index and thickness of the film. Film thickness can only be determined if the refractive indices of the ambient, film, and substrate are known, and the film is transmissive enough such that the light transmits through twice the thickness of the film to interfere with the light that reflected off the surface.

A JA Woollam M-88 ellipsometer was used to measure the amorphous silicon film thicknesses at angles of 60°, 67°, and 74° and wavelengths from 281.6 to 765.7 nm. The i-Si and n-Si films on the different substrates were determined to be 70 and 96 nm thick, respectively. Additional thicknesses were deposited on quartz, ranging from 38 to 172 nm.

2.2.8. Resistivity Characterization

Resistivity measurements shed light on the electronic transport as well as the connectivity of the morphology and structure of the films. Two techniques were used to determine the resistivities of the SWCNT and the laser-crystallized silicon films.

2.2.8.1. CNT Resistivity Characterization

For the SWCNT bilayer, capacitive frequency measurements were recorded, from which the resistivity of the films were extracted. The samples were prepared by depositing an interdigitated electrode pattern on the pre-strained bilayer films as shown in Figure 8. The electrodes were sputtered on the CNT bilayer films, using a Kurt J. Lesker CMS-18. A 125 μm thick polyimide mask of the electrodes was cut out using the HIPPO laser and was taped to the PDMS substrate on top of the bilayer. The strain stage, with the pre-strained bilayer secured, was mounted in the sputtering chamber. A 10 nm chromium layer was deposited initially to ensure good adhesion to the substrate, followed by 100 nm of gold without breaking vacuum.

An Agilent B1500A semiconductor device analyzer was utilized to measure the capacitive reactance of the CNT bilayers. Two probes were connected to the electrodes, an alternating current ramping up from 1 kHz to 1 MHz was applied to the sample, and the sheet resistance was recorded.

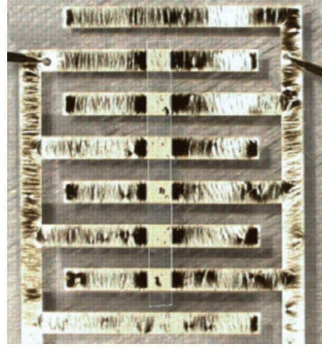

Figure 8. Electrode pattern on a SWCNT film.

2.2.8.2. Laser-Crystallized Silicon Resistivity Characterization

A Cascade Microtech 4-point probe (C4S-44/S) connected to a Keithley 2400 source meter was used to determine the resistivity of the laser-crystallized silicon films. The probe spacing was 1 mm. The outer probes of the configuration provide the current and the inner probes measure the potential difference. In this configuration, the sheet resistance for a 4-point probe setup is given by[34]:

$$R_s = \frac{V}{I}\frac{\pi}{\ln(2)}. \tag{2.4}$$

The resistivity is then the product of the sheet resistance and the film thickness. Three parallel and three orthogonal measurements were taken for each sample and the calculated resistivities were averaged.

2.2.9. Tensile Pull Tester

An Instron 5545 Tensile Tester with a 100 N load cell was used to determine the Young's modulus of the PDMS substrates. The instrument measures the strain in the substrate over a

series of applied loads. The Young's modulus was calculated from the slope of the linear portion of the stress vs. strain curve. The PDMS substrates used for compression experiments had a Young's modulus of 2.6 MPa.

2.2.10. Strain-induced Elastic Buckling Instability for Mechanical Measurements

To obtain the modulus of elasticity for the CNT component of the bilayers, a modified strain-induced elastic buckling instability for mechanical measurements (SIEBIMM) technique was applied. SIEBIMM is a quick and inexpensive technique that can be used to determine the modulus of elasticity of thin films.[35] Other techniques require extensive preparation, such as removing the substrate[36], or expensive instrumentation, such as AFM.[37] The SIEBIMM technique utilizes the periodicity of the buckling pattern that forms when stiff films are compressed. The Young's modulus is related to the buckling wavelength with the expression:

$$\bar{E}_f = 3\bar{E}_s\left(\frac{\lambda}{2\pi h_f}\right)^3 \tag{2.5}$$

where λ is the wavelength of the harmonic wrinkles, h_f is the film thickness, and $\bar{E}_i$ is the plane-strain modulus of the substrate $(i = s)$ or the film $(i = f)$. The plane strain modulus is defined as

$$\bar{E}_i = \frac{E_i}{1 - \upsilon^2} \tag{2.6}$$

where υ is the Poisson ratio.

Equation 2.5 is a linear approximation and is valid for small displacements. At large strains, a correction factor for the wavelength[38] must be implemented and is given by

$$\lambda = \frac{\lambda_o}{(1+\varepsilon)(1+\xi)^{\frac{1}{3}}} \tag{2.7}$$

where ε is the strain and $\xi = 5\varepsilon(1+\varepsilon)/32$.

The relation becomes more complicated when a second distinct layer is introduced in the film. Stafford *et al*[14] and Nolte *et al*[39,40] derived an equation relating the effective modulus to the moduli and thicknesses of the component films. Applying these equations to PS capped SWCNT film, the Young's modulus can be calculated using the expression

$$E_{CNT} = \frac{1}{2}\left[(1+n)^3 E_f - 2nB_n E_{PS} + \sqrt{\left\{2nB_n E_{PS} - (1+n)^3 E_f\right\}^2 - 4\left\{n^4 E_{PS}^2 - n(n+1)^3 E_{PS} E_f\right\}}\right] \quad (2.8)$$

where $B_n = (2n^2 + 3n + 2)$, $n = h_{PS}/h_{CNT}$, and E_i is the modulus of the composite bilayer film $(i = f)$, the SWCNT component of the bilayer $(i = CNT)$, and the polymer component of the bilayer $(i = PS)$. All of these results are rigorously applicable to elastic materials only. Here, the SWCNT films are plastic, so all results need to be extrapolated to the limit of zero strain, as discussed below.

The modulus of the PS and the bilayer were calculated in parallel using Equations 2.5 and 2.8. The film thicknesses were measured using AFM, as described in Chapter 2.2.2, and the Young's modulus of the substrate was determined from the Tensile Pull Tester as outlined in Chapter 2.2.6. The wrinkling wavelengths were measured from the optical micrographs using an image editing software. Five lines spanning the images were drawn and the number of wrinkles that intersected each line were tallied and averaged for each image. The average wavelength was calculated and converted to µm. The Poisson ratios were found in literature to be 0.5 for PDMS,[5] and 0.33 for PS[41] and CNTs[5]. Since PS and CNT share identical Poisson ratios, the same Poisson ratio (0.33) was used for the bilayer film. Through careful optical imaging in reflection, it is possible to detect and measure the fundamental wrinkling harmonic, although care has to be taken to distinguish this structure from other larger-scale features such as ridges and folds.

3. PHYSICS OF CARBON NANOTUBES

CNTs have been widely studied for the past couple of decades due to their wide-ranging potential applications. They possess extraordinary mechanical, thermal, and conductive properties, which make them ideal candidates for thin, flexible electronics as well as additives in composites to enhance material properties. Properties of individual SWCNTs will be covered in the following subsection, followed by the mechanics and electron conduction of SWCNT membranes in response to a compressive strain.

3.1. Individual Carbon Nanotubes

SWCNTs are polymer-like nanomaterials with extremely high aspect ratios. They exist with diameters ranging from 0.3 to larger than 3 nm[42] and lengths ranging from 100 nm to 100 µm.[43] SWCNTs are composed of interlocking hexagonal rings of carbon atoms that form a tube. Individual tubes are called single-wall CNTs (SWCNTs), whereas a tube nested within another is called a double-wall CNT and more than two concentric CNTs is considered a multi-wall CNT. Only SWCNTs will be considered in this section, as these are the materials used in the work and the properties of double- or multi-wall CNTs vary from those of SWCNTs.

A SWCNT can be conceived of as a sheet of graphene rolled to form a cylinder. The "twist" in the cylinder is described by the chiral vector with components (n, m), where n and m are integers and are shown in Figure 9. The chirality of the SWCNT determines its properties, primarily the diameter and the electronic type. Special chiralities of SWCNTs are armchair and zig-zag SWCNTs, which have chiral indices of (n, n) and (n, 0), respectively. Armchair SWCNTs are true metallic CNTs and all other SWCNTs are semiconducting. However, SWCNTs for which the difference in the chiral components, $n - m$, is an integer multiple of 3, have a very small bandgap and are commonly approximated as metallic SWCNTs.[42]

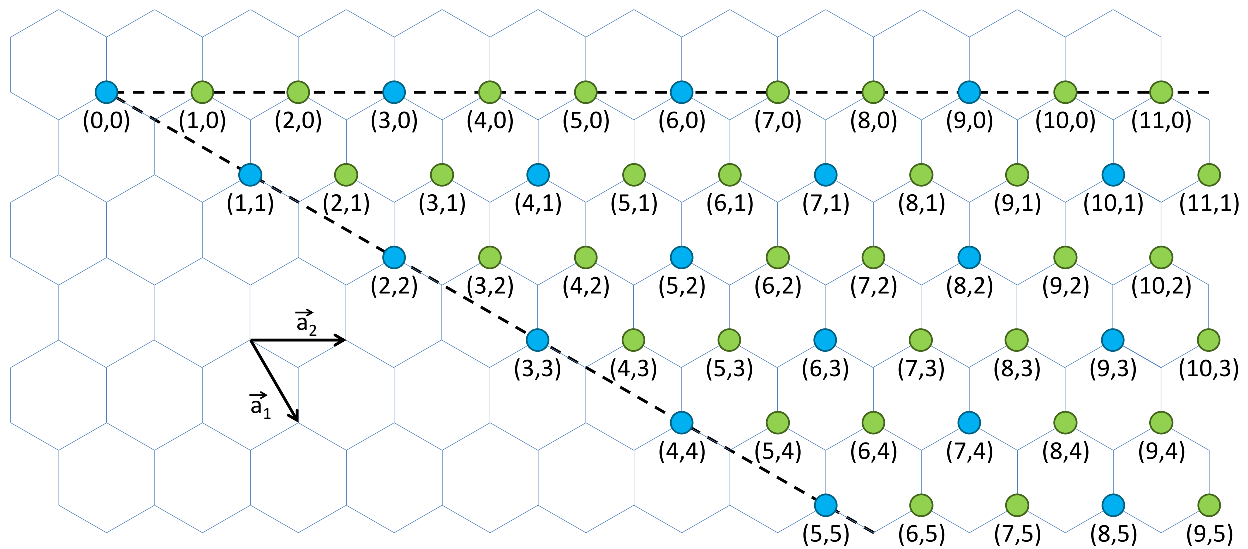

Figure 9. Chirality map of SWCNTs. The blue dots represent metallic SWCNTs and the green, semiconducting SWCNTs.

The superb mechanical properties of SWCNTs arise from the bond strength of the carbon atoms and the structure of the nanotube. Each carbon atom is bonded to three adjacent carbon atoms, hybridizing the *s* and *p* orbitals to form three sp^2 orbitals. The bond energy between the carbon atoms is relatively strong at 2.7 eV,[44] and because of the geometery, at least 10 bonds must be broken to cleave a SWCNT[45] which results in an extremely high tensile strength, the stress at which a material fails. Theoretical models predict a tensile strength of 150-180 GPa[46], however, experimental data has only achieved a tensile strength of 70 GPa, which is likely due to defects in the SWCNTs. The presence of defects is inevitable, but the defect density in SWCNTs is much lower compared to other strong materials such as steel, which is riddled with grain boundaries. Another common mechanical metric is the Young's modulus, a measure of the deformation of a material under a given stress. Theory predicts SWCNTs have a Young's modulus of approximately 1 TPa.[47] Again, the experimental data is a bit weaker, but relatively good in terms of agreement.[48,49] Unlike other materials with comparable mechanical properties,

SWCNTs have a low density of roughly 0.8 g/cm^3. The mechanical properties of SWCNTs and comparable materials are shown in Table 1.

Table 1. Mechanical properties of CNTs, copper, and polystyrene.

Material	Modulus (GPa)	Tensile Strength (MPa)	Density (g/cm^3)
CNTs	650-1000[42,46]	20,000[46]	0.8-1.6
Copper	130[50]	170[51]	9.0
Steel	180[52]	620[52]	8.05
Polystyrene	3-3.5[53]	0.3[54]	1.1

The mechanical properties of CNTs significantly exceed those of copper and steel, but CNTs have a density comparable to polystyrene.

The electronic properties of SWCNTs are tied to their chirality, which also determines the diameter and is given by $d = \frac{a}{\pi}\sqrt{n^2 + m^2 + mn}$ where a is the C-C bond length. The band structure of SWCNTs can be approximated using the electronic structure of graphene by applying a periodic boundary condition. The dependence of SWCNT electronic type on chirality arises from the periodic boundary condition imposed on the wave function.

SWCNTs also exhibit unique optical properties due to the van Hove singularities present in the density of states. Van hove singularities are discontinuities in the the density of states that are typical in one-dimensional quantum systems. The density of states is given by[55]:

$$g_n(\varepsilon)d\varepsilon = \int_{S_n(\varepsilon)} \frac{dS}{4\pi^3} \frac{1}{|\nabla\varepsilon_n(\boldsymbol{k})|} \tag{3.1}$$

where $\varepsilon_n(\boldsymbol{k})$ is the energy. van Hove singularities occur when dispersion relation, $\varepsilon_n(\boldsymbol{k})$ is at an extremum[56]. As allowed by optical selection rules, optical transitions occur between corresponding van Hove singularities on opposite sides of the Fermi level. The transitions between these discrete energy levels result in narrow peaks in the optical absorption spectra[57].

Raman spectroscopy is a useful tool for characterizing SWCNTs[58]. Raman spectra of SWCNTs contain four phonon modes of primary interest (Figure 10). The radial breathing mode (RBM) represents the expansion and contraction of the SWCNT along the radial axis and occurs near 100-500 cm^{-1}. It has been shown experimentally that the RBM is related to the diameter of the SWCNT through $\omega_{RBM} = \frac{A}{d_t} + B$, where A and B are fitting parameters determined from experiment.[59] The G-band corresponds to the tangential vibration of carbon atoms and is composed of G^+ (1590 cm^{-1}) and G^- (1570 cm^{-1}) sub-bands that represent vibrations along and perpendicular to the tube axis. The intensity of the D (1350 cm^{-1}) and G' (2700 cm^{-1}) bands depend on defects in the structure of the SWCNT. For this reason, the intensity ratio of the G to D band is a common metric of the presence of defects in SWCNTs.[60]

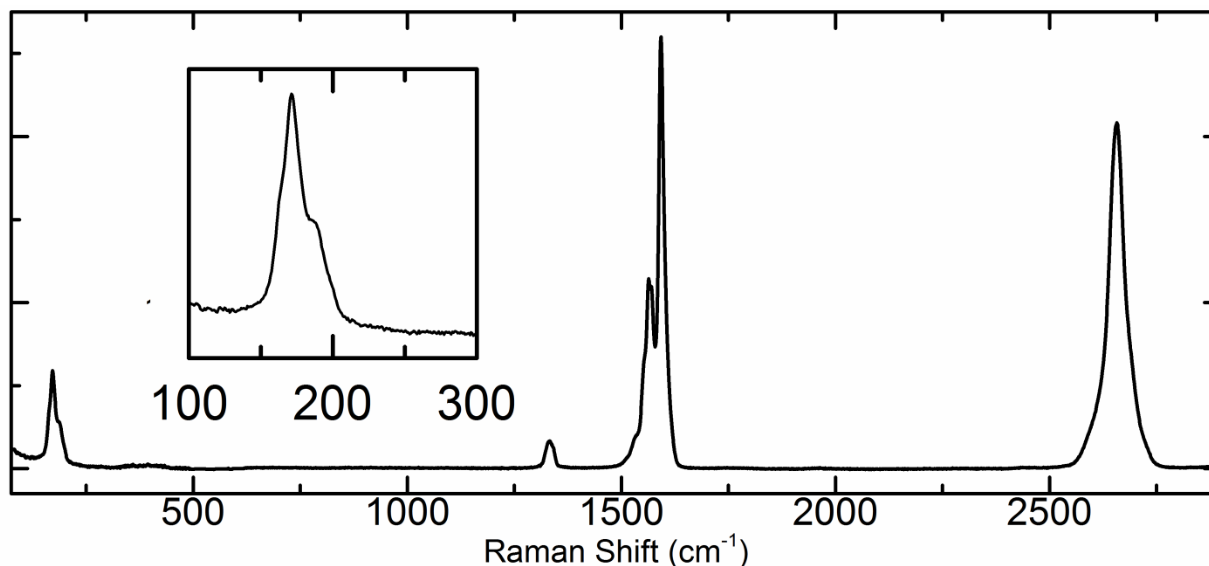

Figure 10. Raman spectra of a metallic SWCNT film. The inset shows the RBM with finer resolution. The RBM is a convolution of at least two peaks, which means the metallic SWCNT film contains with a variety chiralities.

The three popular techniques used to synthesize SWCNTs are laser ablation, arc discharge, and chemical vapor deposition (CVD).[61-64] The yield, length, chirality, and structural

type of CNT - single-wall *vs*. multi-wall - all depend on the system parameters, such as pressure, temperature, ambient composition, etc. In a laser ablation setup, argon gas flows down a heated tube towards a graphite target doped with a catalyst. A laser is used to ablate the carbon target, typically with a wavelength of 1064 or 532 nm. Scott *et al*[62] studied the laser ablation process and described it as follows. A carbon plume is formed, estimated to reach 3000-4000 K, and as the carbon cools, it condenses to form clusters. The vaporized catalysts attach to the carbon preventing the clusters from closing. The CNTs grow until the catalyst is exhausted or the system has cooled. Without the catalyst, the laser ablation technique predominantly produces small fullerenes.[65]

Like laser ablation, arc-discharge relies on the condensation of ablated carbon to form CNTs. Shi *et al*[63] used an arc-discharge setup using a Y-Ni alloy as a catalyst embedded in the anode. The cathode was sharpened to a point and mounted 5 mm from the cathode. An arc with a current of 40-100 A was generated between the electrodes in a helium atmosphere at 100-700 torr. The CNTs then condense on the walls of the apparatus in the same manner as described for laser ablation.

CVD is a much more controlled synthesis of CNTs. CVD is a process that exposes a substrate to a precursor that reacts with or decomposes on the substrate. To synthesize CNTs, a catalyst is deposited on the substrate and a carbon-based gas, i.e. methane, ethane, ethylene, acetylene, etc, decomposes to form the CNTs. Many variants of CVD exist and result in samples with different characteristics. The growth mechanism is not fully understood, but two primary theories exist.[64] One suggests that growth occurs from the base, in which the cap of the CNT forms first on the substrate, and by exposing the base to carbon, the shaft of the CNT grows. The other theory, however, suggests that the CNT grows from the tip, where new carbon atoms attach

to the CNT and growth continues until the CNT is capped. Different morphologies can be produced using different CVD parameters, including upright forests or random spaghetti-like films.[61]

The laser ablation and arc-discharge techniques produce CNTs with a variety of lengths and diameters, as well as other carbon allotropes. Recently, density gradient ultracentrifugation methods to separate CNTs based on their length,[25] electronic type,[27] and chirality[66] have been developed.

3.2. CNT Film Properties

Many of the excellent properties individual CNTs possess are due to individual structure of CNTs, but those properties are not fully realized when CNTs are used to form a film. The attractive van der Waals forces that hold adjacent CNTs together is much weaker than the carbon-carbon bonds of individual CNTs, and electron transport is hindered due to the interfacial tunneling needed at CNT-CNT junctions. Although CNT films are weaker and less conductive than their individual components, they still exhibit excellent properties.

As mentioned earlier, CNT films can be grown directly on the substrate when synthesized *via* CVD. To produce films from aqueous solutions of laser ablation and arc discharge SWCNTs, vacuum filtration techniques are commonly used, as described in Chapter 2. Much research has been done on the mechanics and optical and electronic properties of films produced *via* vacuum filtration and this will be the focus for the remainder of this section.

SWCNT films constructed through vacuum filtration are semi-porous membranes. TEM and SEM images give insight into the structure of the films and are shown in Figure 11. TEM images of SWCNT films show what appear to be large nanotubes, but these are actually bundles of SWCNTs. The SEM image depicts the porosity of films, and small angle light scattering

(SALS) reveals the films have a mass fractal structure, with $I(q) \propto q^{-D}$ where $D = 1.72$, suggesting they can be modeled as 2D diffusion-limited rod aggregates.[5]

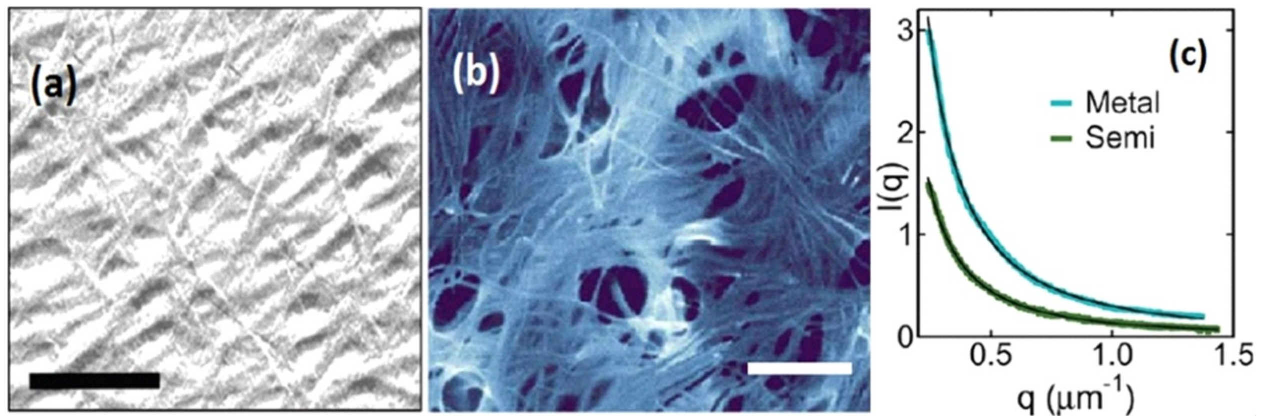

Figure 11. TEM, SEM, and SALS plot of SWCNT films. The film structure is shown in the a) TEM and b) SEM images of a film. Scale bars are 200 nm for the TEM image and 250 nm for the SEM image. SALS of a metallic and semiconducting SWCNT films both have exponents of 1.72, suggesting they have the same structure.[5]

SWCNTs interact in the film *via* van der Waals attraction, excluded-volume repulsion, and sliding friction.[67] The strong van der Waals interactions can be thousands of k_bT deep, and arise primarily from the conductive nature and the large aspect ratios of SWCNTs. Smaller diameter SWCNTs have been shown to have slightly stronger van der Waals attraction than larger diameter SWCNTs,[68] due to the higher effective electron density present in narrower SWCNTs. Surprisingly, this dependence of the strength of van der Waals attraction on SWCNT diameter/chirality leads to interesting and measurable differences in the strain response of SWCNT films[4]. Although the van der Waals forces between SWCNTs are quite strong, they are still the weak link in CNT films. When extrapolated to zero strain, the Young's modulus of a SWCNT film can be on the order of 100 of GPa,[4] in comparison to the 1 TPa Young's modulus of an individual SWCNT.

The semi-porous structure, strong van der Waals attraction, and limited sliding friction inherent to SWCNT films allow the nanotubes to rearrange and bundle perpendicular to applied

strains, a phenomenon is known as strain softening.[5] As noted previously, this restructuring of the SWCNTs can have a detrimental effects on the mechanical and electrical properties of the film. The isotropy of an uncompressed SWCNT film can be a source of the mechanical resilience, whereas aligned SWCNT films are less so due to fewer van der Waals contact points.

Extensive work was done by Harris *et al* on the strain response of semiconducting and metallic SWCNT films.[4,22,28] Using the SIEBIMM technique, described in Chapter 2, applied to pure SWCNT films, they were able to deduce the Young's modulus of several films as a function of film thickness and electronic type. The SIEBIMM technique is a linear model applied to homogenous films, however, recently it has been argued that it can be used equally well for non-homogeneous films.[69] SWCNT films produce disordered wrinkling patterns due to the non-uniformity of the film. As can be seen in Figure 12, the overall wrinkling pattern does not correspond to a uniform, periodic structure, as one sees for uniform polymer films. Rather, the wrinkles localize and bifurcate to reduce the overall stress of the film.[69] We can think of the disordered wrinkling pattern as arising from the presence of defects in the film. Bifurcation occurs when defects prevent a single wrinkle from spanning the film. Bifurcations obstruct the underlying periodic pattern of the film, which we refer to as the fundamental. These localizations also result in pinches in the film that have much higher amplitudes than neighboring wrinkles, and the presence of these tall creases can dominate the more subtle neighboring wrinkles as can be seen for SWCNTs in Figure 12a and for PS in Figure 12c.

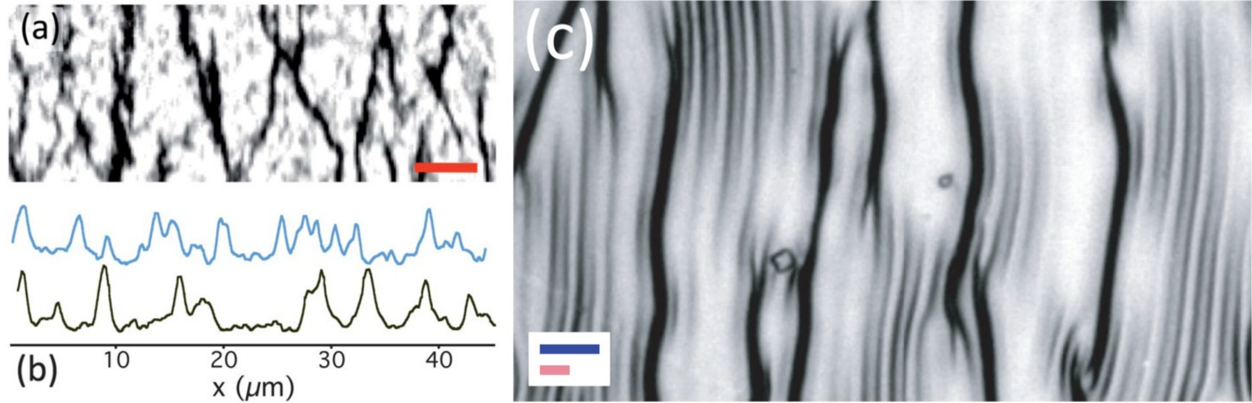

Figure 12. SWCNT and a PS films under 5 % compressive strain on PDMS. a) A reflection micrograph shows the wrinkle pattern of the 30 nm SWCNT film. The scale bar represents 10 μm. b) Profiles of metallic (blue) and semiconducting (brown) films obtained from the intensity of the reflection micrograph. c) A reflection micrograph of a PS film compressed at 5 % strain shows the creases with the more subtle wrinkles between them.

To account for strain softening, Harris *et al* let the SWCNT modulus be strain dependent. The Young's modulus of the SWCNT films decreased significantly more than that predicted by nonlinear elastic theory, as seen in Figure 13. At higher strains, the SWCNTs bundle significantly, and the Young's modulus is substantially reduced. The plots are scaled by the plateau modulus, the Young's modulus of an uncompressed film, and the yield strain, the strain at which the Young's modulus begins to decay.

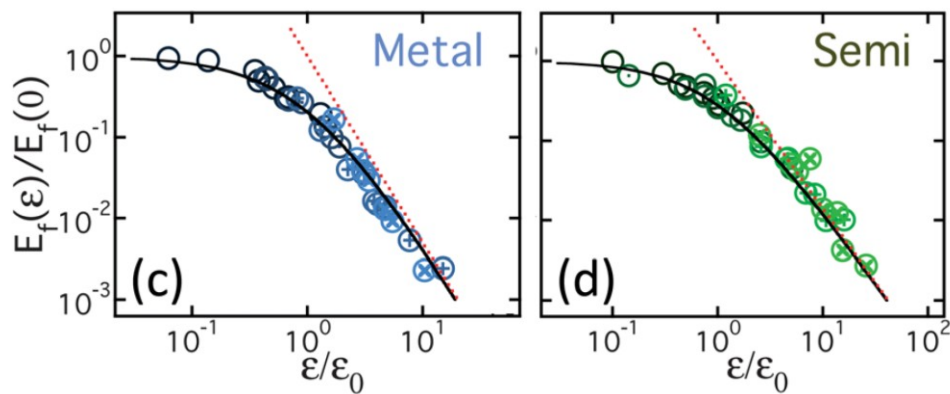

Figure 13. Reduced Young's modulus of metallic and semiconducting SWCNT films.[4]

Many properties of SWCNT films depend on the film thickness, as well as the lengths and diameters of the CNTs that make up the film. The percolation threshold largely depends on

the aspect ratios of the SWCNTs. Percolation can be characterized by two different properties: rigidity percolation and connectivity percolation. The rigidity percolation threshold is the minimum thickness at which a film has quantifiable mechanical properties, such as the Young's modulus, whereas the connectivity percolation threshold is the minimum thickness at which a film can carry current. The data in Figure 14 support a larger aspect ratio for the semiconducting SWCNTs in comparison to the metallic SWCNTs, which is also evident in the distribution of lengths and diameters shown in Figure 15. The semiconducting SWCNTs have a lower connectivity and rigidity percolation threshold than the metallic SWCNTs due to this difference in aspect ratio. The smaller diameter allows for a denser packing of CNTs, resulting in a thinner film with measurable mechanical properties, and longer SWCNTs more readily span the film, resulting in a lower connectivity percolation thickness.

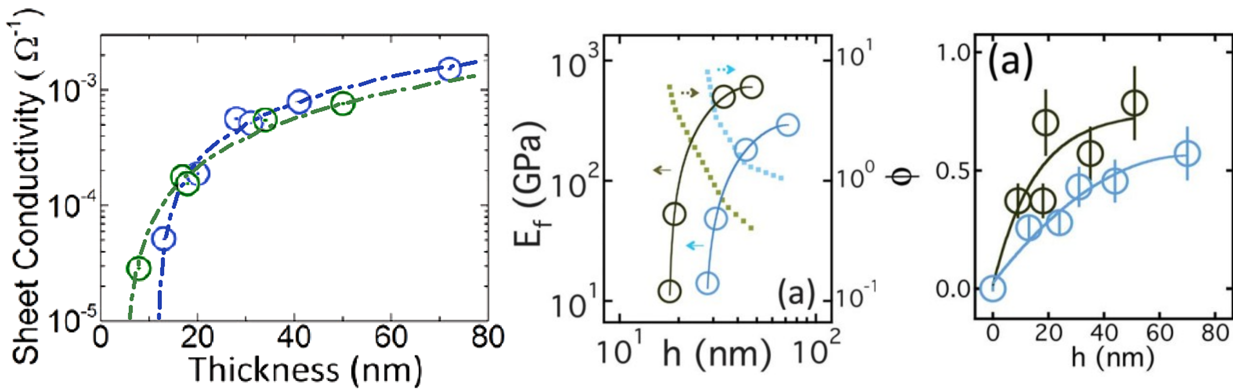

Figure 14. a) Sheet conductivity shows the longer semiconducting SWCNTs (green) have a lower connectivity percolation threshold than metallic CNTs (blue). b) The semiconducting SWCNTs have a narrower diameter resulting in a film with a lower rigidity percolation threshold due to the ability of the SWCNTs to form denser films, as shown in c).

Beyond this difference in aspect ratio, the semiconducting SWCNT films have higher Young's moduli than the metallic SWCNT films, which we attribute to the stronger van der Waals attraction. Although they tend to have a higher Young's modulus, they have a lower yield strain, again, likely due to the difference in the van der Waals forces. The stronger attraction

between the semiconducting SWCNTs causes them to bundle more readily in comparison to the metallic SWCNTs.

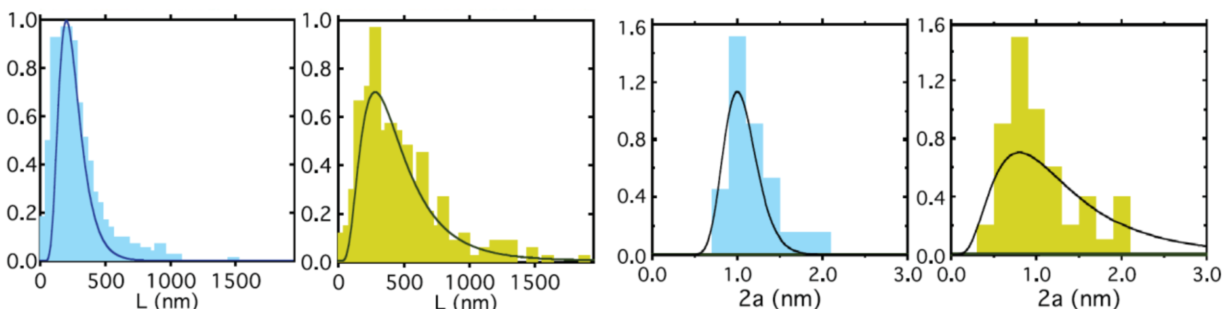

Figure 15. Length and diameter distributions of metallic (blue) and semiconducting (yellow) SWCNTs. The metallic SWCNTs are shorter and have a larger diameter.

As evident in Figure 14, the sheet conductivity of the undoped metallic and semiconducting SWCNTs do not differ drastically. However, the strain response of the sheet conductivity [Figure 16], varies significantly with the two types of films. Subsequent work by our group has improved this strain response considerably, as evidenced below by the measurements I performed on both polymer-capped and uncapped SWCNT films.

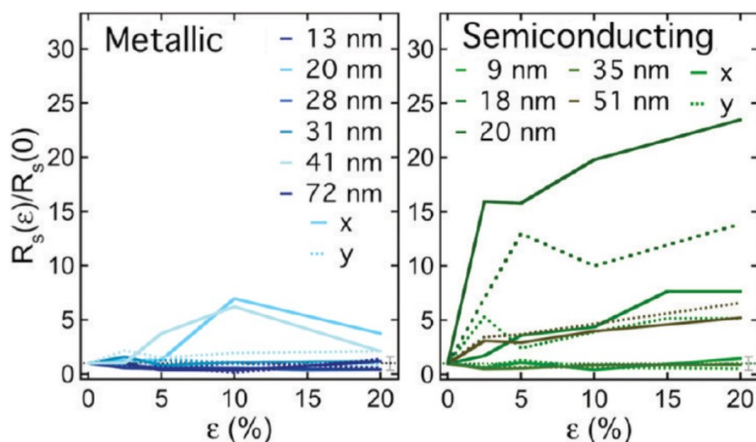

Figure 16. The strain response of the sheet resistance for semiconducting compared to metallic SWCNTs. Although the metallic SWCNTs appear to be much more resilient than the semiconducting SWCNTs, much of the difference in this figure is attributable to residual excess surfcactant.[28]

4. WRINKLING AND FOLDING OF NANOTUBE-POLYMER BILAYERS

4.1. Mechanical Strain-Response

As discussed in Chapter 3, SWCNT films have exceptional mechanical and electronic properties, however, at high compressive strains, they can appear to be quite fragile because the strong van der Waals attractive forces and the porosity of the film give rise to strain softening. For applications in flexible electronics, the films must be resilient. In an attempt to reinforce the SWCNT films *via* excluded volume interactions in bilayer geometries that have relevance to simple device architectures, the voids in the SWCNT network were filled with polymer, as motivated in Chapter 2.1.1. The presence of the polymer in the semi-porous SWCNT membrane exploits excluded volume to prevent CNTs from aligning, as shown schematically in Figure 17. As we demonstrate below, the presence of the polymer capping layer has a significant impact on the modulus and the yield strain for thin SWCNT films.

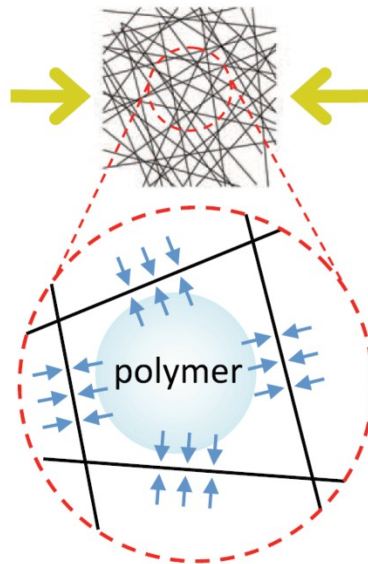

Figure 17. A schematic denoting the effect the polymer filler has on a compressed SWCNT film.

Reflection optical micrographs show the wrinkling patterns of several films at different strains in Figure 18. Homogeneous films produce more uniform wrinkling patterns, such as the

PS film in Figure 18a. However, non-uniformSWCNT films [Figure 18b] or PS films[Figure 18c and Figure 18d] exhibit localizations and bifurcations. The localizations in the film give rise to a superposition of faint wrinkles and dark ridges with different wavelengths. The faint wrinkles have a mean spacing of λ_o, the fundamental wavelength, whereas the darker wrinkles have a mean spacing of twice to four times the fundamental wavelength. Figure 18d shows a comparison between a PS film (top) and a capped SWCNT film (bottom) of comparable thickness. The white bars represent twice the fundamental wavelength for each film. The capped film has a longer fundamental wavelength, and thus by Equation 2.5, a higher Young's modulus.

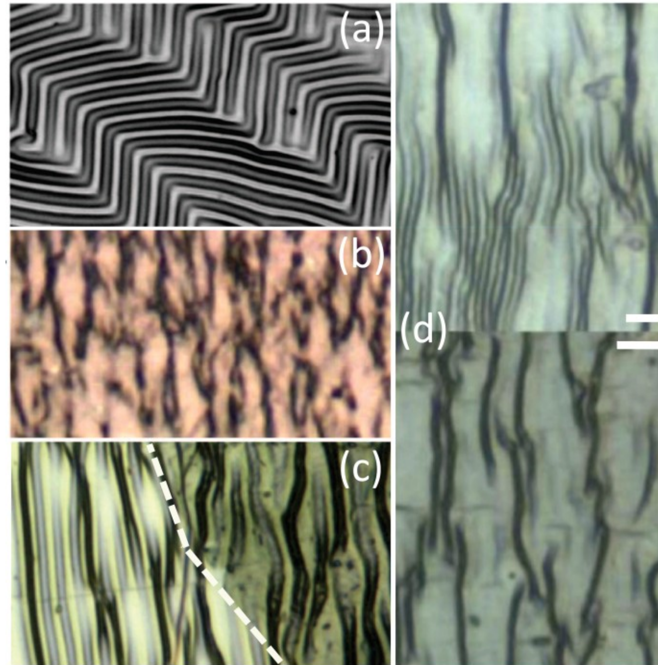

Figure 18. Reflection optical micrographs of compressed films.[70] (a) A 125 μm thick PS film on PDMS at 2.5 % strain (width = 110 μm). (b) A 35 nm thick metallic SWCNT film at 10 % strain (width = 25 μm). (c) A 32 nm thick semiconducting SWCNT film covered with a 125 nm thick PS film at 10 % strain. The dashed line indicates the interface of the capped SWCNT film and the pure PS film (width = 90 μm). (d) A 50 nm PS film (top) and a capped SWCNT film (bottom, $h_{PS} = 33$ nm, $h_{PS} = 16$ nm) at 5 % strain. The two images show a comparison of wavelengths (the scale bars represent twice the fundamental wavelength) of the composite and a PS film of comparable thickness.

Cross-sectional TEM images of the composite were taken to determine the internal structure of the capped film. A 125 μm thick PS film was deposited on a 60 nm metallic SWCNT film and the sample was microtomed as described in Chapter 2. The TEM images show the PS infiltrating the SWCNT film by roughly 25 nm, which is evident in the TEM image in which the PS has peeled away from a significant portion of the SWCNT film.

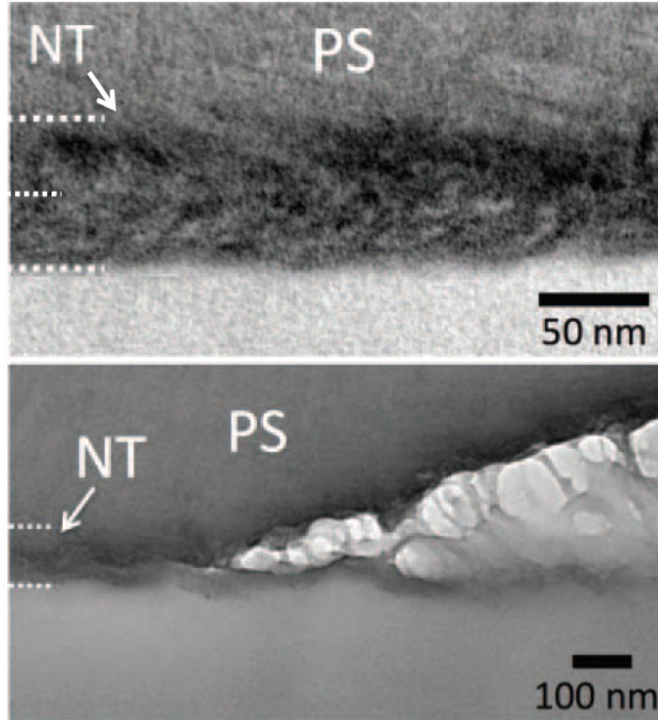

Figure 19. TEM cross-sectional images of the SWCNT-PS interface.[71] The bottom image shows the SWCNTs being removed with the PS as it is peeled off the 60 nm metallic SWCNT film.

The Young's modulus data of the SWCNT layers were calculated using Equation 2.8, and plotted against the strain. An equation of the form

$$E = E_o\left(1 + \frac{\varepsilon}{\varepsilon_o}\right)^{-\alpha} + E_\infty \tag{6.1}$$

was fit to the data, where E_o is the low strain modulus, E_∞ is the background (the modulus at infinite strain), ε_o is the yield strain, and α is a critical exponent measured to be 2.3 and 1.85 for uncapped metallic and semiconducting films, respectively.[4] To reduce the number of free

parameters, the critical exponent is assumed to be unaffected by the polymer. The data suggest [Figure 20] that for SWCNT films thinner than the infiltration depth of 25-30 nm, the PS has a positive reinforcing effect. However, for films thicker than the infiltration depth, the PS appears to negatively affect the SWCNT film properties.

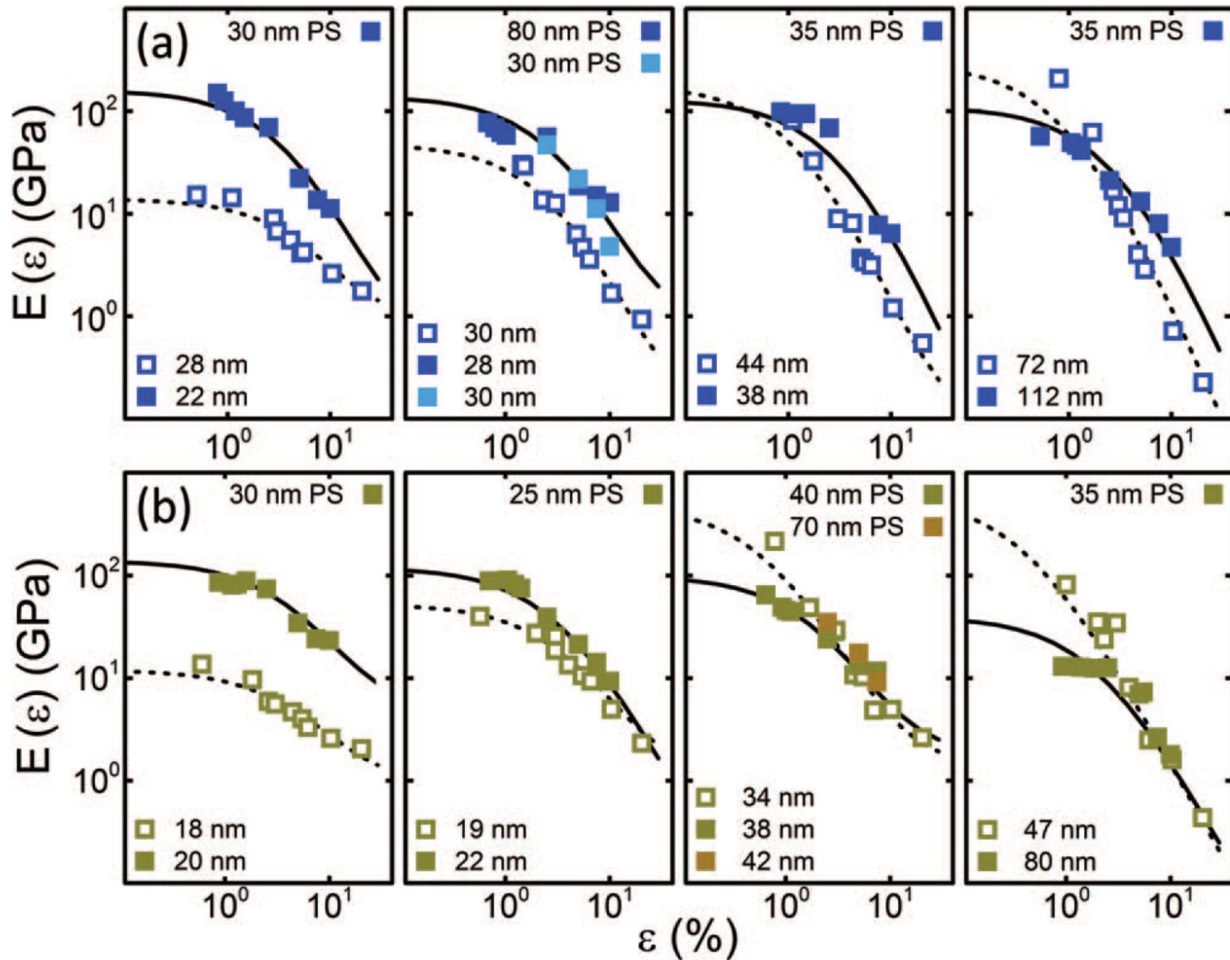

Figure 20. (a) Metallic and (b) semiconducting SWCNT film moduli vs. strain with fits using Equation 6.1. Open markers represent uncapped SWCNT data and solid markers represent capped SWCNT data. The lower legend thicknesses are the SWCNT film thicknesses, and the upper legend is for the PS film thicknesses.[71]

The zero-strain modulus and yield strain data were extracted from the fits and were plotted against the film thicknesses for each electronic type. The plot of the zero strain modulus [Figure 21] more clearly shows the trend of how the polymer affects SWCNT films thinner and

thicker than the infiltration depth. The uncapped data shown was published by Harris *et al*,[4] and was used to determine percolation threshold using the relation $E(0) = \tilde{E}\left(\frac{h_{CNT}}{h_c} - 1\right)^{\beta}$ where h_c is the rigidity percolation threshold and β is a fitting parameter. The fitting parameters used in Figure 21 are: $h_c = (27 \pm 4)$ nm, $\beta = 1 \pm .05$, and $\tilde{E} = (350 \pm 30)$ GPa for the metallic SWCNTs, and $h_c = (17.5 \pm 4)$ nm, $\beta = 1 \pm .05$, and $\tilde{E} = (500 \pm 30)$ GPa for the semiconducting SWCNTs. The capped films exhibited a different trend, and a power law of the form $h_{CNT}^{-\beta}$ was fit to the data, where $\beta \approx 3.5$ for the metallic films and $\beta \approx 3$ for the semiconducting films. The PS reduces the rigidity percolation threshold of pristine SWCNT films in the capped films. The capped SWCNT films, however are above the connectivity percolation thresholds of (12 ± 2) nm and (6 ± 2) nm for the metallic and semiconducting films,[28] respectively.

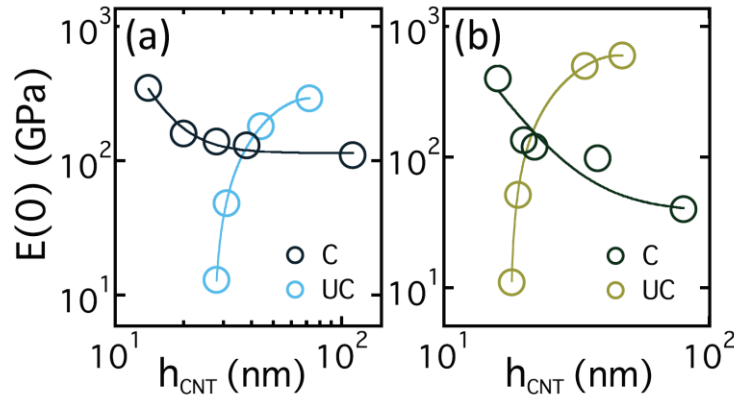

Figure 21. Zero-strain modulus of (a) metallic and (b) semiconducting SWCNT films. The light data represent the uncapped films and the dark data represent the capped data.[71]

For SWCNT films thinner than the infiltration depth, the PS sufficiently permeates the CNT film to create a composite material. The rule of mixtures[72] can be used for a crude estimate of the modulus of the composite as

$$E_c = \phi_{CNT} E_{CNT} + (1 - \phi_{CNT}) E_{PS} \qquad (6.2)$$

where ϕ is the volume fraction of the designated material and E_{PS} and E_{CNT} are the Young's modulus of the PS and SWCNT. Using $E_{CNT} = 1.2$ TPa[73] and $E_{PS} = 2$ GPa (as measured in experiment) and assuming a 20 nm thick SWCNT film, the volume fraction[4] is 0.3 for metallic CNTs and 0.45 for the semiconducting CNTs. The maximum Young's modulus of the composite material is estimated to be 360 GPa for the metallic CNT film and 540 GPa for the semiconducting SWCNT films, in relatively good agreement with the extracted zero-strain moduli of 350 GPa and 400 GPa for the metallic and semiconducting SWCNT films, respectively.

For SWCNT films thicker than the infiltration depth, the Young's modulus is reduced compared to pristine SWCNT films. When the PS permeates a portion of the SWCNT film, it appears to act as a plasticizer, reducing the modulus yet enhancing the yield strain [Figure 22].

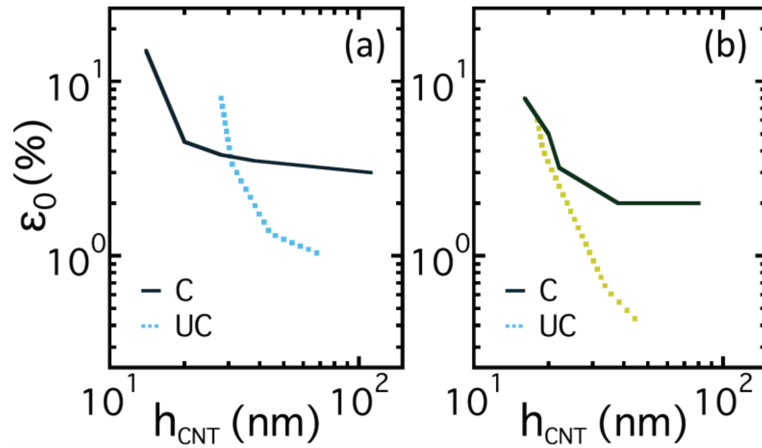

Figure 22. Yield strain of (a) metallic and (b) semiconducting SWCNT films. The data was extracted from the fits in Figure 20 and plotted against thickness. The dark lines represent the capped data and the light represent the uncapped data.[71]

4.2. Electronic Strain-Response

The addition of the polymer further inhibited the conductivity of the CNT films. Figure 23a and Figure 23b show a plot of the sheet resistance of two capped and uncapped metallic

SWCNT films at different strains as it was compressed and stressed repeatedly, and Figure 23c shows the sheet resistance of the unstrained films after several compressive strains have been applied. The compressive strains result in plastic deformation, permanently affecting the sheet conductivity of both the capped and uncapped films. The capped films, however, consistently had slightly higher sheet resistances than the uncapped. The sheet resistance of the 20 nm semiconducting film even improved after compression/stretching cycles. The improvement in conduction may be due to enhanced interfacial contact between adjacent CNTs. Overall, the presence of the polymer impedes contact between CNTs during compression.

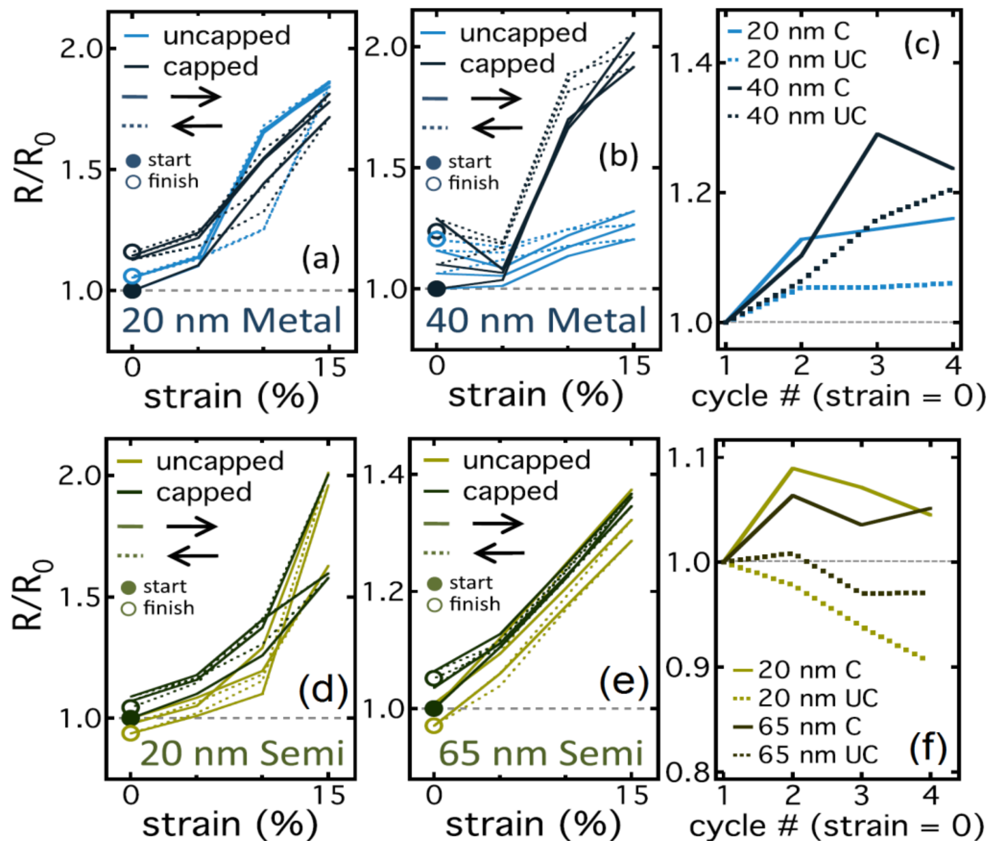

Figure 23. Normalized sheet resistance for compression/stretching of uncapped and capped films.[71] (a) and (b) are 20 nm and 40 nm thick metallic films, and (d) and (e) are 20 nm and 65 nm thick semiconducting films. The unstrained sheet resistance after each cyclical compression and extension was plotted as a function of the cycle number for the (c) metallic films, and (f) the semiconducting films. The improved stability of the strain response, in comparison to that depicted in Figure 16, can be attributed to cleaner SWCNT films with less residual surfactant.

4.3. Conclusion

The strain response of the capped films suggests that the capped films exist in two regimes. For SWCNT films thinner than a polymer infiltration distance, the filler enhances the Young's modulus of the SWCNT film, and even creates a rigid composite film below the rigidity percolation threshold of the SWCNT component. However, for SWCNT films thicker than the penetration depth of the top layer, the PS appears to act as a plasticizer, reducing the modulus and enhancing the yield strain. An infiltration depth of approximately 25 nm was achieved by heating the sample to the glass transition temperature of the filler material under vacuum for one hour. A deeper infiltration depth would be needed to reinforce thicker films.

Although two mechanical behaviors in response to a capping polymer layer are suggested, the sheet resistance strictly increases, regardless of SWCNT thickness. This is likely due to reduced interfacial contact between adjacent SWCNTs. To counter the increase in sheet conductivity, a conductive filler material could be used, such as conjugated polymers or metallic nanoparticles. These materials would not only enhance the Young's modulus through excluded volume interactions, but would also enhance electron transport between adjacent SWCNTs.

6. PHYSICS OF LASER-CRYSTALLIZATION OF SILICON

Laser-crystallization of silicon relies on using the energy of a laser to raise the temperature of the amorphous silicon film to its melting temperature. As the film rapidly cools, the film crystallizes as polycrystalline silicon. The crystallization process and the important parameters will be discussed in the subsections of this chapter.

6.1. Heat Transfer and Phase Change

The laser is the heat source for the amorphous silicon film. Because the absorption coefficient is wavelength-dependent, the laser wavelength is an important parameter. The penetration depth of the laser intensity can be determined using the Beer-Lambert Law,

$$I(\lambda, x) = I_o e^{-\int \alpha(\lambda) dx} \quad (4.1)$$

where I_o is the intensity at the surface, x is the depth of the material, and α is the absorption coefficient, which is plotted in Figure 24. Thicker films can be heated more uniformly with longer wavelength lasers, whereas thinner films require shorter wavelengths to reduce the energy absorbed by the substrate due to the stronger absorption by the silicon.

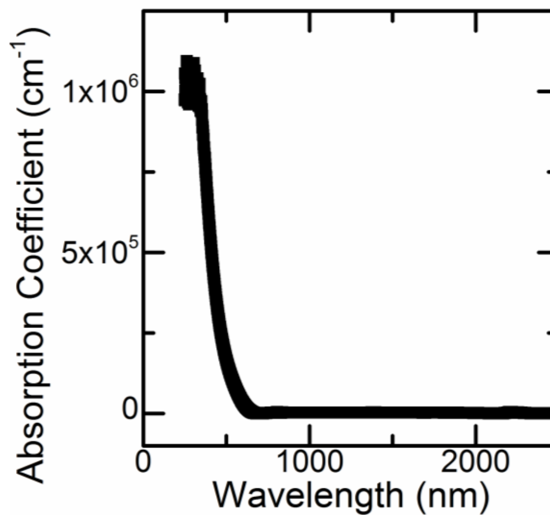

Figure 24. The measured absorption coefficient of amorphous silicon increases dramatically for wavelengths shorter than 600 nm.

The absorption coefficient also strongly depends on temperature. Jellison and Modine[74] examined the temperature dependence of crystalline silicon optical properties and showed the absorption coefficient is empirically related to temperature as

$$\alpha(\lambda, T) = \alpha_o(\lambda)e^{\frac{T}{T_o}} \quad (4.2)$$

where T_o is a fitting parameter determined to be 430 °C for all wavelengths. The exponential increase in absorption with regard to temperature makes the use of lasers at higher wavelengths viable for laser crystallization. The shallow penetration depth (

Table 2) of the laser energy expands the number of possible substrates to those with low melting temperatures, such as glass and plastics, a key advantage of laser crystallization.

Table 2. Lasers commonly used for the laser-crystallization of silicon films.

Laser	Wavelength (nm)	Pulse Length (ns)	Penetration Depth (nm)
Q-switched Ruby Laser[75]	694	28	3307
$Nd:YAG/Nd:YVO_4$[76-78]	1064	7-25	3354
$Nd:YAG/Nd:YVO_4$ (frequency doubled)[20,32,76,77,79]	532	7-25	90
$Nd:YAG/Nd:YVO_4$ (frequency tripled)[76,77,80]	355	7-25	11
ND:YLF (frequency doubled, Q-switched)[81]	524	15-20	81
Ar^+ [82,83]	330	CW	10
ArF[84]	193	10-20	9
XeCl[31,85-87]	308	10-20	10
KrF[88-92]	248	10-20	10

Lasers used for laser crystallization with their corresponding wavelengths, typical pulse lengths, and penetration depths, determined from Figure 24.

The absorbed energy is converted to heat and diffuses through the film creating a deeper melt. Little energy is lost through convection and radiation from the surface due to the thinness of the film and the short pulse width. The heat transfer is dictated by the heat equation:

$$c_p(\boldsymbol{x},T)\rho(\boldsymbol{x},T)\frac{\partial T(\boldsymbol{x},t)}{\partial t} = \nabla[\kappa(\boldsymbol{x},T)\nabla T(\boldsymbol{x},t)] + S(\boldsymbol{x},t) \tag{4.3}$$

where c_p and κ are the temperature-dependent specific heat at constant pressure and thermal conductivity, ρ is the density, and $S(x,t)$ is the source term.

The heat diffuses through the film until it reaches the melting temperature (measured by Donovan *et al*[93] to be 1420 K) at which point the a-Si melts. The depth and duration of the melt cycle is strongly dependent on the fluence of the laser, which is the pulse energy divided by the area of the beam. A threshold fluence is required to melt the surface of the silicon film. As the laser fluence is increased, a larger amount of energy is absorbed and more heat diffuses through the sample, increasing the melt depth. At a critical fluence, the entire film melts, and higher fluences merely heat the liquid silicon further, increasing the melt duration of the film.

The extremely short timescales in which the energy is absorbed by the silicon results in a steep temperature gradient, causing the silicon to cool quickly. Hatano *et al*[88] exploited the difference in optical properties between liquid and crystalline silicon to measure the *in situ* melt duration. Silicon films were crystallized with a KrF excimer laser (248 nm, 25 ns) at fluences of 262 and 365 mJ/cm^2. The surface melted within 10 ns for both fluences and remained in the molten state for 50 and 80 ns and began to cool. The surface cooled at a rate greater than 10^{10} K/s. The extreme cooling rate is believed to be the basis for ion implantation[10], which is capable of dopant densities much higher than solubility limits allow. The quenching of the film locks the dopants in the lattice, preventing phase separation.

Transient temperatures of the films were also measured by Hanato *et al*[88]. The surface just reaches the melting temperature for a fluence of 225 mJ/cm^2 but quickly cools. At higher fluences, the temperature exceeds the melting temperature and as it cools, and the temperature

profile begins to oscillate due the release of the latent heat during crystallization. The melt duration is shown to be less than 100 ns for fluences below 389 mJ/cm^2.

The latent heat released during the crystallization of silicon significantly affects the surface temperature.[88] The extreme amount of energy released during crystallization can cause a chain reaction, in which a melt front is propagated throughout the film. This phenomenon is called explosive crystallization[75] and was observed by measuring the transient electrical conductance and surface reflectivity. An initial peak in conductance, due to the higher conductivity of liquid silicon, was observed simultaneously with an increase in reflectivity. However, a second peak in conductivity was observed after the surface melt. The reflectivity probed the top 20 nm of the film, so the second melt occurred within the film. Thompson *et al* suggest that at low crystallization fluences, a thin layer on the surface is melted, and as it re-crystallizes, the latent heat released melts the underlying amorphous silicon, and the process repeats until the entire film is crystallized. The crystallite diameter produced during explosive crystallization is much finer than that produced by the melt from the laser. The different grain sizes suggest that two different nucleation phenomena are present during crystallization.

Thermal nucleation occurs when nuclei reach a critical size. As the film temperature approaches the melting temperature, regions of the material fluctuate between solid and liquid states. Particles smaller than a critical size, called embryos, must overcome an activation energy to reach the critical size and become a nucleation site. As the temperature cools, the Gibbs free energy becomes large enough to reach the activation energy. Phase transitions with gradual cooling rates are driven by thermal nucleation. The relationship between the change in Gibbs free energy and the change in temperature for thermal nucleation is given by[94]

$$\Delta G(r) = -\frac{4}{3}\pi r^3 \frac{\Delta H_m}{T_m}\Delta T + 4\pi r^2 \gamma_{sl} \quad (4.4)$$

where r is the radius of the nucleus, ΔH_m is the latent energy released upon crystallization, γ_{sl} is the interfacial energy between the solid and liquid phases, and T_m and ΔT are the melting temperature and change in temperature, respectively. The change in Gibbs free energy is a maximum at

$$r_{critical} = \frac{2\gamma_{sl}T_m}{\Delta H_m \Delta T}. \quad (4.5)$$

The Gibbs free energy at the critical radius is the activation needed for the nucleus to grow into a crystal. The activation energy is given by:

$$\Delta G_{activation} = -\frac{16\pi}{3}\gamma_{sl}^3 \left(\frac{T_m}{\Delta H_m}\right)^2 \frac{1}{\Delta T^2}. \quad (4.4)$$

The probability of an embryo nucleating is then proportional to $\exp(\Delta G_{activation}/k_b T)$.

Thermal nucleation occurs for relatively gradual changes in temperature. For systems undergoing extreme cooling, phase transitions are driven by athermal nucleation. Athermal nucleation occurs when the free energy barrier is reduced below the energy present in the embryo.[95] In other words, instead of embryos becoming nuclei by expanding to a critical radius, as in thermal nucleation, the temperature-dependent critical radius becomes smaller than the size of the embryos.

Nucleation rates depend on both thermal and athermal nucleation, where the emphasis depends on the cooling rate and the temperature of the sample.[96] Im *et al* derived a diagram showing three regimes in which the nucleation phenomena in liquid silicon are thermal-dominated, athermal-dominated, and a combination of the two. When the entire film is fully melted, it undergoes a phase transition dominated by athermal nucleation, resulting in the formation of small crystallites. Partially melted silicon films undergo a phase transition

dominated by thermal nucleation. Hatano *et al*[88] observed small crystallite diameters for both low and high fluences, suggesting the ideal nucleation mechanism for large grain growth involves both thermal and athermal nucleation.

6.2. Crystallization Parameters and Film Properties

The structure and properties of laser-crystallized silicon films vary widely for the different crystallization parameters. As mentioned earlier, the laser fluence plays a key role in the crystallization process. However, different fluences produce different results from laser to laser depending on the operating wavelength, beam shape and intensity profile, as well as the crystallization technique itself. Environmental factors also impact the crystallization process. Temperature and atmospheric composition have been studied, as well as the type of substrate, its structure, and the film parameters, such as film thickness and hydrogen content.

6.2.1. Crystallization Fluence

The crystallization fluence is paramount with regard to the crystallization parameters. The melt depth, determined by the fluence, determines the crystallinity of the film. Partially crystallized films have lower conductivities compared to fully crystallized films. The crystallinity is typically determined by Raman spectroscopy, but can be measured using TEM.

As mentioned in Chapter 2.2.5, Raman spectroscopy can be used to identify materials by vibrational modes unique to different materials. Crystalline silicon is a highly ordered lattice with uniform bond angles, lengths, and energies, which result in a narrow range of vibrational modes and, consequently, a narrow Raman peak with a Raman shift at 521 cm^{-1}. Amorphous silicon, conversely, is a disordered material with wide-ranging bond angles, energies, and lengths, resulting in a broad range of lattice vibrations, and thus has a broad Raman peak with a Raman shift located at 480 cm^{-1}.

A Voigt profile is typically fit to the crystalline mode, and a Gaussian profile is fit to the amorphous mode. The crystalline fraction can then be calculated using the intensities of the two fits using the relation:

$$\chi = \frac{I_c}{I_c + \gamma I_a} \tag{4.5}$$

where I_c and I_a are the integrated crystalline and amorphous intensities obtained from the fits and γ is a fitting factor that has been determined to be between 0.8 and 0.9.[97] Adikaari *et al*[98] demonstrated that the crystallinity strongly depends on the crystallization fluence. Film morphology is also affected by the fluence, as discussed in greater detail in later subsections.

6.2.2. Crystallization Techniques and Beam Profiles

Large crystal grains are the main goal when laser-crystallizing films for their superior electronic properties compared to those of poly-crystalline silicon. Several crystallization techniques have been developed to maximize the crystal length formed in silicon films. Im *et al*[85,86] noted the formation of large grains formed, called super lateral growth, for specific laser fluences using a XeCl excimer laser (308 nm, 30 ns). The samples consisted of non-hydrogentated, 100 nm thick, low-pressure CVD amorphous silicon films. Super lateral growth was coupled with a scanning technique coined sequential lateral solidification (SLS) to produce directionally solidified grains of unrestricted length.[31,32,99] The process uses a rectangular beam that fully melts a region of the silicon. The sample is translated by 0.75 μm and new region is completely melted. The crystals along the solid-liquid interface act as nucleation seeds, leading to further crystal growth. Initially, many crystals are present, but after several consecutive pulses, adjacent crystals occlude one another and only the long crystals persist. Shorter translations result in a higher pulse density, which results in rougher films.[77,90]

Several beam shapes were experimented with to further enhance the SLS technique. Im *et al*[87] used a chevron shaped mask to enhance the width of the crystals. Lee *et al* [91] examined the effects of creating a linear gradient in the intensity, in which the least intense portion of the beam is adjacent to the previously crystallized region. The silicon melted by the lower intensities crystallizes faster than the hotter part of the beam, effectively reducing the probability of spontaneous nucleation before lateral growth occurs. The beam with the linear gradient was capable of producing crystals 3x longer.

Many other combinations of intensity profiles and beam shapes have been examined, including a doughnut-intensity profile using an Ar^+ CW laser,[83] However, the flat-top and Gaussian intensity profiles are most popular since they are the output for excimer and solid state lasers, respectively. Gaussian beams suffer from a lack of uniform crystallinity. The fluence is limited by the maximum intensity at the center of the beam, which must be lower than the ablation threshold. The advantage of a Gaussian beam, however, is that the hydrogen in the film does not need to be removed prior to laser-crystallization, as the lower intensities on the edge of the Gaussian beam slowly heat the film, causing the hydrogen to gently diffuse out. McCulloch and Brotherton[90] converted the top-hat profile of a KrF laser (248 nm) into a semi-Gaussian intensity profile with a 6.6 mm FWHM and crystallized a film without an initial annealing step to remove the hydrogen. The film, however, was significantly rougher than similar films crystallized with the same parameters by other authors[88,92] and appears to show significant signs of agglomeration.[80,90,100] The roughness and agglomeration increased with increasing pulse densities.

6.2.3. Type of Laser and Wavelength

Excimer lasers were initially used to crystallize silicon because of the high absorption in the UV. Solid-state lasers at the time were unable to operate at high powers in the UV, but as the technology developed, solid state lasers were soon preferred for laser crystallization because of their high processing speeds. Most studies have been done using the first (1064 nm) [76,77] and second (532 nm) harmonic,[20,32,76,77,79] and more recently the 3rd harmonic (355 nm).[76,80] Since silicon absorbs weakly at 1064 nm, the laser penetrates deeper into the sample and the substrate. The bulk of the energy is absorbed by the surface of the substrate, which heats the amorphous silicon from the bottom. The process results in disruptive melting, which causes material to be ejected from the sample.[78]

Dassow *et al* were the first to apply the sequential later solidification technique to solid state lasers.[20] They observed long grains by crystallizing silicon films with an elliptical Nd:YVO_4 laser operating at the second harmonic (532 nm) with a pulse separation distance of 0.5 μm. Other studies, however, were unable to create the long grains using 532 nm pulsed lasers, but instead created rough samples.[76-78]

Few studies have been done to study the effects of crystallizing films with 355 nm pulsed lasers. Based on a literature review, long grains have not been produced using 355 nm lasers to crystallize silicon films. Chunyan *et al*[80] produced polysilicon with average grain diameters near 100 nm.

More recently, femtosecond lasers have been applied to laser crystallization. Excimer and solid state lasers have comparable pulsewidths, however femtosecond lasers have pulsewidths two orders of magnitude shorter. The short pulsewidths result in nonlinear absorption by the films and enhance the roughness of the crystallized film.[101]

6.2.4. Crystallization Environment and Sample Preparation

Environmental factors also play a role in the crystallization process. Substrate temperature, for example, has been shown to affect the grain size. Samples heated to 550 °C during laser processing had an average grain radius double that of the sample kept at ambient temperature at a lower fluence.[85] Ming *et al*[102] observed a similar effect. The difference is attributed to the different nucleation process. The higher temperature of the sample reduces the quench rate, and thus the nucleation phenomenon.

Brotherton and McColloch[89,90] studied laser-crystallized films in ambient air, nitrogen, argon, and vacuum, and they used reflectance measurements to indirectly determine the roughness of the films. They found samples crystallized in air had significantly rougher profiles at lower fluences than those crystallized in nitrogen or argon. The samples crystallized in ambient air, however, had higher electron mobility than those crystallized under inert conditions. Since the samples were etched after being crystallized, the improved mobilities were not due to the passivating oxide that formed. Brotherton *et al* hypothesize that oxygen passivated the dangling bonds at grain boundaries. Marmorstein *et al*[103] observed similar effects with different atmospheric composition, and the maximum average grain size was affected by the composition of the atmosphere.

The amorphous silicon film composition and preparation primarily affect the structure of the silicon films. Mathe *et al* [84] showed that films containing 10 % – 20 % hydrogen produce rougher films compared to those without hydrogen. When the film melts during irradiation, the hydrogen turbulently diffuses out of the film, creating a rough film when it re-crystallizes. The threshold crystallization fluence was not affected by the presence of the hydrogen; however, the size of the crystals were smaller in the hydrogenated sample. Film roughness can be reduced by

capping the film with a laser-transparent oxide layer. During the crystallization process, the film is confined to the area under which it is covered, preventing the film from roughening, but also increasing the tensile stress in the film. The enhanced stress inhibits crystallization due to an increase in the free energy barrier between amorphous and crystalline silicon that arises from a higher Young's modulus in crystalline silicon compared to amorphous silicon[104].

Film thickness affects the roughness of the film as well, which is likely simply due to the availability of more material that can be used to form the peaks. Adikaari and Silva[98] used AFM to determine the root mean square roughness of 100, 300, and 500 nm thick films. Film thickness also affects the critical fluence for the sample, as more energy is needed to fully melt the film.

The dopant density and substrate composition have been shown to affect the tensile stress in films crystallized with a XeCl excimer laser.[105] Lengsfeld *et al*[105] used contact profilometry and Raman spectroscopy to measure the stress in the films. The profiler measurements revealed a curvature in the crystallized films with a maximum deflection of 6 μm over the span of 4 cm. The curvature was fit to the profile data and Stoney's equation[106] was used to determine the tensile stress. The profiler calculations corroborated the Raman measurements, which showed that films crystallized with the same fluence on different substrates have different tensile stresses. Raman spectroscopy probes the vibrational states. When the film is stressed, more energy is required to vibrate the atoms, reducing the energy of the scattered photon which results in a Raman shift at a smaller wavenumber. Lengsfeld *et al* and others suggest the stress arises from a difference in thermal expansion coefficients between the film and the substrate. The stress is reduced at higher fluences for certain substrates, which is likely due to the temperature of the substrate exceeding its softening limit. The internal stress increases with doping levels and is due to the occupation of lattice sites by non-silicon atoms, typically boron or phosphorous.

7. PROPERTIES OF 355 NM LASER-CRYSTALLIZED SILICON

Extensive research on the laser-crystallization of amorphous silicon has been done with excimer lasers operating at ultraviolet wavelengths, and more recently with pulsed solid-state lasers at 1064 and 532 nm; however, little research has been done with solid-state lasers operating at the tripled frequency at 355 nm. The focus of the studies on laser crystallization of amorphous silicon (a-Si) films presented in this chapter is on the impact of different crystallization fluences used to crystallize films of different thicknesses and substrate compositions. Consistent trends were observed for films crystallized with different laser fluences, and both the film thickness and substrate composition significantly affected the morphology and electronic properties of the crystallized film.

7.1. Morphology Dependence on Film Thickness

Optical and scanning electron micrographs suggest rougher surfaces were produced as the laser fluence was increased, with porous films forming as the fluence was increased still further. At the maximum laser fluence for the thinnest a-Si films, complete agglomeration of the film into isolated pillars occurred, as shown in Figure 25. As the thicker films were crystallized at the maximum fluence, the film became less agglomerated.

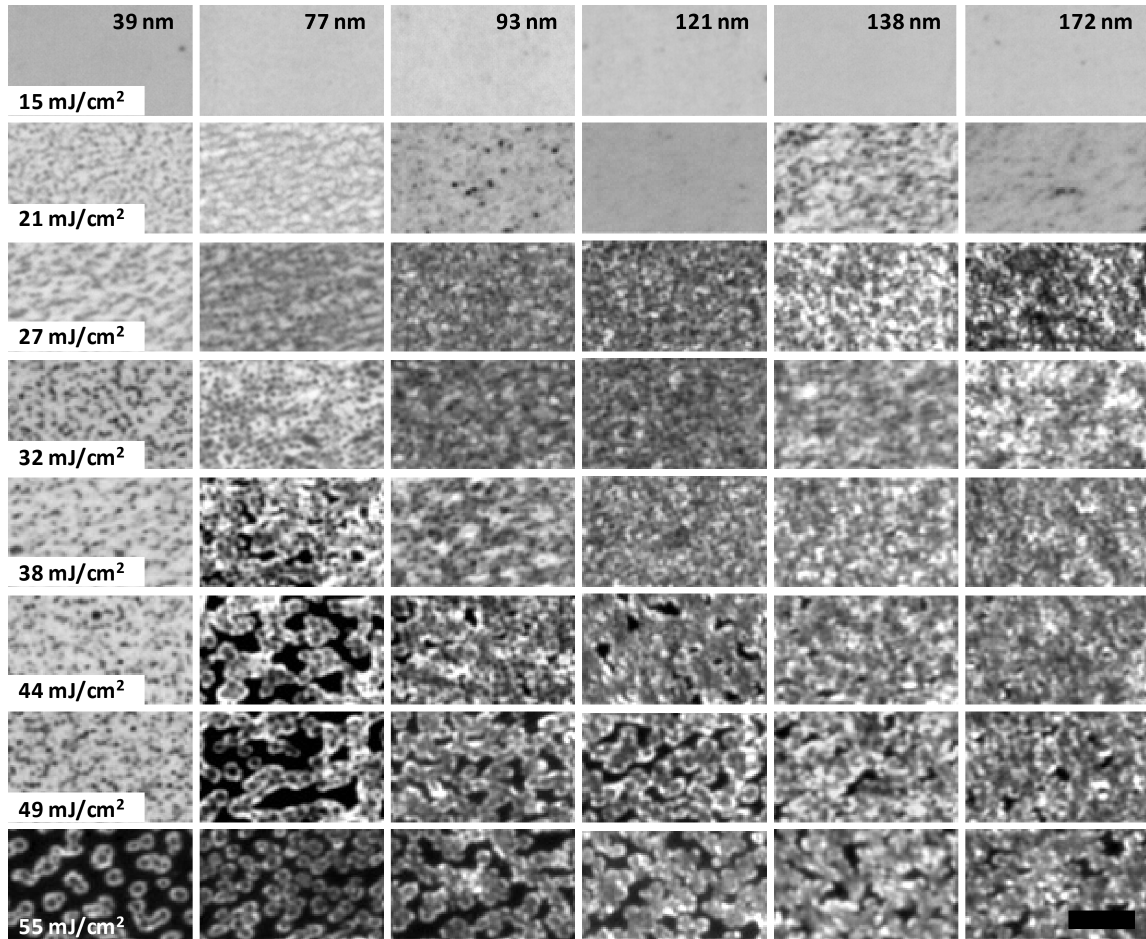

Figure 25. Optical micrographs of various intrinsic film thicknesses laser-crystallized with different fluences.[107] The scale bar is 5 μm.

Greater morphological detail can be seen in the SEM images of doped films shown in Figure 26. For the thinnest film (41 nm), no obvious change in the morphology occurred from 44 to 55 mJ/cm^2, but the insets of these images show a change in the surface on which the pillars appear. Higher magnification SEM images of the surface generated at 44 and 55 mJ/cm^2 laser fluences had a similar morphology to that of the SiO_2 substrate surface, suggesting that the amorphous silicon film had completely localized and agglomerated. The morphology of the 126 nm thick films, in contrast, transitions more continuously with increasing laser fluence. As the fluence is increased, pillar growth and consolidation occur but the morphology does not become fully discontinuous due to the larger thickness of the films.

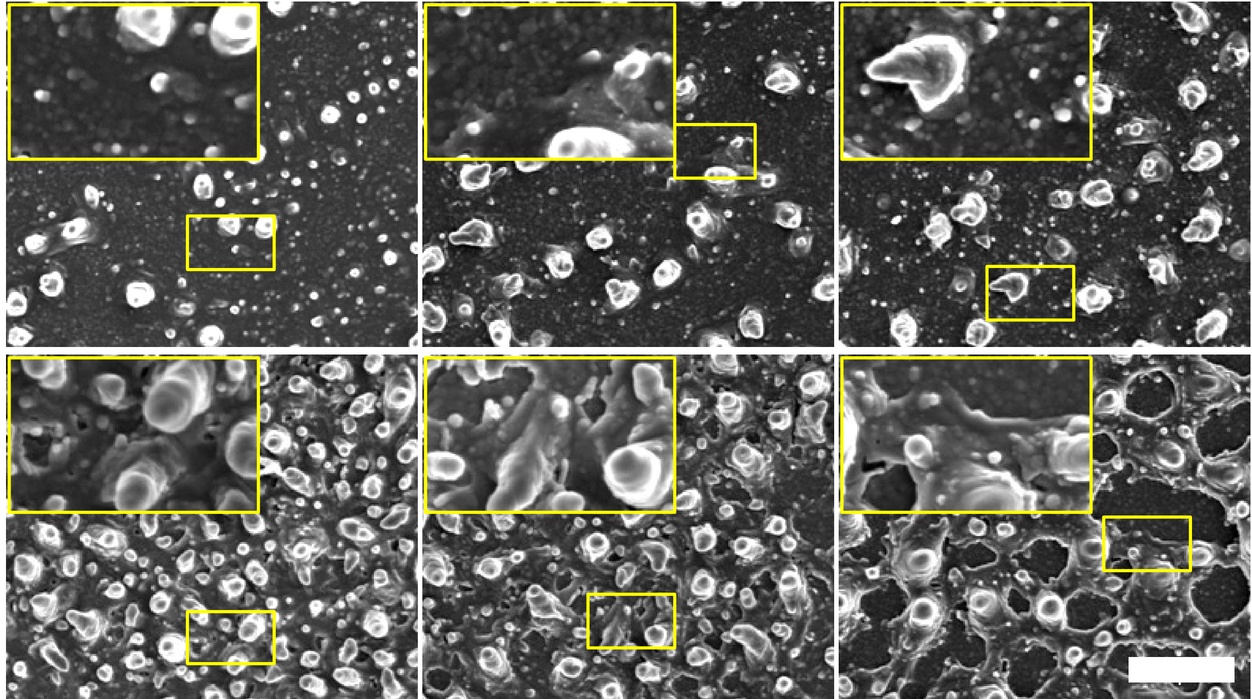

Figure 26. High-resolution SEM images of laser-crystallized doped (n-type) films.[107] Film thicknesses are 41 nm (top) and 125 nm (bottom), and the samples were crystallized with fluences of 38, 44, and 55 mJ/cm^2 (left to right). The scale bar is 2 μm, and the rectangular insets are 1.6 μm wide.

For a silicon film of specified thickness, there is a critical laser fluence required to fully crystallize the film. A fluence below this threshold leads to a stratified film composed of mixed phases of a-Si adjacent to the substrate and c-Si near the surface. The degree of crystallinity can be determined using Raman spectroscopy. If a suitable excitation wavelength is chosen (e.g., 532 nm where the optical extinction length of c-Si is around 1 μm), an analysis over the entire film thickness can be achieved. The Raman spectrum of a mixed-phase silicon film is composed of a broad a-Si mode at 480 cm^{-1} and a narrow c-Si mode at 521 cm^{-1}, as shown in Figure 27a for 15 mJ/cm^2. Stressed films[105] and films composed of μ- and poly-Si[108] have a broadened c-Si mode that is shifted to lower wave number. Local stresses in the film can arise from a mismatch in the thermal expansion coefficients of the silicon and substrate.

Raman spectra were normalized such that the c-Si TO peak reached unity and Gaussian line-shapes were fit to the data. The FWHM and Raman shift were measured and are plotted in Figure 27(b) and (c), respectively. As expected, increasing the laser pulse energy and decreasing the film thickness both reduce the FWHM and increase the Raman shift.

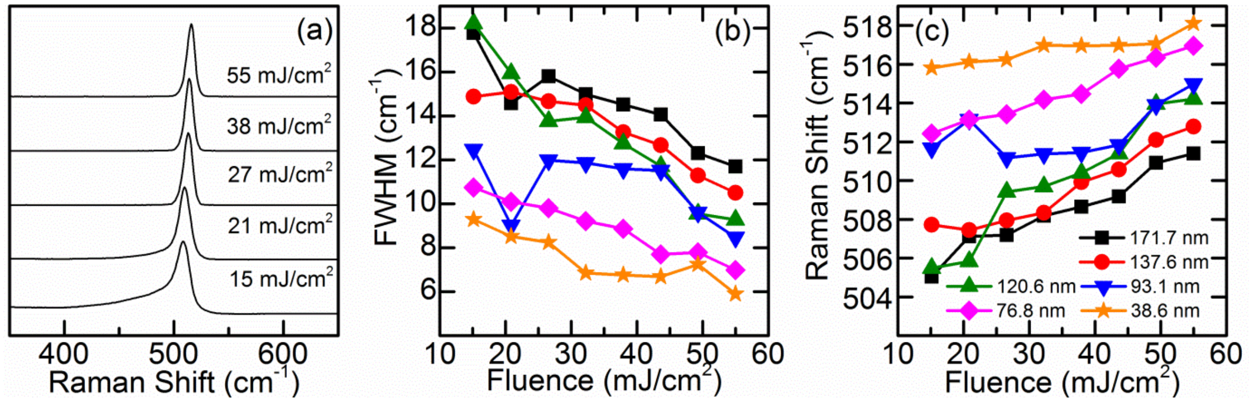

Figure 27. (a) Raman spectra of 121nm thick laser-crystallized intrinsic silicon films. The FWHM (b) and Raman shift (c) of the crystalline TO peak for several film thicknesses crystallized at varied laser pulse energies as indicated in the legend.[107]

XRD spectra were obtained from 121 nm thick intrinsic films to determine the influence of laser fluence on structure and crystallite size. After laser annealing, three shallow broad peaks were observed at $2\theta = 28.4°$, 47.3°, and 56.1°, as shown in Figure 28a. The diffraction peaks were indexed based on JCPDS card number: 27-1402 and correspond to the $\langle 111 \rangle$, $\langle 220 \rangle$, and $\langle 311 \rangle$ orientations. The $\langle 111 \rangle$ peak was used to calculate crystallite size based on the Scherrer equation:

$$D \approx \frac{0.9\lambda}{\beta \cos\theta} \tag{5.1}$$

where β is the FWHM, θ is the diffraction angle, and λ is the wavelength.[109] An initial decrease in the FWHM from 21 mJ/cm^2 to 32 mJ/cm^2 implies the transformation of a-Si into nanocrystalline Si. A minimum FWHM of 0.38° at 44 mJ/cm^2 corresponds to an approximate mean crystallite diameter of 43 nm. The Si $\langle 111 \rangle$ peak position of samples annealed at fluences

greater than 32 mJ/cm^2 showed no significant shift in comparison to the bulk (JCPDF 27-1402). However, films crystallized with fluences less than 38 mJ/cm^2 showed enhanced line-width and hence smaller crystallite size.

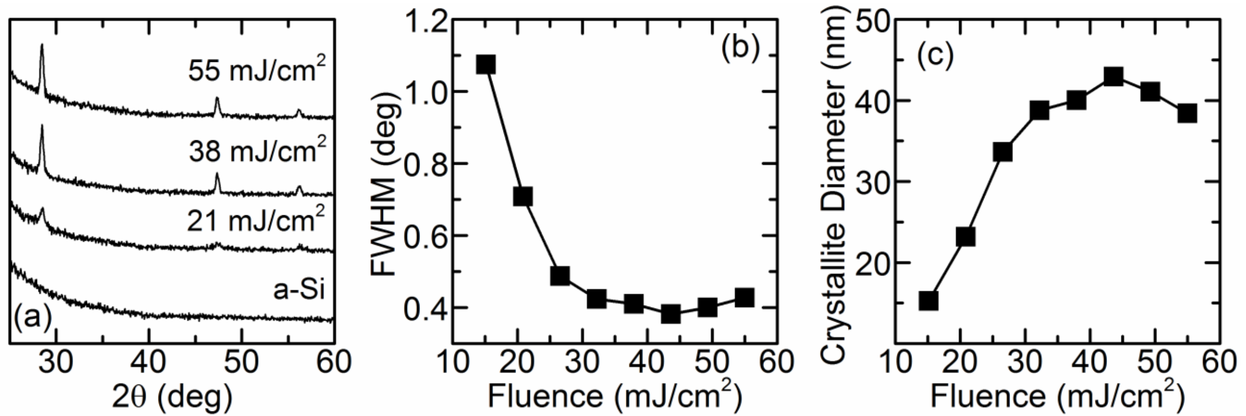

Figure 28. (a) XRD spectra of 121 nm thick intrinsic Si films in descending order of laser fluence; 26.6, 18.4, and 10.1 mJ/cm^2. The bottom reference spectrum is for a-Si. (b) The FWHM of the (111) peak for a 121 nm thick silicon film vs. laser fluence. (c) Mean crystallite diameter as a function of laser fluence.[107]

The resistivity of the doped films was measured with the probes aligned both parallel and perpendicular to the laser scanning direction. No anisotropy was detectable, consistent with isotropic structure. The average resistivity is plotted as a function of laser fluence in Figure 29(a). The resistivity of each film exhibits a minimum around 32–38 mJ/cm^2, where energy densities greater than this lead to agglomeration and a subsequent increase in resistivity due to a loss of connectivity percolation in the films. An exception to this general rule is the 126 nm film, which remained reasonably conductive over all laser fluences due to incomplete agglomeration. As the film thickness decreased, however, the non-conducting fluence threshold also decreased. At the lowest energy densities, the average film resistivity decreased in response to a corresponding decrease in film thickness, suggesting that there is a more complete crystallization occurring in the thinner films. We note that this trend is consistent with the Raman spectra of the intrinsic films shown in Figure 27(c). The absorption coefficient of a 121 nm thick film was

determined by measuring both the transmittance and reflectance spectra as a function of laser fluence. The transmittance and reflectance measurements were averaged over the visible spectrum and are plotted in Figure 29(b). Both the reflectance and transmittance decrease abruptly at 21 mJ/cm^2, while the transmittance increases above a fluence of 38 mJ/cm^2 due to the onset of agglomeration in the films. For uniform amorphous thin films, the optical band gap can often be obtained from a Tauc plot of $(\alpha h\nu)^r$ vs. $h\nu$, where α is the absorption coefficient, $h\nu$ is the photon energy, and r is determined by the type of transition. Direct band-gap materials, such as a-Si, are typically characterized by $r = 0.5$.[110] We can obtain an optical band gap for the 121 nm film at low laser fluence by fitting a line through the linear region of the Tauc plot and identifying the energy where this line intercepts the horizontal axis, as shown in Figure 29(c). For energy densities up to 21 mJ/cm^2, such data suggest a band gap that is close to the accepted value for a-Si [inset, Figure 29(c)]. Above this laser fluence, however, such plots do not yield physical information. This is consistent with trends reported in the literature, where such an analysis has been found to be inapplicable to crystalline or multiphase films.[110] This is also evident for the highest fluence in Figure 29(c) (21 mJ/cm^2), where the linear regime is already starting to exhibit the onset of significant curvature.

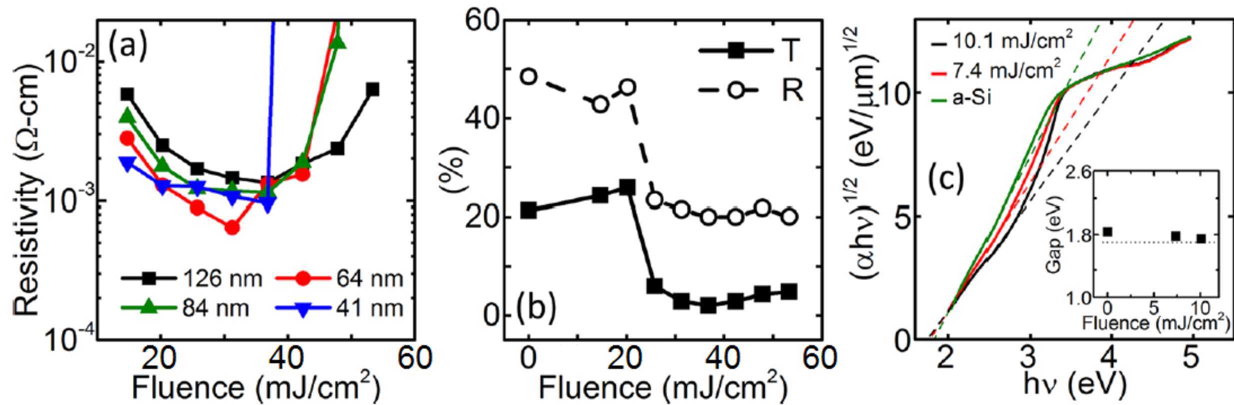

Figure 29. (a) Resistivity of the phosphorous-doped, laser-crystallized films. (b) Average visible transmittance and reflectance of 121 nm thick intrinsic, laser-processed films. (c) Tauc plot for the 121 nm thick intrinsic film at low laser fluence, where the inset shows the optical band gap determined from such plots along with the accepted value (dashed line) for a-Si (1.7 eV).[107,111,112]

The phase diagrams in Figure 30 succinctly show the dependence of the surface morphology and Raman shift on film thickness and laser fluence. Here, the morphology and Raman shift were determined *via* optical microscopy and Raman spectroscopy, respectively, for intrinsic silicon films. Although surface morphology and Raman shift both depend on film thickness and energy per unit area, the Raman shift is more responsive to the former and the morphology is more responsive to the latter. The phase diagrams can be used to guide the production of samples with a specific morphology and structure by choosing an appropriate thickness and laser fluence. Based on microscopy, intrinsic and doped films display the same morphologies at fixed laser energy densities. The Raman shift, however, has been shown to strongly depend on the doping level because of interactions between free carriers and the optical phonons. This interaction can cause an up or down shift in the TO phonon mode for p or n doped samples, respectively, as well as a change in the lineshape of the TO peak.[113]

Figure 30 suggests that there are two “orthogonal” effects governing the interplay of film thickness and laser fluence. The simplest effect [Figure 30(b)] is the tendency for thinner films to more readily crystallize. Physically, thicker films melt and crystallize at the surface, leaving an

underlying layer of amorphous material. The second effect [Figure 30(a)] is more complex. At fixed film thickness, increasing the fluence will more readily melt the material and reduce its viscosity. Interfacial tension will then cause the molten Si to form droplets on the SiO_2 substrate, which can render the crystallized film in a non-percolated morphology depending on film thickness. These two competing effects underlie the resistivity data in Figure 29(a). At lower fluence, resistivity increases with increasing film thickness (the first effect), while each trace in Figure 29(a) shows a loss of conductivity associated with agglomeration (the second effect).

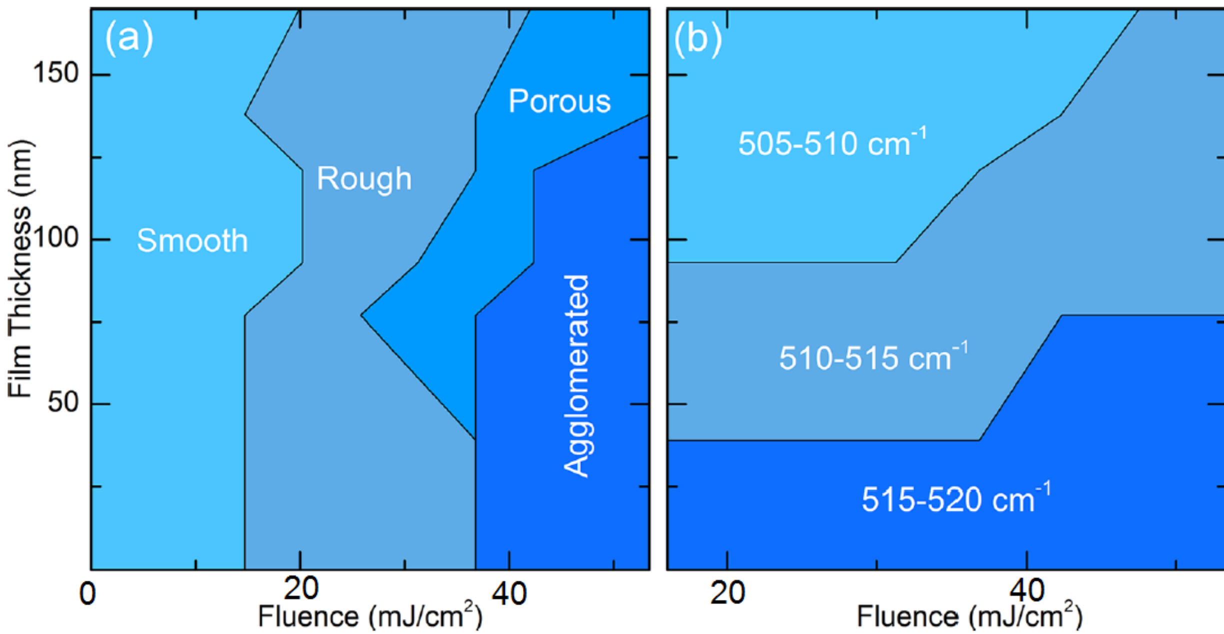

Figure 30. Phase diagrams for (a) the film morphology and (b) the Raman shift of the intrinsic laser processed films.[107]

As shown in Figure 31, we can use simple scaling arguments to model this behavior. Normalizing the resistivity by a characteristic value ρ_o collapses the vertical axis of Figure 29(a), while normalizing the fluence by a characteristic value H_o collapses the horizontal axis, where H_o represents the critical fluence for agglomeration. The choice of ρ_o is somewhat arbitrary and we choose it to coincide with thicker films at lower fluence. Choosing a different point, such as the onset of agglomeration, would shift the magnitude of ρ_o but the dependence on thickness

would be the same. The thickness dependence of the characteristic conductivity ($\sigma_o = 1/\rho_o$) mirrors that of the Raman shift, since the evolution from amorphous to crystalline will improve the charge transport characteristics of the films. Similarly, the critical fluence H_o mirrors the phase behavior in Figure 30(a). Below H_o [Figure 30(a)], the resistivity decreases with increasing fluence because of an increase in crystallinity, where the curve for $H < H_o$ in Figure 31(a) scales as fluence to the -4 power.

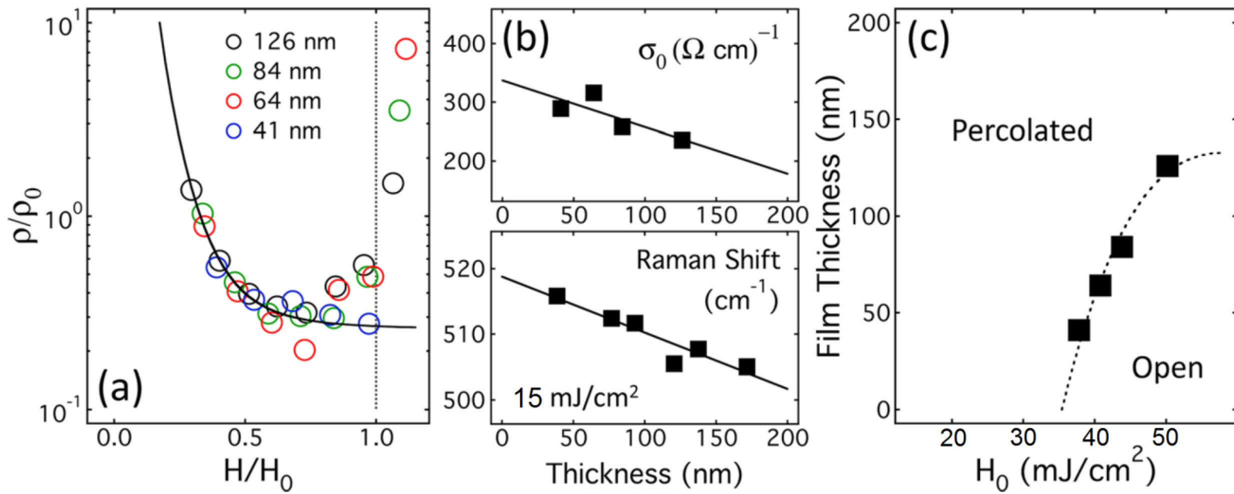

Figure 31. (a) Dimensionless scaling plot of the data in Figure 29. (b) Thickness dependence of the scaling parameter for the resistivity with a linear fit (upper, expressed as conductivity), which mirrors the change in Raman shift associated with the loss of crystallinity at fixed fluence (lower). (c) Thickness dependence of the critical fluence where the resistivity diverges, which mirrors the onset of agglomeration in the phase diagram in Figure 30(a).[114]

Several characterization techniques have been applied to both intrinsic and doped silicon films of varied thicknesses that have been laser crystallized at different laser fluences at 355 nm. The fluence and film thickness both have a substantial impact on the morphology, the crystallinity, and the electronic and optical properties of the crystallized films. Several aspects of these measurements suggest an optimal, minimum fluence between 32 and 38 mJ/cm^2. At this fluence, the crystallite size is maximized. It is also in this fluence range that the films begin to form pillars and achieve a point of maximum percolation (the films should be fully percolated

until they begin to exhibit substantial agglomeration) and minimum film resistivity. Energy densities greater than 38 mJ/cm^2 do not affect the crystallite size or pillar diameters, although still greater energy densities cause the film to agglomerate to a higher degree, increasing the resistivity while adding to the height of the pillars.

Film thickness plays a substantial role in the surface morphology and crystallinity of the films. Thicker films maintain their structural integrity for larger fluences, but as seen in the Raman spectra, thicker films are less crystalline than thinner films, which have competing effects on the conductivity. We offer a simple scaling model to account for this behavior and illuminate the underlying physics. The fact that the data can be described by such a scaling argument implies that the observed trends with fluence and thickness are always similar, if not precisely identical. Regardless of the exact location of a sample in the fluence-thickness plane, increasing thickness will inhibit crystallization and hence reduce conductivity, while increasing fluence will promote crystallization and hence increase conductivity, as long as the sample is percolated. The observed dependencies of film characteristics on film thickness and laser fluence allow for selective processing of the electronic and morphological properties of the films for specific needs, such as large pillar growth to promote surface roughness and enhance the absorption of solar radiation in photovoltaic devices. The results could have important implications for nanofabrication, such as patterned pillar growth through nanoparticle seeding of the substrate. Finally, our results also offer new insight into the laser processing of silicon at the specific wavelength of 355 nm.

7.2. Morphology Dependence on Substrate Composition

The film morphology varies significantly with substrate and laser fluence. Optical micrographs of i-Si (top) and n-Si (bottom) films crystallized at 55 mJ/cm^2, shown in Figure 32,

reveal that films on BAS and quartz have increased agglomeration as compared to the YSZ- and c-Si-supported samples. Differences in morphology between the i-Si and n-Si films can be attributed to the different film thicknesses. Transmission images were taken by back-illuminating the sample to outline the porosity, where the exposed substrate appears white and the film black. The percentage of exposed substrate (porosity) was calculated from the transmission images shown in Figure 33b, and the results are detailed in the graph of Figure 33a. The film on BAS agglomerated the most (up to 50 %), while films on YSZ showed the least agglomeration. The film on the BAS substrate showed significantly different agglomeration at low laser fluences compared to high laser fluences. At low fluences, large holes appeared in the film, whereas at higher fluences, small pinholes appeared, which is similar to what was seen on quartz.

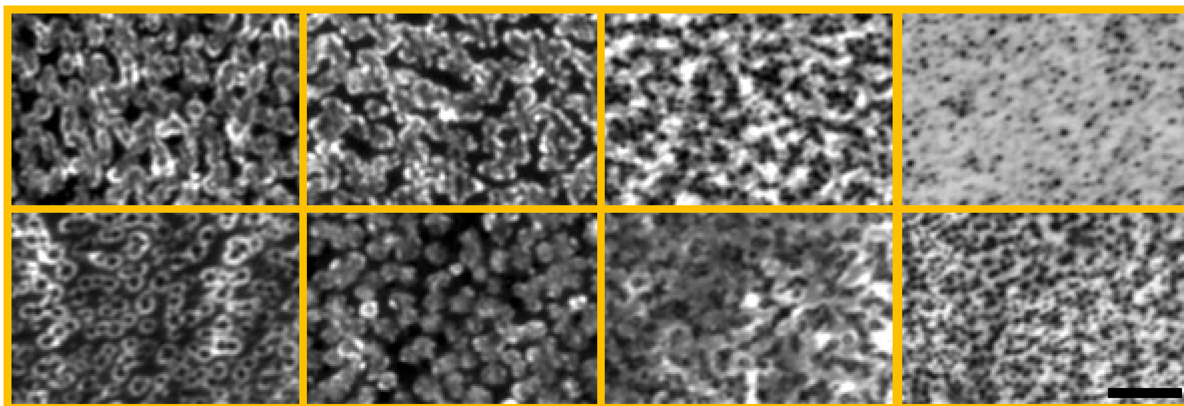

Figure 32. i-Si (top) and n-Si (bottom) films crystallized at 55 mJ/cm^2 on (left to right) quartz, BAS, YSZ, and c-Si substrates. The scale bar in the lower right image is 5 μm.[114]

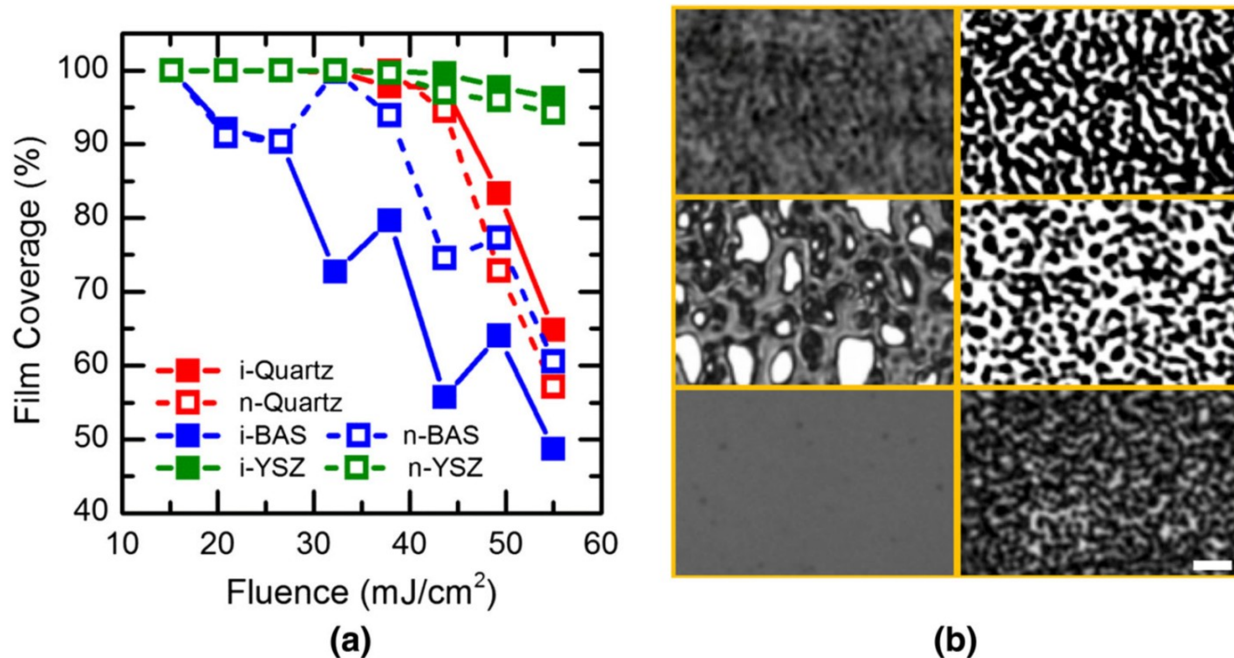

Figure 33. (a) The percentage of substrate covered by the film as a function of laser fluence. (b) Transmission images of i-Si on quartz, BAS, and YSZ (top to bottom) at 21 (left) and 27 mJ/cm^2 (right). White regions are areas of exposed substrate, and the dark circles are pillars that absorb more of the light. The scale bar in the lower right image is 5 μm.[114]

SEM images of the n-Si films (Figure 34) show that the films on quartz and BAS completely agglomerate in response to a laser fluence of 55 mJ/cm^2, whereas the YSZ and c-Si films at comparable fluence are still percolated, although both develop holes. Pillars grow regardless of substrate and show no preferred direction of growth. The pillars are less numerous and larger on the quartz and BAS substrates compared to the YSZ and c-Si samples. The tip-to-base length, FWHM, and tip-to-base angle were measured and are plotted as a histogram in Figure 35. On average, the pillars grow normal to the substrate with a deviation of approximately 15° for all four substrates. The pillars are approximately the same size on quartz and BAS substrates, but are narrower and shorter on the YSZ and c-Si substrates. AFM profiles were used to determine the average height and spatial density of the pillars as shown in Figure 36. The height follows an inverse relationship with the spatial density due to conservation of volume

within the film. The BAS and quartz substrates formed taller pillars compared to the YSZ and c-Si substrates, as evidenced by the SEM images.

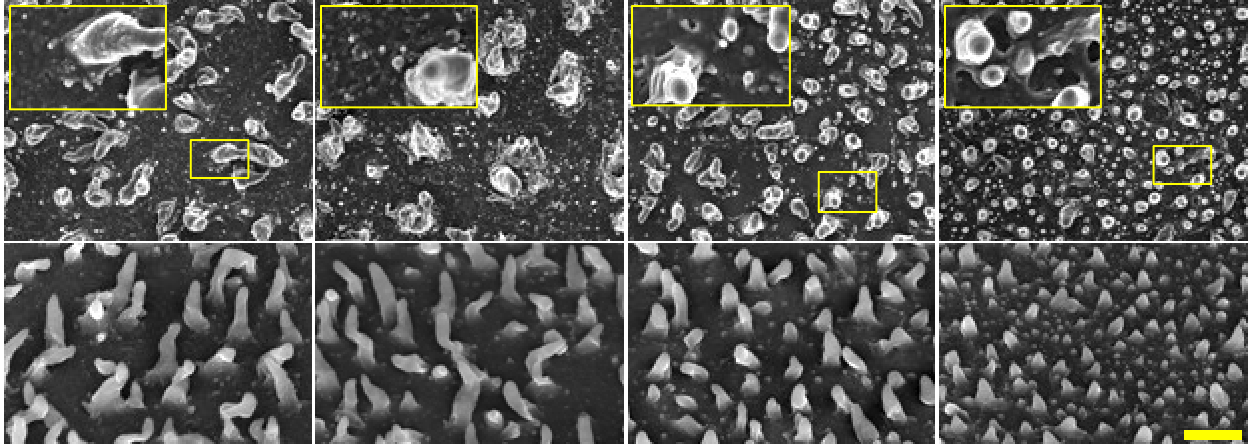

Figure 34. SEM images of n-Si films crystallized at a laser fluence of 55 mJ/cm^2 on quartz, BAS, YSZ, and c-Si substartes (left to right), as viewed normal (top) and tilted at 45° (bottom) to the sample. The scale bar and insets are 1.5 μm wide.[114]

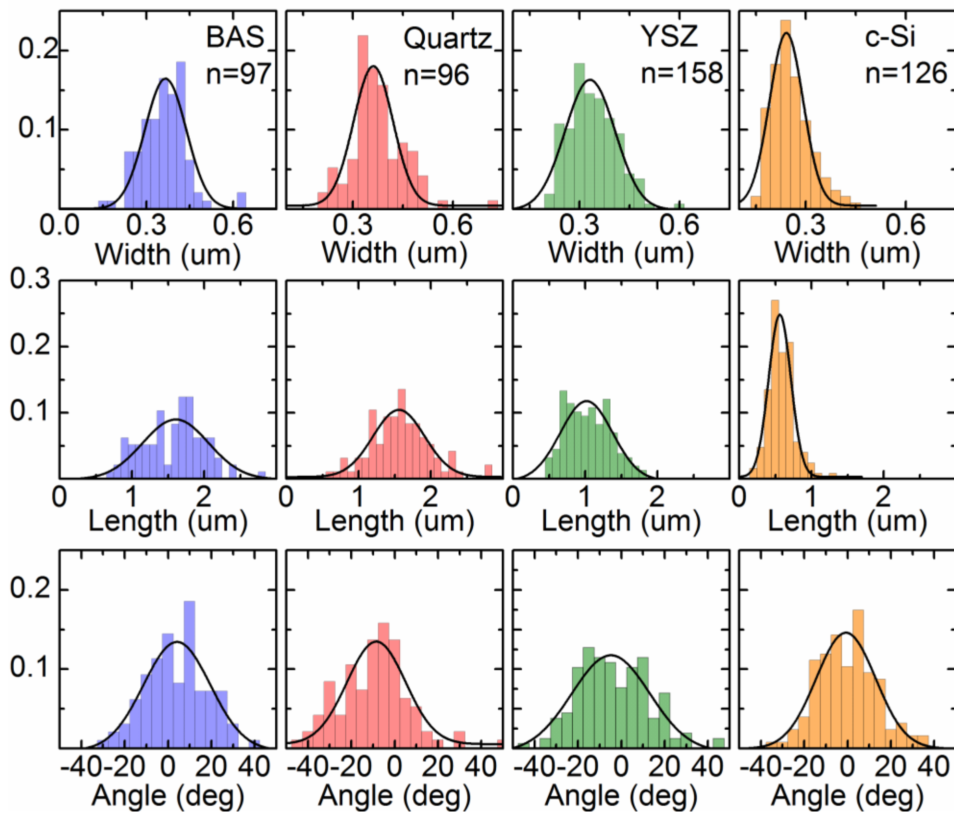

Figure 35. Normalized probability distributions of width (top), length (middle), and angle (bottom) for a-Si films crystallized at a laser fluence of 55 mJ/cm^2.[114]

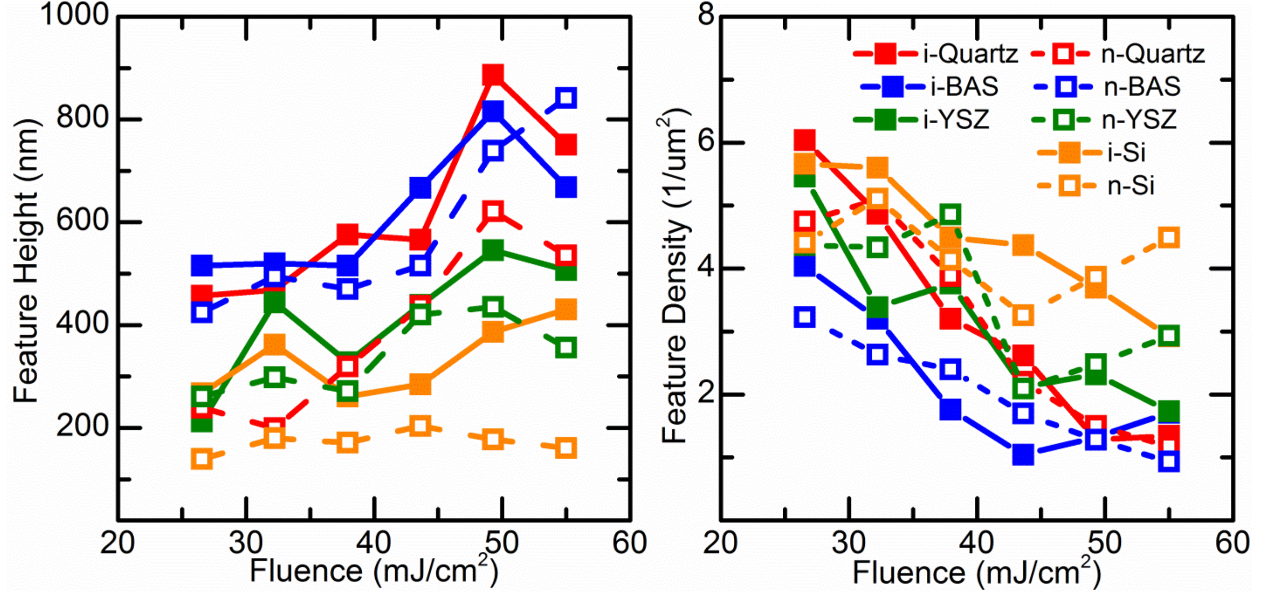

Figure 36. Feature height (left) and spatial density of features (right) plotted versus laser fluence for the n-Si and i-Si films on each of the four substrates.[114]

Raman spectroscopy of doped and intrinsic silicon showed similar trends with respect to the crystallization fluences as those shown in Figure 27. The Raman shift of doped films is typically larger than intrinsic films due to the extra stresses imparted by the dopant molecules[115]. Coherent coupling between discrete phonon states and the continuum of electronic states in n-type crystalline silicon leads to an asymmetric line shape through a Fano resonance.[115] The asymmetric Fano profile is given by:

$$\alpha(x) = a\frac{\left(q + \frac{2(x-p)}{w}\right)^2}{1 + \left(\frac{2(x-p)}{w}\right)^2} \tag{5.1}$$

where p is the location of the peak, w is the width, and the Fano parameter, q, dictates the peak asymmetry and in the present situation is an indicator of the level of n-type dopant in the film. This asymmetry can be seen in the n-Si spectrum at 55 mJ/cm^2 in Figure 37 (dashed curve), where the silicon film is fully crystallized. Asymmetry at lower fluence reflects a second amorphous peak at lower wave number.

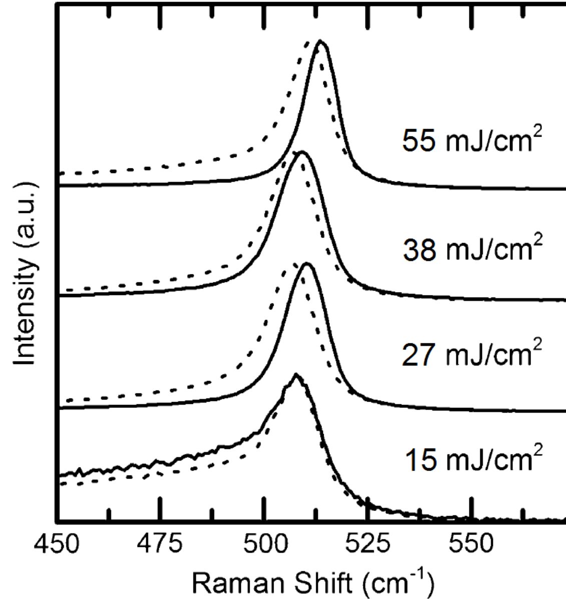

Figure 37. Raman spectra for i-Si (*solid*) and n-Si (*dashed*) crystallized on quartz with four different fluences. The amorphous contribution is evident at 15 mJ/cm^2, whereas the Fano effect is evident at 55 mJ/cm^2.[114]

The a-Si contribution to the spectra was fit with a Gaussian profile and removed as detailed elsewhere.[108] The c-Si mode was then fit using a Voigt or Fano profile for the intrinsic or doped samples, respectively. Figure 38 presents the results of the Raman analysis. Higher laser fluences increase the Raman shift and reduce the FWHM for both i-Si and n-Si. The doped samples consistently have a Raman shift to lower wave numbers due to higher stress in the film. The films are fully crystallized by 27 mJ/cm^2, which suggests that as the laser fluence increases beyond this point, a reduction in stress and a subsequent shift to higher wave numbers occur. The crystallinity was determined by taking the ratio of the integrated intensity of the crystalline peak to that of the amorphous peak, where a correction factor of 0.8 was used as detailed by Smit *et al.*[108]. The crystallinity does not depend on substrate, but the peak shift due to stress in the sample is lowest for the YSZ. The q-parameter for the n-Si films decreases with laser fluence up to 27 mJ/cm^2, at which point it remains constant due to crystallization and the dopant being fully

activated. The Fano asymmetry also depends on substrate, mirroring the Raman shift, which suggests that the electron-phonon coupling changes with stress.

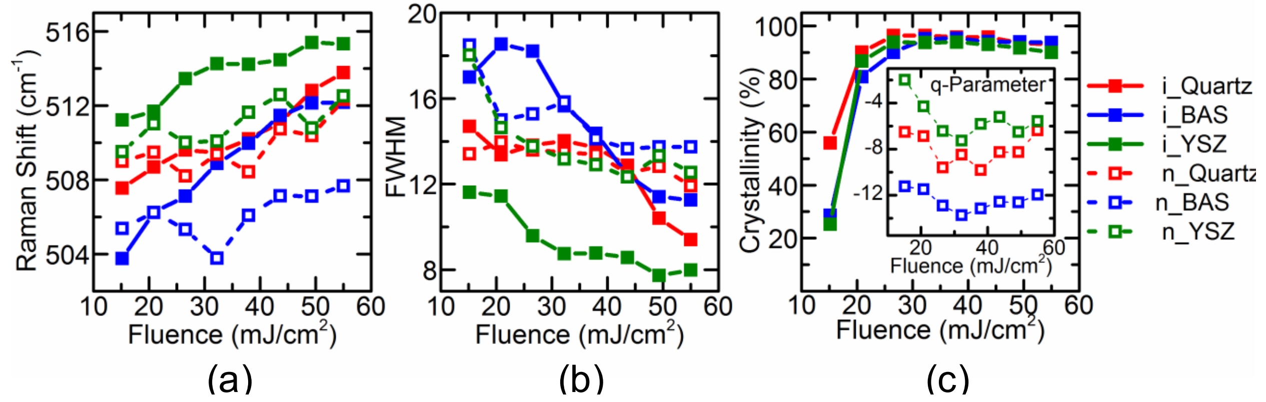

Figure 38. a) The Raman shift, b) FWHM, c) crystallinity and q-parameter (inset) for n-Si films plotted as a function of laser fluence. Open symbols with dashed lines denote n-Si and solid symbols with solid lines denote i-Si. Green denotes YSZ, red denotes quartz, and blue denotes BAS.[114]

XRD spectra of the samples were measured to identify the dependence of the mean crystallite diameter on substrate type and laser fluence. The most intense peak in the XRD spectra was the ⟨111⟩ peak at $2\theta = 28.4°$. As was done in the previous section, the FWHM of the ⟨111⟩ peak was used to calculate the crystallite diameter using the Scherrer equation. The results in Figure 39b show that the mean crystallite diameter increases with laser fluence until 27 mJ/cm^2 where the diameter remains constant at 35-50 nm. The smallest crystallite diameter was achieved on the c-Si substrate, which coordinated with the higher resistivity of films prepared on this same substrate. The resistivity of the films (Figure 39) reflects the trends seen in the morphology. Films on YSZ and c-Si become less resistive with increasing laser fluence until a critical fluence of 32 mJ/cm^2 is reached, at which point the resistivity remains constant. Once the films on quartz and BAS reach the same critical fluence, however, they become more resistive, which indicates a loss of percolation. As noted above, the two mechanisms compete with one another to reduce or enhance the conductivity. The conductivity of the film increases with

crystallinity, but decreases as it becomes less percolated. XRD shows that the film is fully crystallized at 27 mJ/cm^2, but transmission images indicate that the silicon does not begin to noticeably agglomerate until after 27 mJ/cm^2. The silicon agglomerates significantly more on quartz and BAS compared to the YSZ and c-Si substrates, suggesting that the quartz and BAS have a higher surface energy with L-Si than YSZ or c-Si.

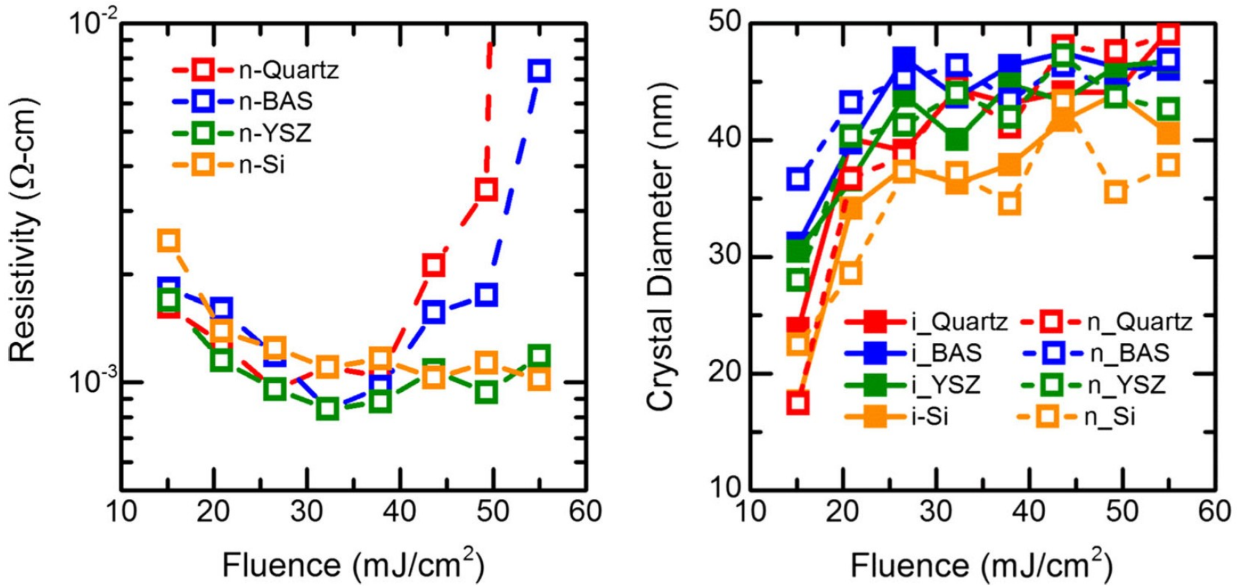

Figure 39. Resistivity (left) and crystallite diameter (right) of the i-Si and n-Si films plotted against laser fluence for the four different substrates.[114]

We used a numerical model to explain these measurements. The simulation, outlined in Appendix B, calculates both the percent crystallinity and the duration of time during which the surface of the film was in the liquid (melt) phase. The simulated crystallinity data agree relatively well with the Raman data, as shown in Figure 40 where crystallinity is graphed vs. laser fluence. The experiments showed little variation in crystallinity as a function of substrate material type, whereas the simulation predicted differing minimum laser fluences at which the film was fully crystallized. The films with the highest amount of agglomeration (BAS and quartz) had the highest simulated crystallization fluence. The simulation does not take into account changes in morphology; films that were more agglomerated are thus rougher and hence

absorb more laser energy. The simulated surface melt duration increases with laser fluence (Figure 40, right) and is greatly dependent on the substrate. Surprisingly, the surfaces of the samples that showed the least amount of agglomeration were in the liquid state the longest. This is counterintuitive with respect to the experimental results, but the surface energy of the film on the substrate is not accounted for in the simulations. Hence, we believe that the L-Si has higher surface interaction energy with quartz and BAS, which encourages the film to reduce its interfacial area with the substrates, whereas the L-Si has a lower surface interaction energy with the YSZ and c-Si substrates.

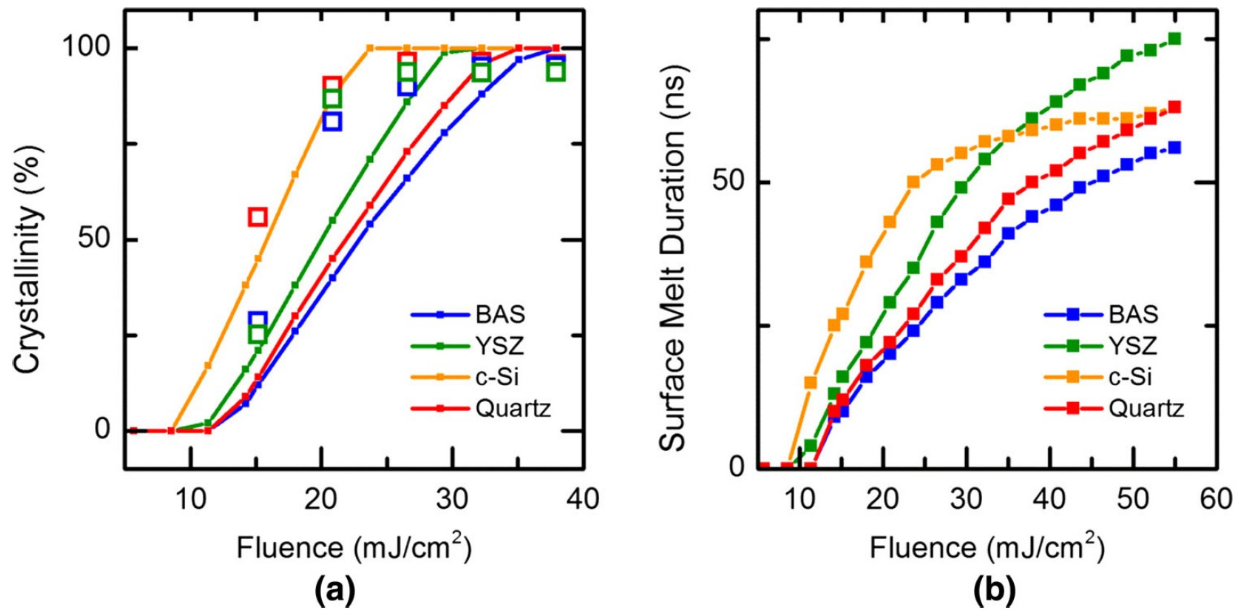

Figure 40. Left - simulated crystallinity (solid squares) and experimental crystallinity from Raman (open squares) versus laser fluence. Right - simulated surface melt duration versus laser fluence.[114]

In conclusion, we have measured the influence of laser crystallization on silicon film crystallinity, morphology, and conductivity as a function of laser fluence for different substrates and compared the measurements to a model simulation of the same process, where the simulations ignore morphological changes. It was found that for a common minimal optimum laser fluence of 27 mJ/cm^2 independent of substrate, the mean crystallite diameter is maximized

and the film resistivity is minimized. Laser fluences above this threshold led to increased agglomeration. The amount of agglomeration for a given fluence largely depends on the substrate, where the driving mechanism is the surface energy of the L-Si with respect to the substrate. Because the largest pillars grew on substrates with the shortest simulated surface melt time, the L-Si must have a higher surface energy to increase the flow of silicon to the pillars. This might be viewed as a very early stage of dewetting that is ultimately arrested by crystallization. Pillars only form above the critical fluence, when the film fully melts and the L-Si subsequently interacts unfavorably with the substrate. This repulsive force results in the formation of pillars. Higher laser fluences increase the melt duration of the film, which allows L-Si to flow for a longer duration, simultaneously reducing the percolation of the film and enhancing the size of the pillars.

Surface energies likely play a significant role in the pillar shape, as evidenced by the difference in morphology between the various substrates; however, with aspect ratios as high as 7:1 on BAS, it is unlikely that surface energy is the only contribution to the formation of the features. In research papers where silicon is textured with a laser, it has been noted that the pillars resemble silicon nanowires.[116] It was subsequently hypothesized that the growth mechanism is similar to the growth of nanowires, where silicon vapor attaches to the crystalline tips. Here, such an explanation is unlikely because the surface of the silicon does not reach the vaporization temperature, which we verified by scanning a c-Si wafer with the laser at the same threshold fluence with no detectable difference in morphology.

Other researchers have suggested that surface tension driven Marangoni flow and capillary waves may play important roles in the film morphology, including the large pillars.[77,117] The L-Si flows from hot to cool regions, and as it cools, capillary forces pull the silicon back to

form a peak. Small peaks are evident at fluences below the critical fluence, similar to those seen on the c-Si substrate in Figure 34, but this does not explain the stark contrast in morphology between silicon crystallized on different substrates, which we have shown is due to the difference in surface energies of the L-Si on the different substrates. We can rationalize this through the varied Hamaker constants of the substrates and the simple relationship $A_{12} \approx \sqrt{A_{11}A_{22}}$. For a larger Hamaker constant A_{12} between the substrate (material 1) and L-Si (material 2), the tendency for dewetting will be weaker. The approximate Hamaker constants of YSZ, c-Si, and amorphous SiO_2 can be found in the literature.[118] The similarity between the refractive indices of BAS and NaCl suggests that the Hamaker constant of BAS is approximately that of NaCl. The Hamaker constants of YSZ and c-Si are thus both roughly 4x those SiO_2 and BAS, which means the van der Waals attraction of the L-Si to the YSZ and c-Si substrates is approximately twice as strong as the attraction to SiO_2 and BAS, regardless of the magnitude of the Hamaker constant of L-Si. The stronger attraction of L-Si to c-Si and YSZ could effectively suppress dewetting and lead to a percolated film at high laser fluence, whereas a weaker attraction results in dewetting, regions of bare substrate, and large pillars.

7.3. Conclusion

Both film thickness and substrate composition have significant impacts on the morphology of the laser-crystallized silicon films. The substrate primarily determines whether a film remains percolated or agglomerates. On substrates where films prefer to agglomerate, thinner films agglomerate more readily at lower crystallization fluences, whereas thicker films require more energy and still thicker films remain percolated by forming a porous film.

The enhanced roughness caused by agglomeration of the film amplifies the absorption of the film, a desired quality for photovoltaic devices. The strong preference for the silicon to form

pillars on quartz and BAS can be exploited by patterning the substrate with a seed material, allowing for controlled growth of the silicon pillars. Depending on the preferred morphology, appropriate sample parameters can be used to obtain a film with the desired structure.

8. OUTLOOK

8.1. Reinforced Carbon Nanotube Films

Several obstacles remain for the implementation of SWCNT films in flexible electronics. The primary obstacle being SWCNTs are still quite expensive to synthesize and purify.[119] As production efficiencies improve, and if they do become widespread, handling procedures and recycling standards may be necessary, as SWCNTs have been possibly linked to potential health concerns.[120] SWCNTs have been compared to asbestos, which has been strongly linked to pulmonary health problems. Other competitive nanomaterials are also being considered as viable candidates that have properties comparable to SWCNTs, such as graphene.

Aside from the cost of production and potential health concerns, SWCNT films can be rather fragile when compressed, which could be a significant detriment for SWCNTs and their inclusion in flexible electronics. However, in this dissertation, it was shown that the addition of a polymer capping layer offers a potential way of mitigating strain softening. The capping layer significantly altered the mechanical properties of the SWCNT films, where the SWCNT film thickness played a critical role in determining if the film modulus was enhanced or the film was plasticized. It was noted that the depth of penetration of the polymer into the SWCNT film appears to be a limiting factor. Films thicker than this penetration depth were plasticized, whereas thinner films were reinforced. The mechanism by which the SWCNT film softens through the addition of the capping layer is not understood and requires further investigation. The strain-softening phenomenon was slightly reduced for sufficiently thin films; however more research must be done to further reduce the strain response of the CNTs if they are to be applied to flexible electronics.

Future work can be done to not only further reduce strain softening, but to replace the "passive" polymer filler with "active" filler materials, where passive materials strictly act to obstruct SWCNT movement, such as polymers or colloids, while active fillers provide additional preferential electronic properties, such as metallic nanoparticles or semiconducting quantum dots. A significant effort during the last year of this thesis research was directed at testing this idea using silver nanocrystal, silicon nanocrystals and CdSe quantum dots. To date, however, difficulties associated depositing uniform nanocrystal capping layers have impeded our progress, and this will thus need to be addressed in future work.

8.2. Laser-Crystallization of Silicon

Laser crystallization appears to be a promising technology that is quite versatile. Thin film transistors composed of poly-crystalline silicon are currently being integrated in to active matrix liquid-crystal displays (AMLCDs). Coherent, an commercial laser manufacturer, introduced a laser-crystallization platform (Vyper/LB759) in early 2011 for industrial applications, such as creating AMLCD displays. The presence of thin film silicon in solar cells is less developed. The current, bulk technologies are capable of achieving efficiencies of around 20 %, which is nearly double that of cells composed of laser-crystallized silicon.

The laser crystallization experiments discussed in this dissertation produced interesting morphologies. Both the film thickness and substrate composition had significant impact on the agglomeration of the films. The long crystals presented in the literature were not observed in these experiments, and the difference may be attributed to an incorrect combination of crystallization parameters, such as pulse overlap. Although flatter films with long crystals have better transport qualities, the rougher films produced on quartz and BAS are desirable for thin film solar cells because of the higher absorption of the films. Thin film solar cells need to be

thick enough to fully absorb light over the desired wavelength range. Rougher films, with high absorption coefficients, can reduce the needed thickness for absorption.

Film thickness and substrate composition had significant impacts on the structure of the crystallized films. On quartz and BAS, the silicon tended to agglomerate, forming structures an order of magnitude taller than the film thickness. Thinner films on quartz formed structures that left a bare substrate, whereas for thicker films, some silicon remained on the substrate, leaving a porous silicon network. YSZ and crystalline silicon substrates produced structures with much smaller agglomerates, resulting in a fully covered substrate. The root of the structural differences observed on different substrates was tentatively attributed to differences in Hamaker constant for the different materials. This suggests that for sufficiently thin films, for which the film completely agglomerates, it would be possible to control where the pillars grow by seeding the substrate with a material with a higher affinity, such as metallic nanoparticles. The ordered nanopillars could have potential applications in energy storage, similar to research performed on silicon nanowires, opening the door to new potential applications for laser treated silicon films.

REFERENCES

1 M. Ciesinski, in *Flexible Electronics: Why the Interest? Where are the markets? What's next?*, 2010.

2 S. Park and S. Jayaraman, Ieee Engineering in Medicine and Biology Magazine **22,** 41 (2003).

3 E. P. Kelly and G. S. Erickson, Industrial Management & Data Systems **105,** 703 (2005).

4 J. M. Harris, J. Y. Huh, M. R. Semler, T. Ihle, C. M. Stafford, S. D. Hudson, J. A. Fagan, and E. K. Hobbie, Soft Matter **9,** 11568 (2013).

5 E. K. Hobbie, D. O. Simien, J. A. Fagan, J. Y. Huh, J. Y. Chung, S. D. Hudson, J. Obrzut, J. F. Douglas, and C. M. Stafford, Physical Review Letters **104** (2010).

6 E. Menard, R. G. Nuzzo, and J. A. Rogers, Applied Physics Letters **86** (2005).

7 K. Gurnett and T. Adams, Iii-Vs Review **19,** 38 (2006).

8 G. R. S. Iyer, E. K. Hobbie, S. Guruvenket, J. M. Hoey, K. J. Anderson, J. Lovaasen, C. Gette, D. L. Schulz, O. F. Swenson, A. Elangovan, and P. Boudjouk, Acs Applied Materials & Interfaces **4,** 2680 (2012).

9 J. C. C. Fan and H. J. Zeiger, Applied Physics Letters **27,** 224 (1975).

10 N. H. Nickel, *Laser Crystallization of Silicon*, Vol. 75 (Elsevier Ltd, Kidlington, Oxford UK, 2003).

11 A. Imparato, C. Minarini, A. Rubino, P. Tassini, F. Villani, D. Della Sala, E. Amendola, M. Kunst, H. C. Neitzert, and S. Bellone, Thin Solid Films **487,** 58 (2005).

12 K. H. Cui, A. S. Anisimov, T. Chiba, S. Fujii, H. Kataura, A. G. Nasibulin, S. Chiashi, E. I. Kauppinen, and S. Maruyama, Journal of Materials Chemistry A **2,** 11311 (2014).

13 D. D. Tune, B. S. Flavel, R. Krupke, and J. G. Shapter, Advanced Energy Materials **2,** 1043 (2012).

14 F. Wang, D. Kozawa, Y. Miyauchi, K. Hiraoka, S. Mouri, Y. Ohno, and K. Matsuda, Acs Photonics **1,** 360 (2014).

15 J. M. Harris, M. R. Semler, S. May, J. A. Fagan, and E. K. Hobbie, Journal of Physical Chemistry C **119,** 10295 (2015).

16 S. Varlamov, J. Dore, R. Evans, D. Ong, B. Eggleston, O. Kunz, U. Schubert, T. Young, J. Huang, T. Soderstrom, K. Omaki, K. Kim, A. Teal, M. Jung, J. Yun, Z. M. Pakhuruddin, R. Egan, and M. A. Green, Solar Energy Materials and Solar Cells **119,** 246 (2013).

17 J. Plentz, G. Andra, A. Gawlik, I. Hoger, G. B. Jia, and F. Falk, Thin Solid Films **562,** 430 (2014).

18 J. Dore, R. Evans, U. Schubert, B. D. Eggleston, D. Ong, K. Kim, J. L. Huang, O. Kunz, M. Keevers, R. Egan, S. Varlamov, and M. A. Green, Progress in Photovoltaics **21,** 1377 (2013).

19 E. S. Snow, P. M. Campbell, M. G. Ancona, and J. P. Novak, Applied Physics Letters **86** (2005).

20 R. Dassow, J. R. Kohler, Y. Helen, K. Mourgues, O. Bonnaud, T. Mohammed-Brahim, and J. H. Werner, Semiconductor Science and Technology **15,** L31 (2000).

21 A. A. Green and M. C. Hersam, Nano Letters **8,** 1417 (2008).

22 J. M. Harris, G. R. S. Iyer, D. O. Simien, J. A. Fagan, J. Y. Huh, J. Y. Chung, S. D. Hudson, J. Obrzut, J. F. Douglas, C. M. Stafford, and E. K. Hobbie, Journal of Physical Chemistry C **115,** 3973 (2011).

23 J. Li, L. Hu, L. Wang, Y. Zhou, G. Gruner, and T. J. Marks, Nano Letters **6,** 2472 (2006).

24 H.-Z. Geng, K. K. Kim, K. P. So, Y. S. Lee, Y. Chang, and Y. H. Lee, Journal of the American Chemical Society **129,** 7758 (2007).

25 J. A. Fagan, M. L. Becker, J. Chun, and E. K. Hobbie, Advanced Materials **20,** 1609 (2008).

26 J. A. Fagan, J. Y. Huh, J. R. Simpson, J. L. Blackburn, J. M. Holt, B. A. Larsen, and A. R. H. Walker, Acs Nano **5,** 3943 (2011).

27 M. S. Arnold, A. A. Green, J. F. Hulvat, S. I. Stupp, and M. C. Hersam, Nature Nanotechnology **1,** 60 (2006).

28 J. M. Harris, G. R. S. Iyer, A. K. Bernhardt, J. Y. Huh, S. D. Hudson, J. A. Fagan, and E. K. Hobbie, Acs Nano **6,** 881 (2012).

29 M. Moravej, S. E. Babayan, G. R. Nowling, X. Iang, and R. F. Hicks, Plasma Sources Science & Technology **13,** 8 (2004).

30 J. M. Bovatsek and R. S. Patel, in *Highest-speed dicing of thin silicon wafers with nanosecond-pulse 355nm q-switched laser source using line-focus fluence optimization technique*, San Francisco, CA, 2010.

31 R. S. Sposili and J. S. Im, Applied Physics a-Materials Science & Processing **67,** 273 (1998).

32 Y. Helen, R. Dassow, M. Nerding, K. Mourgues, F. Raoult, J. R. Kohler, T. Mohammed-Brahim, R. Rogel, O. Bonnaud, J. H. Werner, and H. P. Strunk, Thin Solid Films **383,** 143 (2001).

33 P. Lengsfeld, N. H. Nickel, and W. Fuhs, Applied Physics Letters **76,** 1680 (2000).

34 F. M. Smits, Bell System Technical Journal **34,** 711 (1958).

35 C. M. Stafford, C. Harrison, K. L. Beers, A. Karim, E. J. Amis, M. R. Vanlandingham, H. C. Kim, W. Volksen, R. D. Miller, and E. E. Simonyi, Nature Materials **3,** 545 (2004).

36 K. E. Petersen and C. R. Guarnieri, Journal of Applied Physics **50,** 6761 (1979).

37 E. K. Dimitriadis, F. Horkay, J. Maresca, B. Kachar, and R. S. Chadwick, Biophysical Journal **82,** 2798 (2002).

38 H. Jiang, D.-Y. Khang, J. Song, Y. Sun, Y. Huang, and J. A. Rogers, Proceedings of the National Academy of Sciences of the United States of America **104,** 15607 (2007).

39 C. M. Stafford, S. Guo, C. Harrison, and M. Y. M. Chiang, Review of Scientific Instruments **76** (2005).

40 A. J. Nolte, R. E. Cohen, and M. F. Rubner, Macromolecules **39,** 4841 (2006).

41 C. M. Stafford, B. D. Vogt, C. Harrison, D. Julthongpiput, and R. Huang, Macromolecules **39,** 5095 (2006).

42 R. H. Baughman, A. A. Zakhidov, and W. A. de Heer, Science **297,** 787 (2002).

43 M. J. Green, N. Behabtu, M. Pasquali, and W. W. Adams, Polymer **50,** 4979 (2009).

44 J. W. G. Wildoer, L. C. Venema, A. G. Rinzler, R. E. Smalley, and C. Dekker, Nature **391,** 59 (1998).

45 P. M. Ajayan and J. M. Tour, Nature **447,** 1066 (2007).

46 R. S. Ruoff, D. Qian, and W. K. Liu, Comptes Rendus Physique **4,** 993 (2003).

47 K. I. Tserpes and P. Papanikos, Composites Part B-Engineering **36,** 468 (2005).

48 M.-S. Wang, D. Golberg, and Y. Bando, Advanced Materials **22,** 4071 (2010).

49 M. M. J. Treacy, T. W. Ebbesen, and J. M. Gibson, Nature **381,** 678 (1996).

50 H. M. Ledbetter and E. R. Naimon, Journal of Physical and Chemical Reference Data **3,** 897 (1974).

51 W. D. Jenkins, T. G. Digges, and C. R. Johnson, Journal of Research of the National Bureau of Standards **58,** 201 (1957).

52 W. E. M. Luecke, J.D., C. N. McCowan, S. W. Banovic, R. J. Fields, T. Foecke, T. A. Siewert, and F. W. Gayle, (National Institute of Standards and Technology, 2005).

53 K. Miyake, N. Satomi, and S. Sasaki, Applied Physics Letters **89,** 3 (2006).

54 I. Y. Gnip, S. Vejelis, V. Kersulis, and S. Vaitkus, Polymer Testing **26,** 886 (2007).

55 N. Ashcroft and N. Mermin, *Solid State Physics* (Brooks/Cole, Belmont, CA, 1976).

56 G. G. Samsonidze, R. Saito, A. Jorio, M. A. Pimenta, A. G. Souza, A. Gruneis, G. Dresselhaus, and M. S. Dresselhaus, Journal of Nanoscience and Nanotechnology **3,** 431 (2003).

57 J.-C. Blancon, M. Paillet, H. N. Tran, T. Xuan Tinh, S. A. Guebrou, A. Ayari, A. San Miguel, P. Ngoc-Minh, A.-A. Zahab, J.-L. Sauvajol, N. Del Fatti, and F. Vallee, Nature Communications **4** (2013).

58 M. S. Dresselhaus, G. Dresselhaus, R. Saito, and A. Jorio, Physics Reports-Review Section of Physics Letters **409,** 47 (2005).

59 A. Jorio, R. Saito, J. H. Hafner, C. M. Lieber, M. Hunter, T. McClure, G. Dresselhaus, and M. S. Dresselhaus, Physical Review Letters **86,** 1118 (2001).

60 K. A. Wepasnick, B. A. Smith, J. L. Bitter, and D. H. Fairbrother, Analytical and Bioanalytical Chemistry **396,** 1003 (2010).

61 M. Meyyappan, Journal of Physics D-Applied Physics **42** (2009).

62 C. D. Scott, S. Arepalli, P. Nikolaev, and R. E. Smalley, Applied Physics a-Materials Science & Processing **72,** 573 (2001).

63 Z. J. Shi, Y. F. Lian, X. H. Zhou, Z. N. Gu, Y. G. Zhang, S. Iijima, L. X. Zhou, K. T. Yue, and S. L. Zhang, Carbon **37,** 1449 (1999).

64 J. Prasek, J. Drbohlavova, J. Chomoucka, J. Hubalek, O. Jasek, V. Adam, and R. Kizek, Journal of Materials Chemistry **21,** 15872 (2011).

65 R. E. Smalley, Accounts of Chemical Research **25,** 98 (1992).

66 S. Ghosh, S. M. Bachilo, and R. B. Weisman, Nature Nanotechnology **5,** 443 (2010).

67 M. Lucas, X. H. Zhang, I. Palaci, C. Klinke, E. Tosatti, and E. Riedo, Nature Materials **8,** 876 (2009).

68 E. K. Hobbie, T. Ihle, J. M. Harris, and M. R. Semler, Physical Review B **85** (2012).

69 M. R. Semler, J. M. Harris, and E. K. Hobbie, Journal of Chemical Physics **141** (2014).

70 M. R. Semler, J. M. Harris, A. B. Croll, and E. K. Hobbie, Physical Review E **88,** 7 (2013).

71 M. R. Semler, J. M. Harris, and E. K. Hobbie, Journal of Chemical Physics **141,** 8 (2014).

72 R. F. Gibson, *Principles of Composite Material Mechanics* (McGraw Hill Inc., United States, 1994).

73 D.-Y. Khang, J. Xiao, C. Kocabas, S. MacLaren, T. Banks, H. Jiang, Y. Y. Huang, and J. A. Rogers, Nano Letters **8,** 124 (2008).

74 G. E. Jellison and F. A. Modine, Physical Review B **27,** 7466 (1983).

75 M. O. Thompson, G. J. Galvin, J. W. Mayer, P. S. Peercy, J. M. Poate, D. C. Jacobson, A. G. Cullis, and N. G. Chew, Physical Review Letters **52,** 2360 (1984).

76 I. A. Palani, N. J. Vasa, M. Singaperumal, and T. Okada, Thin Solid Films **518,** 4183 (2010).

77 I. A. Palani, N. J. Vasa, M. Singaperumal, and T. Okada, Journal of Laser Micro Nanoengineering **5,** 150 (2010).

78 O. Garcia, J. J. Garcia-Ballesteros, D. Munoz-Martin, S. Nunez-Sanchez, M. Morales, J. Carabe, I. Torres, J. J. Gandia, and C. Molpeceres, Applied Surface Science **278,** 214 (2013).

79 M. Nerding, R. Dassow, S. Christiansen, J. R. Kohler, J. Krinke, J. H. Werner, and H. P. Strunk, Journal of Applied Physics **91,** 4125 (2002).

80 D. Chunyan, L. Chao, A. Bin, L. Jianjun, D. Youjun, and S. Hui, Journal of Semiconductors **32,** 123002 (2011).

81 P. D. Veneri, M. L. Addonizio, A. Imparato, C. Minarini, C. Privato, and E. Terzini, Materials Science and Engineering B-Solid State Materials for Advanced Technology **69,** 227 (2000).

82 J. F. Michaud, R. Rogel, T. Mohammed-Brahim, and M. Sarret, Journal of Non-Crystalline Solids **352,** 998 (2006).

83 S. Kawamura, J. Sakurai, M. Nakano, and M. Takagi, Applied Physics Letters **40,** 394 (1982).

84 E. L. Mathe, A. Naudon, M. Elliq, E. Fogarassy, and S. Deunamuno, Applied Surface Science **54,** 392 (1992).

85 J. S. Im, H. J. Kim, and M. O. Thompson, Applied Physics Letters **63,** 1969 (1993).

86 J. S. Im and H. J. Kim, Applied Physics Letters **64,** 2303 (1994).

87 J. S. Im, R. S. Sposili, and M. A. Crowder, Applied Physics Letters **70,** 3434 (1997).

88 M. Hatano, S. Moon, M. Lee, K. Suzuki, and C. P. Grigoropoulos, Journal of Applied Physics **87,** 36 (2000).

89 S. D. Brotherton, D. J. McCulloch, J. B. Clegg, and J. P. Gowers, Ieee Transactions on Electron Devices **40,** 407 (1993).

90 D. J. McCulloch and S. D. Brotherton, Applied Physics Letters **66,** 2060 (1995).

91 M. Lee, S. Moon, M. Hatano, K. Suzuki, and C. P. Grigoropoulos, Journal of Applied Physics **88,** 4994 (2000).

92 M. Miyasaka and J. Stoemenos, Journal of Applied Physics **86,** 5556 (1999).

93 E. P. Donovan, F. Spaepen, D. Turnbull, J. M. Poate, and D. C. Jacobson, Applied Physics Letters **42,** 698 (1983).

94 R. A. L. Jones, *Soft Condense Matter* (Oxford university Press, University of Oxford, 2002).

95 J. C. Fisher, J. H. Hollomon, and D. Turnbull, Journal of Applied Physics **19,** 775 (1948).

96 A. Ziabicki, Journal of Chemical Physics **48,** 4368 (1968).

97 R. Tsu, J. Gonzalezhernandez, S. S. Chao, S. C. Lee, and K. Tanaka, Applied Physics Letters **40,** 534 (1982).

98 A. Adikaari and S. R. P. Silva, Journal of Applied Physics **97** (2005).

99 R. S. Sposili and J. S. Im, Applied Physics Letters **69,** 2864 (1996).

100 J. Jin, Z. Yuan, L. Huang, S. Chen, W. Shi, Z. Cao, and Q. Lou, Applied Surface Science **256,** 3453 (2010).

101 X. C. Wang, H. Y. Zheng, C. W. Tan, F. Wang, H. Y. Yu, and K. L. Pey, Optics Express **18,** 19379 (2010).

102 M. He, R. Ishihara, E. J. J. Neihof, Y. van Andel, H. Schellevis, W. Metselaar, and K. Beenakker, Japanese Journal of Applied Physics Part 1-Regular Papers Brief Communications & Review Papers **46,** 1245 (2007).

103 A. Marmorstein, A. T. Voutsas, and R. Solanki, Journal of Applied Physics **82,** 4303 (1997).

104 Y. Kimura, M. Kishi, and T. Katoda, Journal of Applied Physics **86,** 2278 (1999).

105 P. Lengsfeld, N. H. Nickel, C. Genzel, and W. Fuhs, Journal of Applied Physics **91,** 9128 (2002).

106 G. G. Stoney, Proceedings of the Royal Society of London Series a-Containing Papers of a Mathematical and Physical Character **82,** 172 (1909).

107 M. R. Semler, J. M. Hoey, S. Guruvenket, C. R. Gette, O. F. Swenson, and E. K. Hobbie, Journal of Applied Physics **115,** 6 (2014).

108 C. Smit, R. van Swaaij, H. Donker, A. Petit, W. M. M. Kessels, and M. C. M. van de Sanden, Journal of Applied Physics **94,** 3582 (2003).

109 B. D. Cullity, *Elements of X-Ray Diffraction* (Addison-Wesley Publishing Company, Inc., 1956).

110 D. B. Buchholz, J. Liu, T. J. Marks, M. Zhang, and R. P. H. Chang, Acs Applied Materials & Interfaces **1,** 2147 (2009).

111 W. Bludau, A. Onton, and W. Heinke, Journal of Applied Physics **45,** 1846 (1974).

112 J. I. Pankove and D. E. Carlson, Annual Review of Materials Science **10,** 43 (1980).

113 N. H. Nickel, P. Lengsfeld, and I. Sieber, Physical Review B **61,** 15558 (2000).

114 M. R. Semler, J. M. Hoey, S. Guruvenket, O. F. Swenson, and E. K. Hobbie, Applied Physics a-Materials Science & Processing **120,** 1545 (2015).

115 P. Lengsfeld, S. Brehme, K. Brendel, C. Genzel, and N. H. Nickel, Physica Status Solidi B-Basic Research **235,** 170 (2003).

116 A. J. Pedraza, J. D. Fowlkes, and D. H. Lowndes, Applied Physics Letters **74,** 2322 (1999).

117 D. K. Fork, G. B. Anderson, J. B. Boyce, R. I. Johnson, and P. Mei, Applied Physics Letters **68,** 2138 (1996).

118 L. Bergstrom, Advances in Colloid and Interface Science **70,** 125 (1997).

119 M. F. L. De Volder, S. H. Tawfick, R. H. Baughman, and A. J. Hart, Science **339,** 535 (2013).

120 A. Helland, P. Wick, A. Koehler, K. Schmid, and C. Som, Environmental Health Perspectives **115,** 1125 (2007).

121 H. C. Webber, A. G. Cullis, and N. G. Chew, Applied Physics Letters **43,** 669 (1983).

122 Y. B. Magomedov and G. G. Gadjiev, High Temperature **46,** 422 (2008).

123 T. Nishi, H. Shibata, and H. Ohta, Materials Transactions **44,** 2369 (2003).

124 K. L. Wray and T. J. Connolly, Journal of Applied Physics **30,** 1702 (1959).

125 (Corning, 2002).

126 K. Sasaki, T. Terai, A. Suzuki, and N. Akasaka, International Journal of Applied Ceramic Technology **7,** 518 (2010).

127 P. D. Desai, Journal of Physical and Chemical Reference Data **15,** 967 (1986).

128 B. S. Hemingway, American Mineralogist **72,** 273 (1987).

129 D. T. Pierce and W. E. Spicer, Physical Review B **5,** 3017 (1972).

130 B. Rezek, C. E. Nebel, and M. Stutzmann, Journal of Applied Physics **91,** 4220 (2002).

131 D. E. Aspnes and A. A. Studna, Physical Review B **27,** 985 (1983).

132 K. D. Li and P. M. Fauchet, Applied Physics Letters **51,** 1747 (1987).

133 (Technical Glass Products, 2010).

APPENDIX A. BEAM SIZE MEASUREMENTS

The beam was characterized using an Ophir Photonics beam profiler using BeamGage software. The profiler was placed below the scanhead, and stages were used to position the profiler so as to center the beam. The rotation stage on which the cylindrical lenses were mounted was rotated until the elliptical beam was parallel to the software window. The profiler was raised, using the z-stage, until the minor axis of the beam was at a minimum. To ensure that the beam was focused, the profiler was lowered by 500 μm and profiles were taken every 100 μm until the profiler was 500 μm above the anticipated focal plane.

The beam dimensions were measured for each profile and the profile with the narrowest minor axis was determined to be at the focal height. Ten profiles were taken at the focal height and the average major and minor axis was calculated. The beam dimensions were determined by fitting a Gaussian to the major and minor axis beam profiles. Due to the small sample size along the minor axis, the height of the Gaussian was determined from the major axis, and it was fixed during the fitting of the minor axis. A sample profile of the major and minor axes with the fit is shown in Figure A1.

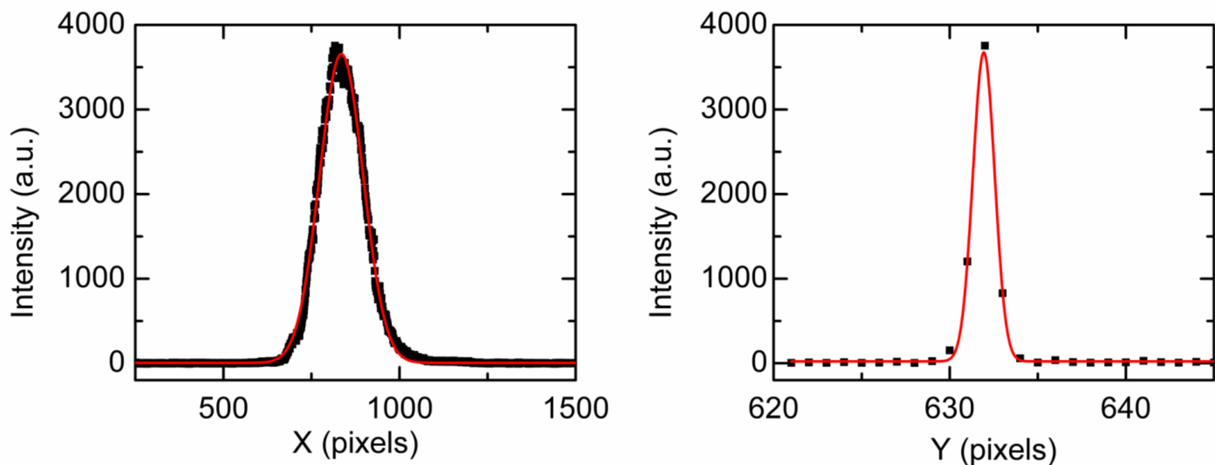

Figure A1. Gaussian fits to the major (left) and minor (right) axes.

APPENDIX B. LASER-CRYSTALLIZATION SIMULATION DERIVATION AND VERIFICATION

The programming language Java was used to write code designed to numerically solve the heat equation with a source term due to laser heating. The equation was discretized into cubic nanometer cells. Since the intensity of the beam varies slowly over the range of a nanometer, the one-dimensional heat equation was used. The simulated system consists of a 100 nm thick amorphous silicon film on an infinitely thick substrate. To minimize runtimes, the minimum thickness of the substrate was determined by increasing the thickness until the temperature profile at the base of the film was negligibly affected.

B.1. Discretization of the Heat Equation

The 1D heat equation is given by:

$$c_p(T)\rho(T)\frac{\partial U(z,t)}{\partial t} = \frac{\mathrm{d}}{\mathrm{dz}}\left[\kappa(T)\frac{\mathrm{d}U(z,t)}{dz}\right] + S(z,t). \qquad \text{(B1)}$$

Using the chain rule, B1 can be simplified to

$$c_p(T)\rho(T)\frac{\partial U(z,t)}{\partial t} = \frac{\partial \kappa(T)}{\partial T}\left(\frac{\partial \mathrm{U(z,t)}}{\partial \mathrm{z}}\right)^2 + \kappa(T)\frac{\partial^2 \mathrm{U(z,t)}}{\partial \mathrm{z}^2} + S(z,t). \qquad \text{(B2)}$$

The finite difference method used to discretize the heat equation:

$$\frac{dy}{dx} = \frac{y(x+dx) - y(x)}{dx}. \qquad \text{(B3)}$$

Applying B3 to B2, the equation becomes:

$$c_p\rho\left(\frac{U_z^{t+\Delta t} - U_z^t}{\Delta t}\right) = \frac{d\kappa}{dU}\left(\frac{U_{z+\Delta z}^t - U_z^t}{\Delta z}\right)^2 + \kappa\left(\frac{U_{z+\Delta z}^t - U_z^t + U_{z-\Delta z}^t}{\Delta z^2}\right) + S(z,t) \qquad \text{(B4)}$$

and by rearranging, we can solve for $U_z^{t+\Delta t}$:

$$U_z^{t+\Delta t} = \frac{\Delta t}{\Delta z^2 c_p \rho}\left[\frac{d\kappa}{dU}(U_{z+\Delta z}^t - U_z^t)^2 + \kappa(U_{z+\Delta z}^t - U_z^t + U_{z-\Delta z}^t)\right] + U_z^t + \frac{\Delta t}{c_p \rho}S(z,t). \quad \text{(B5)}$$

The source term is due to the non-reflected energy absorbed by the film. It is both temporally and spatially dependent. The laser has a Gaussian intensity distribution in the XY plane, so as it scans across the sample, the intensity changes. The pulse has a temporal Gaussian shape with a pulse width of 12 ns, so over the course of 24 ns, the source terms increases to the maximum then decreases back to zero. The absorbed energy is the gradient of the absorbance, given by:

$$\nabla A = -\nabla T = -\frac{d}{dz}(I_o e^{-\alpha z}) = I_o \alpha e^{-\alpha z}\ . \quad \text{(B6)}$$

The source term is then:

$$S(x,y,z,t) = I(x,y,t)(1-R)\alpha e^{-\alpha z} \quad \text{(B7)}$$

where I is the maximum intensity, α is the absorption coefficient, and R is the reflectance. Because the absorption changes with the state of the material, it too must be discretized. This is achieved by calculating the energy absorbed by a given cell. The discretized source term then becomes

$$S_{z+\Delta z}(x,y,t) = I(x,y,t)(1-R)e^{-\alpha \Delta z}(1-e^{-\alpha \Delta z}). \quad \text{(B8)}$$

The spatial intensity of the beam is given by

$$I(x,y) = I_o e^{-\left(\frac{2x^2}{a^2}+\frac{2y^2}{b^2}\right)} \quad \text{(B9)}$$

where I_o is the maximum intensity, and a and b are the minor and major axes, respectively.

The average power is used to determine I_o. The average power is the integral over space of the intensity:

$$P_{avg} = \int_{-\infty}^{\infty} \int_{-\infty}^{\infty} I(x,y) dxdy\,, \tag{B10}$$

$$P_{avg} = \int_{-\infty}^{\infty} \int_{-\infty}^{\infty} I_o e^{-\left(\frac{2x^2}{a^2}+\frac{2y^2}{b^2}\right)} dxdy\,, \tag{B11}$$

$$P_{avg} = \frac{I_o \pi ab}{2}\,, \tag{B12}$$

$$I_o = \frac{2P_{avg}}{\pi ab}\,. \tag{B13}$$

Pulsed lasers concentrate the intensity into a small pulse of energy with a Gaussian distribution. Using a FWHM pulse width, the peak power is given by:

$$P_{peak} \approx .94 \frac{P_{avg}}{F\tau} \tag{B14}$$

where F is the repetition rate of the laser and τ is the pulse width. The pulse has a temporal Gaussian distribution, so with a FWHM pulse width of τ:

$$I(t) = I_o e^{-4\ln(2)\frac{(t-t_o)^2}{\tau^2}} \tag{B15}$$

$$I(t) \approx I_o e^{-2.77\frac{(t-t_o)^2}{\tau^2}}\,. \tag{B16}$$

The net intensity is thus given by:

$$I(x,y,t) = 0.94 \frac{2}{\pi ab} \frac{P_{avg}}{F\tau} e^{-2.77\frac{(t-t_o)^2}{\tau^2}} e^{-\left(\frac{2x^2}{a^2}+\frac{2y^2}{b^2}\right)} \tag{B17}$$

which is used with (B6) to determine the source term for each cell. The source term is assumed to be zero in the film for depths greater than 50 nm to reduce computation time.

The phase-change process of silicon was simulated by fixing the temperature of a cell undergoing the phase change until the cell has absorbed/released enough latent heat. The cell begins a phase change if a) the film is a-Si just at/above the melting temperature of a-Si, b) the

film is c-Si just at/above the melting temperature of c-Si, or c) the film is L-Si at or below the freezing temperature of L-Si and is no longer gaining energy.

The film is melting if the stored latent heat is less than the latent heat of fusion, i.e. $0 < q < L_f$, whereas the film is crystallizing if the stored latent heat, which is negative by definition, is greater than the negative latent heat of fusion, i.e. $-L_f < q < 0$.

For each iteration, the temperature of the cell is determined as if it were not undergoing a phase transition to determine the amount of heat energy the cell absorbs. The change in latent energy is then given by:

$$\Delta Q = c_p \rho (\Delta x)^3 \Delta T \tag{B18}$$

The temperature is reset to the melting temperature, and the thermal energy is added to the cell's accumulated latent energy. If the accumulated latent energy exceeds the latent heat of fusion, the cell's accumulated latent energy is set to 0, and is no longer undergoing a phase change. It is possible that during a single iteration the cell receives more latent energy than required for a phase change, so any excess latent energy is converted to an increase in energy.

B.2. Code Verification

The discretized heat equation (B4) was tested by fixing the temperature of a wire at each end and calculating the time evolution of the temperature of the wire, where the analytical solution is known and is given by:

$$T(x,t) = T_o + \left(T_o \frac{x}{L}\right) + \sum_{n=1}^{\infty} (-1)^n \frac{2T_o}{n\pi} \sin\left(\frac{n\pi x}{L}\right) e^{-\frac{n^2 \pi^2 k t}{c\rho L^2}} . \tag{B19}$$

The temperature profiles at different times are plotted in Figure B1for the theory and the simulation, where the numerical solution closely matches the theoretical values.

Table B1. Simulation parameters used to verify heat equation.

Parameter	Value
c	$952\ \frac{nm^2}{ns^2 K}$
κ	$5E-15\ \frac{g\ nm}{ns^3 K}$
ρ	$2.2E-21\ \frac{g}{nm^3}$
L	$400\ nm$
T_1	$300\ K$
T_2	$1700\ K$

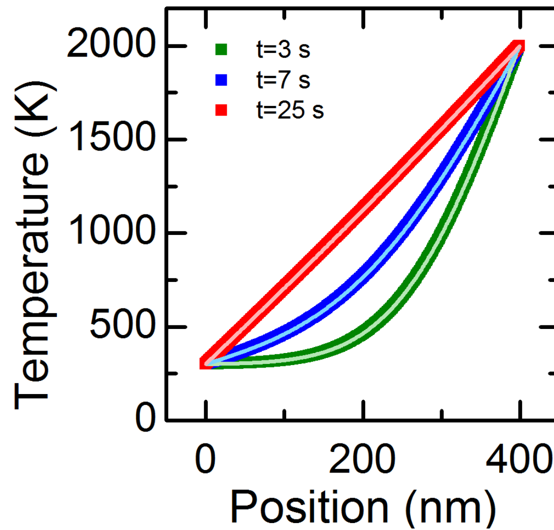

Figure B1. Temperature profiles of a wire with the ends fixed at 300 and 2000 K. The thick dark lines are the data collected from the simulation and the pastel lines are the theoretical values calculated from Equation B9.

The discretized source term was plotted as a function of depth at a fixed time, and as a function of time at the surface, as shown in Figure B2. Each pulse has a FWHM of 12 ns and a repetition rate of 33 MHz, resulting in 30 ns between consecutive pulses. A scan speed of 16.7 m/s results in a pulse-to-pulse spatial separation of 0.5 µm. To make it easier to portray the data and the fit, 30 ns is assumed between pulses. Figure B2(a) shows the value of the source term as

a function of depth. The theoretical fit (B5) is plotted in red and is in excellent agreement. Figure B2(b) shows an individual pulse of the source term as a function of time whereas Figure B2(c) show the time-dependent source term over the course of consecutive pulses. The theoretical values for Figure B2(b) and Figure B2(c) were calculated using Equations (B5) and (B7).

Table B2. Simulation parameters used to verify laser-heating source term.

Parameter	Value
τ	$12\ ns$
f	$.033\ ns^{-1}$
v	$16.7\ \frac{m}{s}$
a	$763000\ nm$
b	$5500\ nm$
P_{avg}	$2.2E-06\ \frac{g\ nm^2}{ns^3}$
R	0.50472
α	$0.101\ nm^{-1}$

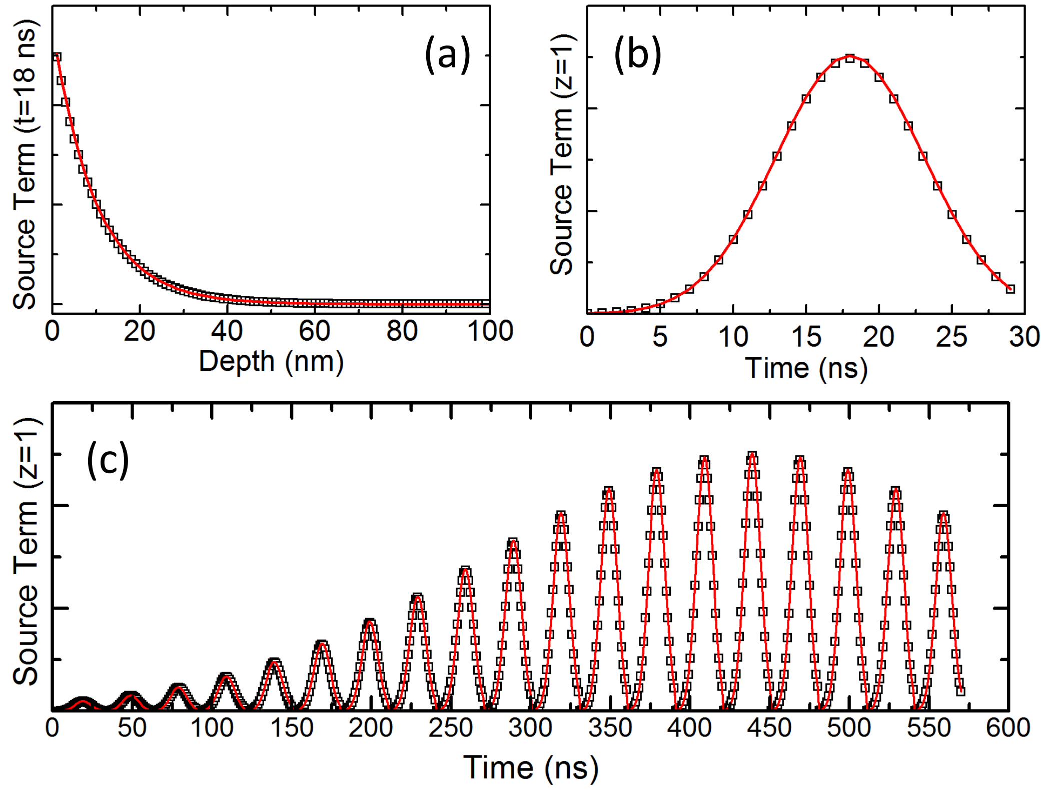

Figure B2. Plots of the source term as a function of (a) depth, and (b, c) time.

Lastly, the phase change mechanism was verified by applying the heat equation to a wire with a uniform, constant heat source. Due to uniform heating, there is no temperature gradient in the wire, so the solution is linear with time until the melting temperature is reached. The phase transition duration is given by

$$t = \frac{L_h m}{P} \tag{B20}$$

where L_h is the latent heat of fusion, m is the mass, and P is the power of the heat source. Equation (B10) predicts the wire will take 29.04 ns to complete the phase change, which is in excellent agreement with 29.0 ns predicted by the numerical solution of the heat equation.

Table B3. Simulation parameters used to verify phase transition mechanism.

Parameter	Value
c	$1000\,\frac{nm^2}{ns^2}$
ρ	$2.2E-21\,\frac{g}{nm^3}$
T_amb	$300\ K$
L_f	$1.32E6\ nm^2/ns^2$
P	$1E-16\ \frac{g\ nm^2}{ns^3}$

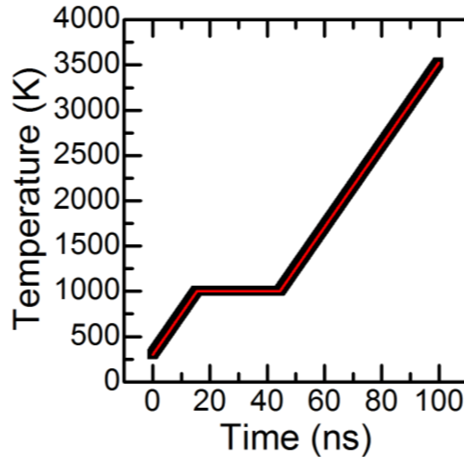

Figure B3. Temperature of a wire uniformly heated past the melting temperature.

B.3. Thermal Properties of Materials

Temperature dependent thermal properties of amorphous, crystalline, and molten silicon and the thermal properties of the substrates were obtained from the literature and are shown in the tables below. Curves were fit to the thermal conductivity and heat capacity data obtained from the references listed. Laser parameters used during silicon crystallization simulations are also shown in Tables B4-B7.

Table B4. Fits of thermal conductivities used during silicon crystallization simulations.

Material	Thermal Conductivity	Ref
a-Si $\left(\frac{W}{cm\,K}\right)$	$4.8 \times 10^{-11}(T-900)^3 + 4.8 \times 10^{-9}(T-900)^2 + 3.7 \times 10^{-6}(T-900) + 3.7 \times 10^{-2}$	[121]
c-Si $\left(\frac{W}{m\,K}\right)$	$19.1 + 2.7 \times 10^{-3}\,T - 1.3 \times 10^{-5}\,T^2 + 5.9 \times 10^{-9}\,T^3$	[122]
L-Si $\left(\frac{W}{m\,K}\right)$	$5.71 \times 10^{-4}(T-1685) + 58.6$	[123]
Quartz $\left(\frac{cal}{cm\,s\,K}\right)$	$1.970 \times 10^{-3} + 8.3 \times 10^{-7}\,T + 6.54 \times 10^{-9}\,T^2 - 5.7 \times 10^{-12}\,T^3 + 1.3 \times 10^{-15}\,T^4$	[124]
BAS $\left(\frac{cal}{cm\,s\,K}\right)$	$4.2 \times 10^{-3} - 3.3 \times 10^{-3}\exp(-T/611)$	[125]
YSZ $\left(\frac{W}{m\,K}\right)$	$2.0 - 2.3\exp(-T/144.1)$	[126]

Table B5. Fits of heat capacities used during silicon crystallization simulations.

Material	Heat Capacity	Ref
a-Si $\left(\frac{J}{g\,K}\right)$	$0.952 + 0.171T/1685$	[121]
c-Si $\left(\frac{J}{mol\,K}\right)$	$13.3 + 3.3 \times 10^{-2}\,T - 3.5 \times 10^{-5}\,T^2 + 1.8 \times 10^{-8}\,T^3 - 3.5 \times 10^{-12}\,T^4$	[127]
L-Si $\left(\frac{J}{mol\,K}\right)$	27.2	[127]
Quartz $\left(\frac{J}{mol\,K}\right)$	$-3.1 + 0.2\mathrm{T} - 2.8 \times 10^{-4}\mathrm{T}^2 + 1.5 \times 10^{-7}\mathrm{T}^3 - 2.9 \times 10^{-11}\mathrm{T}^4$	[128]
BAS $\left(\frac{cal}{g\,K}\right)$	$0.3 - 0.3\exp(-\mathrm{T}/614)$	[125]
YSZ $\left(\frac{J}{mol\,K}\right)$	$83.9 - 65.7\exp(-\mathrm{T}/425)$	[126]

Table B6. Material properties used for silicon crystallization simulation.

	Reflectance	Absorption Coefficient (cm^{-1})	Melting Temperature (K)	Latent Heat of Fustion (J/kg)	Density (g/cm^3)
a-Si	0.50[129]	1.01E6	1420[93]	1320E3[75]	2.2[130]
c-Si	0.58[131]	1.07E6[131]	1685	1805E3[75]	2.33[130]
L-si	0.58[132]	1.0E6	- - -	- - -	2.52[130]
Quartz	- - -	- - -	- - -	- - -	2.2[133]
BAS	- - -	- - -	- - -	- - -	2.54
YSZ	- - -	- - -	- - -	- - -	5.94[126]

Table B7. Laser parameters used for silicon crystallization simulation.

Parameter	Simulation Value(s)
Major Axis (μm)	1526
Minor Axis (μm)	11
Laser Repetition Rate (kHz)	50
Pulse Width (FWHM, ns)	12
Power (mW)	75-1450 ($\Delta 5 = 75$)

APPENDIX C. LASER-CRYSTALLIZATION CODE

```
import java.io.*;

import java.text.*;

import java.util.*;

public class SiCrystallization{

    private static String stateDiagram = "c://users//Origin//Desktop//state";

    private static String tempProfile = "c://users//Origin//Desktop//temp";

    private static String intensity = "c://users//Origin//Desktop//intensity";

    private static String temporary = "c://users//Origin//Desktop//temporary";

    public static final String SUBSTRATE =

    //      "bas";

            "c-Si";

    //      "quartz";

    //      "ysz";

    // substrate

    private static final double aSi_Rho = (2.2)*1E-21, polySi_Rho = (2.33)*1E-21, lSi_Rho =

    (2.52)*1E-21,  bas_Rho = (2.54)*1E-21, cSi_Rho = (2.33)*1E-21,       quartz_Rho =

    (2.20)*1E-21, ysz_Rho = (5.94)*1E-21;

/* dt:      c-Si:   6.54E-6

 *          BAS:    6.3E-6

 *          Quartz:6.54E-6

 *          YSZ:    3.67E-6

 */
```

```
private static final int startPow = 1450, endPow = 1450, dPow = 150;
private static final int startX = 0, endX = 0;        // usually -7000 to 2000 nm
private static final double dt = 6.54E-6, totalTime = 40;
// film and substrate thicknesses
private static final int  si_h = 100, sub_h = 800;
// simulation parameters
private static final double dx = 1, T_amb = 300;
// laser parameters
private static double power = 0;
private static final double pWidth = 12, repRate = (50000)*1E-9, majorAxis =
(1526.0/2)*1E3, minorAxis = (11.0/2)*1E3, area = 3.14159*majorAxis*minorAxis;
// reflectances
private static final double aSi_R = .50472, polySi_R = .57583, lSi_R = .58;
// absorption coefficients
private static final double aSi_Abs = (1.01E6)*1E-7, polySi_Abs = (1.07E6)*1E-7, lSi_Abs
= (1.0E6)*1E-7;
// latent heats
private static final double aSi_L = 1320E3, polySi_L = 1805E3;
//melting temperatures
private static final double aSi_Tmelt = 1420, polySi_Tmelt = 1685;
private static int length = sub_h+si_h;
private static int beamPos = 0;
private static double dx3 = dx*dx*dx;
```

```
    private static double t = 0, j = 0;
    private static double trans = 1;
    private static final int[] state = new int[length];   // 0 = a-Si, 1 = polySi, 2 = l-Si, 3 = sub
    private static double[] oldT = new double[length];
    private static double[] T = new double[length];
    private static double[] q = new double[length];
    private static double getDensity(int x) {
        double rho = aSi_Rho;
        return rho;
    }

    private static double getSpecificHeat(int x, double T) {
        double c=0;
        if(state[x]==0)      // a-Si state
            c = (0.952+0.171*T/1685)*1000;
        else if(state[x]==1)     // poly-Si
            c = (13.31359+.03354*T-3.48365E-5*T*T+1.81126E-8*T*T*T-3.55409E-
12*T*T*T*T)*1000/28.1;
        else if(state[x]==2)     // liquid Si state
            c = (27.2)*1000/28.1;
        else
//          c = (.34429-.2845*Math.exp(-T/614.27297))*4.184E3;            //BAS
```

```
            c = (13.31359+.03354*T-3.48365E-5*T*T+1.81126E-8*T*T*T-3.55409E-
12*T*T*T*T)*1000/28.1;          //c-Si
//          c = (-3.07334+0.23008*T-2.78115E-4*T*T+1.49769E-7*T*T*T-2.94226E-
11*T*T*T*T)*1000/60.08;   // quartz
//          c = (83.91092-65.72648*Math.exp(-T/425.8675))*1000/124.32;          //YSZ
        return c;
    }
    private static double getThermalConductivity(int x, double T) {
        double k = 0;
        if(state[x]==0)      // a-Si state
            k = (4.828*1E-11*(T-900)*(T-900)*(T-900)+4.828*1E-9*(T-900)*(T-
900)+3.714*1E-6*(T-900)+3.7141E-2)*1E-13;
        else if(state[x]==1)     // poly-Si
            k = (19.15536+0.00274*T-0.0000137435*T*T+5.93E-9*T*T*T)*1E-15;
        else if(state[x]==2)     // liquid Si state
            k = (5.71E-4*(T-1685)+58.6)*1E-15;
        else                     // substrate
//          k = (.00422-.00331*Math.exp(-T/611.25063))*4.184E-13;       //BAS
            k = (279.79-.73*T+8.37E-4*T*T-4.43E-7*T*T*T+8.98E-11*T*T*T*T)*1E-15;
            //c-Si
//          k = (1.97E-3+8.3E-5*T+6.54E-9*T*T-5.74E-12*T*T*T+1.35E-
15*T*T*T*T)*4.184E-13;    //quartz
//          k = (2.0128-2.29162*Math.exp(-T/144.13756))*1E-15;           //ysz
```

```
        return k;
    }
    private static double getThermalConductivityPrime(int x, double T) {
        double kPrime = 0;
        if(state[x]==0)      // a-Si state
            kPrime = (3*4.828*1E-11*(T-900)*(T-900)+2*4.828*1E-9*(T-900)+3.714*1E-
6)*1E-13;
        else if(state[x]==1)     // poly-Si
            kPrime = (0.00274-2*0.0000137435*T+3*0.00000000593605*T*T)*1E-15;

        else if(state[x]==2)     // liquid Si state
            kPrime = (5.71E-4)*1E-15;
        else
//          kPrime = (.00331*Math.exp(-T/611.25063)/611.25063)*4.184E-13;    //bas
            kPrime = (-.73353+2*8.37458E-4*T-3*4.43058E-7*T*T+4*8.98469E-
11*T*T*T)*1E-15;    //c-si
//          kPrime = (.83958+2*.00654*T-3*5.74935E-6*T*T+4*1.35858E-9*T*T*T)*4.184E-
13;      //quartz
//          kPrime = (2.29162*Math.exp(-T/144.13756)/144.13756)*1E-15;        //ysz
        return kPrime;
    }
    private static double getReflectance() {
        double R;
```

```
    if(state[1]==0)
        R = aSi_R;
    else if(state[1]==1)
        R = polySi_R;
    else
        R = lSi_R;
    return R;
}
private static double getAbsorption(int x) {
    double abs;
    if(state[x]==0)
        abs = aSi_Abs;
    else if(state[x]==1)
        abs = polySi_Abs;
    else
        abs = lSi_Abs;
    return abs;
}
private static double getSource(int x) {
    double I_t, I, Io, abs, R;
    double pos2 = (double)beamPos*beamPos;
    double peakPower = .94*power/(repRate*pWidth);
    Io = 2*peakPower/area;
```

```
    Io*=Math.exp(-2*pos2/(minorAxis*minorAxis));
    R = getReflectance();
    abs = getAbsorption(x);
    I_t = Io*(1-R)*Math.exp(-2.77*(t-1.5*pWidth)*(t-1.5*pWidth)/(pWidth*pWidth));
    if(x==1) {
        trans = 1;
        I = I_t*trans*(1-Math.exp(-abs*dx));
        trans*=Math.exp(-abs*dx);
    }
    else {
        I = I_t*trans*(1-Math.exp(-abs*dx));
        trans*=Math.exp(-abs*dx);
    }
    return I;
}
private static void checkMelt(int x) {
    double m = 0, c = 0;
    double dQ = 0;
    m = dx3*getDensity(x);
    c = getSpecificHeat(x, oldT[x]);
    if(state[x]==0 && (T[x] >= aSi_Tmelt || q[x]>0)) {
        dQ = m*c*(T[x]-aSi_Tmelt);
        q[x]+=dQ;
```

```
    T[x] = aSi_Tmelt;
    if(q[x]>=aSi_L*m) {
        T[x] = (q[x]-aSi_L*m)/(c*m)+aSi_Tmelt;
        state[x]=2;
        q[x] = 0;
    }
    return;
}
else if(state[x]==1 && (T[x] >= polySi_Tmelt || q[x]>0)) {
    dQ = m*c*(T[x]-polySi_Tmelt);
    q[x]+=dQ;
    T[x] = polySi_Tmelt;
    if(q[x]>=polySi_L*m) {
        state[x]=2;
        q[x] = 0;
    }
    return;
}
else if(state[x]==2 && T[x]<polySi_Tmelt) {
    dQ = m*c*(T[x]-oldT[x]);
    if(q[x]>=0) {
        if(T[x]<oldT[x]) {
            T[x] = oldT[x];
```

```
                    q[x]+=dQ;
                    return;
                }
                else
                    return;
            }
            else if (q[x]<0) {
                T[x] = oldT[x];
                q[x]+=dQ;
            }
            if(q[x]<=-polySi_L*m) {
                state[x]=1;
                q[x] = 0;
            }
            return;
        }
    }
    public static void makeStateDiagram() {                    // 0 = a-Si, 1 = polySi, 2 = l-Si
        try(PrintWriter pw = new PrintWriter(new BufferedWriter(new FileWriter(stateDiagram,
true)))) {
            pw.print(t + " " + state[0] + " ");
            for(int i=1; i<si_h-1; i++) {
                pw.print(state[i] + " ");
```

```
            }
            pw.print(state[si_h-1]);
            pw.println();
        } catch(IOException e) {};
    }
    private static void initialize() {
        for(int i=0; i<length; i++) {
            q[i] = 0;
            T[i]=T_amb;
            if(i<si_h)
                state[i] = 0;
            else
                state[i] = 3;
        }
        oldT = T.clone();
    }
    private static void step() {
        double k=0;             // thermal conductivity
        double kPrime=0; // Temperature derivative of thermal conductivity
        double c=0;             // specific heat
        double rho=0;       // density
        double source = 0;
            // boundary condition dT/dx(0) = 0
```

```
T[0] = T[1];
state[0] = state[1];
if(t>=j)
    try(PrintWriter pw = new PrintWriter(new BufferedWriter(new
FileWriter(tempProfile, true)))) {
        pw.print(t + " " + T[0] + " ");
    } catch(IOException e) {};
// implicit boundary condition: T(L) = 0
for(int i=1; i<length-1; i++) {
    k = getThermalConductivity(i, oldT[i]);
    kPrime = getThermalConductivityPrime(i, oldT[i]);
    c = getSpecificHeat(i, oldT[i]);
    rho = getDensity(i);
    source = dt*getSource(i)/(rho*c);
    T[i] = (dt/(rho*c*dx*dx))*(kPrime*(oldT[i+1]-oldT[i])*(oldT[i+1]-
oldT[i])+k*(oldT[i+1]-2*oldT[i]+oldT[i-1]))+oldT[i]+source;
    if(i<si_h)
        checkMelt(i);
    if(t>=j && i<si_h)
        try(PrintWriter pw = new PrintWriter(new BufferedWriter(new
FileWriter(tempProfile, true)))) {
            pw.print(T[i] + " ");
        }catch(IOException e){};
```

```
            }
            if(t>=j) {
                try(PrintWriter pw = new PrintWriter(new BufferedWriter(new
FileWriter(tempProfile, true)))) {
                    pw.print(T[si_h-1]);
                    pw.println();
                    pw.close();
                }catch(IOException e) {};
                //makeStateDiagram();
                j+=1;
                System.out.println(t);
            }
    }
    public static void printHeader(String path) {
        try(PrintWriter pw = new PrintWriter(new BufferedWriter(new FileWriter(path, true))))
{
            pw.println("si_h = " +si_h);
            pw.println("sub_h = " +sub_h);
            pw.println("dx = " +dx);
            pw.println("dt = " +dt);
            pw.println("totalTime = " +totalTime);
            pw.println("T_amb = " +T_amb);
            pw.println("pWidth = " +pWidth);
```

```
pw.println("repRate = " +repRate);
pw.println("majorAxis = " +majorAxis);
pw.println("minorAxis = " +minorAxis);
pw.println("power = " +power);
pw.println("area = " +area);
pw.println("Power = " +power);
pw.println("aSi_Rho = " +aSi_Rho);
pw.println("polySi_Rho = " +polySi_Rho);
pw.println("lSi_Rho = " +lSi_Rho);
pw.println("substrate_Rho = " + getDensity(length-1));
pw.println("aSi_R = " +aSi_R);
pw.println("polySi_R = " +polySi_R);
pw.println("lSi_R = " +lSi_R);
pw.println("aSi_Abs = " +aSi_Abs);
pw.println("polySi_Abs = " +polySi_Abs);
pw.println("lSi_Abs = " +lSi_Abs);
pw.println("aSi_L = " +aSi_L);
pw.println("polySi_L = " +polySi_L);
pw.println("aSi_Tmelt = " +aSi_Tmelt);
pw.println("polySi_Tmelt = " +polySi_Tmelt);
pw.println("startX = " +startX);
pw.println("endX = " +endX);
pw.println("");
```

```
            for(int x=0; x<si_h; x++)
                pw.print(" " + x + " ");
            pw.println();
        } catch(IOException e) {}
    }
    public static void newPulse() {
        for(int i=0; i<length; i++) {
            q[i] = 0;
            T[i]=T_amb;
        }
        oldT = T.clone();
    }
    public static void scanSample() {
        initialize();
        printHeader(tempProfile);
// beam moves .5 um between pulses
        for(beamPos=startX; beamPos<=endX; beamPos+=500) {
            System.out.println("Power: " + power + " " + "Beam Pos: " + beamPos);
            for(t=0; t<=totalTime+dt; t+=dt) {          // beam width is 11 um so start
                step();                                  // crystallization 7 um before cell
                oldT = T.clone();
            }
            newPulse();
```

```
            j=0;
        }
    }
    public static void main(String[] args) {
        long startTime = System.currentTimeMillis();
        int tempChar = tempProfile.length();
        int temporaryChar = temporary.length();
        int stateChar = stateDiagram.length();
        int intensityChar = intensity.length();

        DateFormat df = new SimpleDateFormat("yyyyMMdd_HHmmss");
        Calendar calobj = Calendar.getInstance();
        for(int i=startPow; i<=endPow; i+=dPow) {
            power = i*1E-9;
            tempProfile = tempProfile.substring(0, tempChar) + "_" + SUBSTRATE + "_" +
Integer.toString(i) + "_" + df.format(calobj.getTime()) + ".txt";
            stateDiagram = stateDiagram.substring(0, stateChar) + "_" + SUBSTRATE + "_" +
Integer.toString(i) + "_" + df.format(calobj.getTime()) + ".txt";
            intensity = intensity.substring(0, intensityChar) + "_" + SUBSTRATE + "_" +
Integer.toString(i) + "_" + df.format(calobj.getTime()) + ".txt";
            temporary = temporary.substring(0, temporaryChar) + "_" + SUBSTRATE + "_" +
Integer.toString(i) + "_" + df.format(calobj.getTime()) + ".txt";
            scanSample();
```

```
        }
        long totalTime = (System.currentTimeMillis()-startTime);
        System.out.println("Total Time: " + totalTime);
    }
}
```